DIRECTED ENERGY DEPOSITION OF Ni-Mn-Ga MAGNETIC SHAPE MEMORY ALLOY

by

Jakub Toman

B.S. in Engineering, Robert Morris University, 2012

Submitted to the Graduate Faculty of
the Swanson School of Engineering in partial fulfillment
of the requirements for the degree of
Master of Science

University of Pittsburgh

2016

UNIVERSITY OF PITTSBURGH
SWANSON SCHOOL OF ENGINEERING

This thesis was presented

by

Jakub Toman

It was defended on
November 17, 2016
and approved by

Markus Chmielus, Ph.D., Assistant Professor
Department of Mechanical Engineering and Materials Science

Ian Nettleship, Ph.D., Associate Professor
Department of Mechanical Engineering and Materials Science

Albert To, Ph.D., Associate Professor
Department of Mechanical Engineering and Materials Science

Thesis Advisor: Markus Chmielus, Ph.D., Assistant Professor
Department of Mechanical Engineering and Materials Science

DIRECTED ENERGY DEPOSITION OF Ni-Mn-Ga MAGNETIC SHAPE MEMORY ALLOY

Jakub Toman, M.S.

University of Pittsburgh, 2016

Processing of magnetic shape memory alloys – active materials that show strains of up to 12 % in a magnetic field and that are being targeted for application as actuators, sensors and energy harvesters – suffers from challenges including time-intensive production and macrosegregation that leads to reduced yield. Furthermore, the brittle mechanical behavior of these materials largely eliminates the possibility of machining for a desired shape. This work explores directed energy deposition, an additive manufacturing or "3D printing" process, as an alternative processing route for Ni-Mn-Ga magnetic shape memory alloy. The magnetic properties, transformation behavior, and composition of the feedstock powder and deposits resulting from a laser metal deposition process are investigated against varied laser power. All samples are seen to possess favorable magnetic behavior and potentially favorable phase for magnetic-field induced strain (MFIS) to take place. Additionally, the microstructure of the deposited samples is observed and its special features that may aid MFIS are discussed. Most notably, this thesis presents possible evidence of twin variants crossing deposition layers and of twin boundary motion in a magnetic field. Finally, a connection between lower laser power and reduced loss of Mn is considered.

TABLE OF CONTENTS

PREFACE ..... **XIV**

1.0 INTRODUCTION **1**

1.1 GENERAL CONCEPT AND MOTIVATION **1**

1.2 HYPOTHESIS **2**

1.3 MAGNETIC SHAPE MEMORY ALLOYS **2**

1.4 HEUSLER ALLOYS **5**

1.5 SUMMARY OF MAGNETISM **6**

1.6 PHASES OF NI-MN-GA **16**

1.7 PROCESSING OF NI-MN-GA **23**

1.8 MAGNETIC FIELD-INDUCED STRAIN **28**

1.9 ADDITIVE MANUFACTURING **34**

2.0 EXPERIMENTS **39**

2.1 DEPOSITION OF SAMPLES BY DIRECTED ENERGY DEPOSITION **39**

2.1.1 Laser Engineered Net Shaping **39**

2.1.2 LENS® 450 System Specifics **40**

2.1.3 Mechanism of deposition **43**

2.1.4 AM terminology and other processes related to LENS® **46**

2.1.5 Deposition of samples within this thesis **47**

2.2 PREPARATION OF POWDER FEEDSTOCK **50**

2.3 ANNEALING HEAT TREATMENT APPLIED TO POWDER **51**

2.4 SAMPLE SECTIONING **52**

2.5 VIBRATING SAMPLE MAGNETOMETRY **52**

2.5.1 Overview **52**

2.5.2 Physical Property Measurement Systems (PPMS) VSM Option **54**

2.5.3 LakeShore model 7407 VSM 55
2.5.4 PPMS VSM Experiments 56
2.5.5 LakeSore VSM Experiments 57
2.6 DIFFERENTIAL SCANNING CALORIMETRY 59
2.6.1 Overview 59
2.6.2 DSC Experiments 62
2.7 OPTICAL MICROSCOPY 63
2.7.1 Overview 63
2.7.2 Differential Interference Contrast (DIC) 63
2.7.3 Optical Microscopy within this thesis 67
2.7.4 Differential Interference Contrast (DIC) microscopy within this thesis 68
2.8 SCANNING ELECTRON MICROSCOPY 68
2.8.1 Overview 68
2.8.2 SEM Images within this thesis 70
2.9 ENERGY DISPERSIVE SPECTROSCOPY 71
2.9.1 Energy Dispersive Spectroscopy in this thesis 72
3.0 RESULTS: POWDER FEEDSTOCK 73
3.1 COMPOSITION 73
3.2 MAGNETIC PROPERTIES 74
3.3 TRANSFORMATIONS 75
4.0 RESULTS: DEPOSITED SAMPLES 77
4.1 SAMPLE MORPHOLOGY 77
4.2 COMPOSITION 79
4.3 MAGNETIC PROPERTIES 80
4.4 TRANSFORMATIONS 83
4.5 MICROSTRUCTURE 90
5.0 DISCUSSION 98
5.1 SAMPLE MORPHOLOGY 98
5.2 MAGNETIC PROPERTIES 100
5.2.1 Overview 100
5.2.2 Saturation magnetization behavior 101

5.2.3 Inflection points in the M-H curves 103
5.2.4 Curie points 104
5.3 PHASE 106
5.4 MICROSTRUCTURE AND COMPOSITION 112
5.5 INFLUENCE OF PROCESSING PARAMETER 115
6.0 CONCLUSION 119
7.0 OUTLOOK 121
APPENDIX 123
BIBLIOGRAPHY 126

LIST OF TABLES

Table 1. General sign and magnitude of magnetic permeability and susceptibility corresponding to magnetic classification of a material 10

Table 2. Structures of the austenite and martensite phases of Ni-Mn-Ga 19

Table 3. Example lattice parameters and angles of Ni-Mn-Ga..... 20

Table 4. Selected properties of Ni-Mn-Ga martensites 21

Table 5. Industrial additive manufacturing (AM) processes regularly used for metals..... 37

Table 6. Selected synonyms for additive manufacturing..... 38

Table 7. Process parameters used for deposition of samples..... 48

Table 8. Masses of the deposited samples after removal from substrate..... 49

Table 9. Properties of the Ni-Mn-Ga powder, including properties of the feedstock powder. 51

Table 10. Parameters used for moment versus temperature (M vs. T) experiments with the LakeShore VSM..... 59

Table 11. Measured and reported compositions of the feedstock powder..... 73

Table 12. Transformation temperatures extracted from DSC experiment with annealed small-size powder 75

Table 13. Averaged energy dispersive spectroscopy (EDS) results obtained from each deposited sample and comparison to powder composition. 80

Table 14. Ferromagnetic properties determined from M vs. $\mu_0 \cdot H$ data 82

Table 15. Curie temperatures and austenite start temperatures obtained from the data displayed in Figure 36 and Figure 39 87

Table 16. Selected temperatures observed in DSC data on heating for feedstock powder and the deposited samples 89

Table 17. Comparison of transformation temperatures measured for small-size powder to transformation temperatures from literature 107

Table 18. Comparison of transformation temperatures acquired for powder and deposited samples 117

LIST OF FIGURES

Figure 1. Schematics of MSMA actuation 3

Figure 2. The $L2_1$ structure 5

Figure 3. Force on a body in a magnetic field. 6

Figure 4. a) Magnetic moment due to loop of current, b) simplified schematic of net magnetic moment due to sum of moments in a solid body. 9

Figure 5. (a) Orbit and spin motions of an electron in a simplified orbit model. (b) Magnetic moment due to an electron's orbital motion 11

Figure 6. Magnetic field vs. applied field for a ferromagnetic material 13

Figure 7. Simplified schematic of ferromagnetic domains in a polycrystal 14

Figure 8. Surfaces of equal magnetic anisotropy energy 15

Figure 9. Model structures of (a) 10M martensite viewed along [010], and (b) The 14M martensite viewed along [010] 18

Figure 10. Pseudo-orthorhombic unit cell for 14M martensite 18

Figure 11. Schematic of a single crystal growth furnace. 24

Figure 12. Compositional variation in one quarter of a circular laser spot 27

Figure 13. Demonstration of the MFIS process in a single MSMA crystal 30

Figure 14. Schematic illustrating the lattice shear by which the twin boundary moves 31

Figure 15. Magnetization vs. magnetic field strength data obtained by VSM for Ni-Mn-Ga single crystals 31

Figure 16. MFIS vs. direction of an applied, rotating magnetic field 33

Figure 17. Schematic of a powder bed system 36

Figure 18. Schematic of a powder feed system. 36

Figure 19. Optomec LENS 450 40

Figure 20. Schematic of the LENS 450 deposition head. 42

Figure 21. Deposition path used for each layer of the deposited samples 47

Figure 22. Deposited samples while still joined to the substrate 49

Figure 23. Schematic demonstrating sample directions and terminology used 50

Figure 24. Simplified schematic of an early vibrating sample magnetometer (VSM) 54

Figure 25. Example DSC curve collected with a Ni-Mn-Ga sample 60

Figure 26. Example of the effect of rate of temperature change on the same sample 61

Figure 27. The same exact field of view (an edge of a notch in a piece of metal) is acquired with (a) brightfield microscopy, (b) DIC microscopy, and (c) DIC microscopy with optical staining.. 64

Figure 28. The optical path in a reflected light microscope with DIC in a de Sénarmont design.. 66

Figure 29. (a) Schematic of a scanning electron microscope. (b) Graphic demonstrating the categories of particles ("signals") created by interaction of an electron beam with a sample 70

Figure 30. Example energy dispersive spectroscopy (EDS) spectrum 72

Figure 31. Magnetization versus magnetic field strength (M vs. $\mu_0 \cdot H$) curves for small size Ni-Mn-Ga powder in the as-received condition. 74

Figure 32. DSC experiment on small-size powder 76

Figure 33. Views of samples in as-deposited condition 78

Figure 34. Saturation magnetization experiments on deposited samples 81

Figure 35. Close-up of data shown in Figure 34 82

Figure 36. Magnetization vs. temperature curves obtained by use of the PPMS VSM 85

Figure 37. Plot of PPMS VSM data shown in Figure 36, limited to the range of 35 °C to 100 °C 86

Figure 38. Magnetization vs. temperature curves obtained by use of the LakeShore VSM with "quasi-continuous" parameters 86

Figure 39. Magnetization vs. temperature curves obtained by use of the LakeShore VSM with "quasi-settling" parameters 87

Figure 40. DSC experiments at temperature rate of change of 10 °C/minute. 88

Figure 41. DSC experiments at temperature rate of change of 20 °C/minute. 88

Figure 42. DSC experiments on the two pieces of the 200 W sample..... 89

Figure 43. Directions on micrographs of deposited sample cross-sections. 90

Figure 44. Optical micrograph of polished cross-section of 300 W sample, acquired while in focus (left) out of focus (right) 91

Figure 45. Composite image of differential interference contrast (DIC) optical micrographs of the 200 W sample in (left) the as-polished condition and (right) after heating above room temperature 91

Figure 46. Composite image of differential interference contrast (DIC) optical micrographs of the 250 W sample in the as-polished condition (top) and after heating above room temperature (bottom) 92

Figure 47. Composite image of differential interference contrast (DIC) optical micrographs of the 300 W sample in the as-polished condition (top) and after heating above room temperature (bottom) 92

Figure 48. Optical micrographs of 200 W (top), 250 W (middle) and 300 W (bottom) samples after etching 93

Figure 49. Optical micrograph of 200 W sample after etching, revealing the difference between the top layer of the sample and the underlying layer 94

Figure 50. Backscattered electron image of the 300 W sample displaying contrast in regions, as well as in parallel bands within the darker regions 95

Figure 51. Backscattered electron image of the 300 W at higher magnification (left) and highest magnification (right). Bands are seen to be twins and small-scale porosity and scratches become easily discernable 95

Figure 52. Differential interference contrast (DIC) optical micrograph of the 300 W sample 96

Figure 53. Differential interference contrast (DIC) optical micrograph of the 300 W sample. ... 97

Figure 54. Differential interference contrast (DIC) optical micrograph of the 300 W sample at a layer boundary 97

Figure 55. Magnetization vs. magnetic field strength data obtained by VSM for Ni-Mn-Ga single crystals 103

Figure 56. Compilation and curve fitting of Curie temperature data from literature 105

Figure 57. Susceptibility vs. temperature experiment which demonstrates the expected shape of the *M* vs. *T* curves for Ni-Mn-Ga with transformation near room temperature 110

Figure 58. Transparent overlay of micrograph of etched 250 W sample and DIC micrograph of the sample after heating 114

Figure 59. Selected regions of composite images created from DIC micrographs of the 250 W sample. Overlaid black lines show the locations of segregation lines (dark lines) that were revealed in micrographs of the sample after etching. 115

PREFACE

I would like to acknowledge the following people for all of their contributions that made this work possible: the research group of Dr. Peter Müllner (for providing the powder feedstock), Yun-Yi Pai and the research group of Dr. Jeremy Levy (for their generous willingness to allow me to use their equipment and gracious help with running experiments), Yuval Krimer (for help with many aspects of this work and related work), Erica Stevens (for SEM images) and my advisor, Dr. Markus Chmielus (for many things, but above all, for his patience and encouragement).

1.0 INTRODUCTION

1.1 GENERAL CONCEPT AND MOTIVATION

Magnetic shape memory alloys are promising active materials which exhibit a reversible magnetic field-induced strain of up to 12% [1], and can achieve a strain and its full reversal many times per second. For this reason, they have potential application as elements in actuators, sensors, and energy-harvesting devices. Of the various materials investigated, Ni-Mn-Ga is by far the leading MSMA in terms of research activity and attempted application. Actuators based on Ni-Mn-Ga have been successfully demonstrated and reach frequencies of 800 Hz [2] or more, sometimes reported as the order of 10^3 Hz [3] [4]. Thus, these materials achieve a combination of strain and speed which is not achievable by any other active material: electrostrictive, magnetostrictive and piezoelectric ceramics are not comparable due to strains on the order of 0.1 %, ionic electroactive polymers achieve strains on the order of 1 %, and (conventional) shape memory alloys, shape memory polymers, ionic electroactive polymers and even piezoelectric polymers cannot achieve actuation frequencies above 10^2 Hz (see Fig. 1.1 and 1.2 of [3]). However, production of magnetic shape memory elements using currently proven processing routes, including single-crystal growth and foam creation by replication casting, is time- and cost- intensive. Recently popularized “additive manufacturing” methods may provide faster and cheaper alternatives, with potential for greater choice in the shape of the resulting product. Additionally, deliberate parameter choices may lead to preferred orientation and porosity, both of which may be desirable. This work seeks to establish that directed energy deposition (DED) can produce Ni-Mn-Ga samples with room-temperature magnetic properties and phase that are prerequisite for magnetic field-induced strain, and that processing parameters influence these properties.

1.2 HYPOTHESIS

It is hypothesized that when processed by directed energy deposition, a Ni-Mn-Ga alloy that is of composition to otherwise be present as martensite at room temperature, will form martensite upon cooling to room temperature. This hypothesis is made even in light of the rapid solidification rates and rapid cooling rates experienced by the material.

Objectives

1. To obtain Ni-Mn-Ga powder of composition which should be present as martensite at room temperature; and
2. to deposit the Ni-Mn-Ga powder with Laser Engineered Net Shaping, a directed energy deposition method; and
3. to investigate the transformation behavior of the deposited samples and search for indications of twinning within the samples by microscopy.

1.3 MAGNETIC SHAPE MEMORY ALLOYS

Magnetic shape memory alloys (MSMAs) are materials that exhibit the magnetic shape memory effect (MSME): a reversible plastic deformation driven by appropriate magnetic or magneto-mechanical forces (Figure 1). This deformation, when expressed as a strain, is called a magnetic field-induced strain (MFIS). For MFIS to be possible, a material must possess an anisotropic unit cell with associated magnetic anisotropy, must be ferromagnetic at the temperature of interest, and must have a proclivity for twinning with a twinning stress that is lower than the available magnetic stress. Unexplained magnetic behavior in dysprosium and in terbium at cryogenic temperatures [5] was later discovered to be plastic deformation by means of mechanical twinning in a magnetic field (in Dy) [6]. “Magnetic-field-induced strains” as a term in its own right was introduced, and became widely noted, after it was demonstrated to achieve 0.2 % strain in Ni_2MnGa at a non-cryogenic temperature by Ullakko et al. [7]. Various magnetic shape memory

alloys have been identified since then, and most, but not all, are Heusler alloys with chemical formula A_2XY or near-stoichiometric variations on such compositions. Other MSMAs include Fe-Pd [8], Fe_3Pt, Co-Ni-Al, Co-Ni-Ga, Ni-Mn-Al, Ni-Mn-Sn, and Ni-Mn-In, Ni-Fe-Al, and Ni-Fe-Ga [9]. Ni-Mn-Ga remains as the most widely researched MSMA and still holds the title of highest demonstrated MFIS, with 12% observed in an alloy with Co and Cu ($Ni_{46}Mn_{24}Ga_{22}Co_4Cu_4$) [1]. The highest MFIS achieved in Ni-Mn-Ga without additional alloying elements is 9.7% [10]. Importantly, this high MFIS was observed at room temperature. Furthermore, Ni-Mn-Ga crystals with very low twinning stresses have been developed, leading to very high energy conversion efficiency (up to 90 %) within the crystal itself [11]. For this reason, this thesis features Ni-Mn-Ga and addresses properties needed for MFIS rather than for other effects.

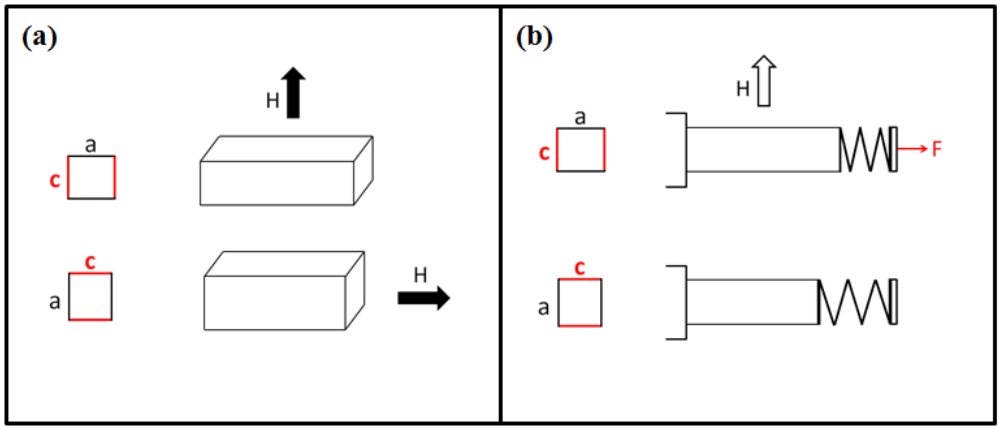

Figure 1. (a) Schematic of MSMA actuation in a rotating magnetic field. The magnetic field (vector H) is applied in mutually perpendicular directions to produce full actuation. The boxes on the left indicate the alignment of crystal axes (for pseudo- unit cells, described later in section 1.6). Adapted from [2] **and** [12]**.**
(b) Schematic of MSMA actuation with an on-off magnetic field. In the top image, the magnetic field is on and the resulting horizontal extension of the MSMA element transfers force through the spring on the right. In the bottom image, the spring supplies a biasing force which returns the element to its pre-actuation state. An electromagnet can provide the on-off field. Adapted from [2]**.**

A comparison to "conventional" shape memory alloys (SMAs) will now be drawn for readers familiar with those materials. Magnetic shape memory alloys share the martensitic transformation (also known as the "military transformation") with the broader class of shape memory alloys. However, unlike shape memory alloys, magnetic shape memory alloys generally

do not see use of this transformation. The MSME is possible only when the material is present as martensite, that is, at temperatures below the transformation temperature. With that said, it must be noted that investigations have been conducted into use of a magnetic field-induced transformation and have shown a resulting strain [13].

Ni-Mn-Ga offers not just a large MFIS, but also holds potential for magnetocaloric [14–16] and “conventional” shape memory alloy applications at higher temperatures [17]. Although the system is not competitive with commercially available SMAs in room-temperature applications, appropriate compositions hold promise at higher temperatures if key limitations can be overcome [18]. If used as an SMA at higher temperatures, the system is said to be a high-temperature shape memory alloy (HTSMA).

Of course, MSMAs also have disadvantages and challenges. The limiting features which are cited as preventing adoption include the relatively low stress at which the MSME can be counteracted by mechanical stress, resulting in low blocking forces attained by actuators, and a narrow temperature range in which a substantial MSME takes place [13] [19]. However, the first point has been countered earlier by the now-defunct manufacturer of commercially available actuators based on the MSME, AdaptaMat Ltd., in a publication demonstrating a multi-element actuator producing a displacement of approximately 0.05 mm under a load of over 900 N [2]. Additionally, one study [13] sought and achieved increases in blocking stress, albeit at a very low temperature of -95 °C. The most promising result which addresses the temperature range question is that of Pagounis and co-authors [20], who reported a Ni-Mn-Ga single crystal which produces significant MFIS of over 7 % and over 4 % at 22 °C and 80 °C, respectively. This result shows functionality over a wide range of practical, everyday temperatures, but also at the highest temperature demonstrated so far, which improves the applicability of MSMA actuators in warm environments such as mechanical compartments. Additionally, Ni-Mn-Ga and other compositions are relatively brittle [21]. Finally, MSMA-based actuators may require advanced control systems. Due to reasons described further at the end of section 1.8, the magnitude of MFIS developed varies as an MSMA element is cycled through extension and return to the original shape. For these reasons, closed-loop control may be necessary in some applications. However, this challenge appears surmountable [22], and may simply add to the cost and complexity of MSMA actuators. Notably, AdaptaMat claimed development of “self-sensing” actuators, which use changes in electrical resistance to sense the length of the MSMA element.

1.4 HEUSLER ALLOYS

The present wealth of research about the Ni-Mn-Ga system begins with investigations of the stoichiometric compound Ni_2MnGa, a member of the class of Heusler alloys. These alloys exhibit ferromagnetism despite that two or all of elements present in the chemical formula are not ferromagnetic in their pure state [23]. Heusler alloys have stoichiometric compositions of X_2YZ and take on the $L2_1$ structure, which can be understood as interpenetrating face-centered cubic sublattices of Mn and Ga [Webster Ziebeck et al.] [24]. This structure belongs to the $Fm\bar{3}m$ space group [25] and is shown in Figure 2. Some Heusler alloys only take on this structure at temperatures above the austenitic transformation and exist as martensite below the corresponding martensitic transformation, although some do not transform to martensite at any temperature. An example of the latter is Ni_2MnAl [24].

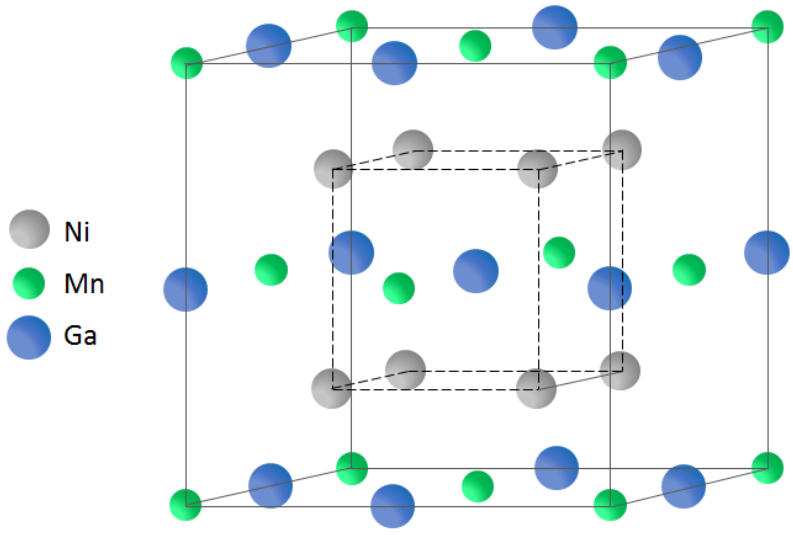

Figure 2. The $L2_1$ structure (prototype: Cu_2MnAl). The continuous line represents the Mn sublattice, while the dashed line represents the Ni sublattice. Adapted from [12] **and** [25]**.**

1.5 SUMMARY OF MAGNETISM

Because magnetism is central to the concept of MSMAs, a foundation for understanding magnetism will be laid in this section. Grossly simplifying, magnetism might be understood as a phenomenon by which the periodic motion of electrons confined within matter (more specifically, electrons not necessarily involved in conduction) can be affected by the periodic or continuous motion of other electrons. The most intuitive demonstration of magnetism involves two bar magnets, whose opposite poles attract, resulting in a tangible force which pulls the magnets together. In a more detailed example, a solid body is hung from a string, and lowered into the air gap of an electromagnet (Figure 3).

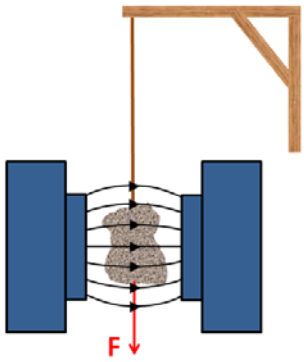

Figure 3. Force on a body in a magnetic field. Adapted from [26]**.**

Due to the magnetic field which is present in the air gap (known as applied field [26] or magnetizing field [27]), the sample will experience a force, and this force can be measured at the string's end (in addition to the force due to the body's weight). This force is dependent on the mass of the body, the applied field strength and its gradient, a physical constant, and the magnetic susceptibility of the material from which the body is made. The susceptibility may vary with crystallographic orientation, and in some cases, with the field strength, the history of magnetic fields applied to the material, and/or with other influences. The force is related to these quantities by equation (1.1) [26]:

$$F = V\chi\mu_0 H\frac{dH}{dx} \tag{1.1}$$

where F is the force [N], V is the volume in [m^3], χ is the volume magnetic susceptibility (unitless, referred to as susceptibility from here), μ_0 is the permeability of free space in [V·s/(A·m)], H is the applied field strength at the location of the body in [A/m], and dH/dx is the gradient of the magnetic field along the axis of the string at that same location [A/m^2]. In this equation, the size of the body is expressed as its volume, although its mass might be used by multiplying by the material's density (if volume is used, it follows that porosity would have to be included if the sample is not fully dense). Mass may also be used in an equation which involves a mass magnetic susceptibility, as opposed to the present definition. Furthermore, for a body of significant size, the equation would have to be applied in such a way that addresses H and dH/dx over the volume of the body (the fact that these quantities vary over the body is apparent in Figure 3). Also, some shapes may lead to demagnetizing fields [12], a situation which is not addressed here. Above all, it must be understood that the susceptibility χ may or may not be a constant, even when all influences but the applied field are held constant (e.g., temperature, lattice strain, crystallographic orientation). The susceptibility is not a constant in ferromagnetic materials, and this is explained later in this section.

Often, magnetic permeability μ is discussed instead of susceptibility. Permeability comes from relating an applied field to the magnetic field B inside a material, which is said to be "induced" by the applied field (magnetic field is thus also called magnetic induction, but this term is not to be confused with electromagnetic induction). The magnetic field is due to both the applied field, which would be present in free space in the absence of material, and due to the response of the material present within the field. Magnetic field is related to applied field by the relation [26]:

$$B = \mu_r\mu_0 H \tag{1.2}$$

where B is the magnetic field [T], μ_r is the relative permeability (unitless), μ_0 is the permeability of free space [V·s/(A·m)], and H is the applied field [A/m]. The quantity $\mu = \mu_r\mu_0$ is often referred to as the magnetic permeability, while sometimes μ_r itself is referred to as the magnetic permeability. As before, it is emphasized that the magnetic permeability μ (and so by necessity the relative permeability μ_r) may or may not be constant with respect to applied field. In the case of magnetized ferromagnetic materials, it may be better to say that the equation does not apply [27].

If the effect of the presence of material in an applied field is separated from the applied field (that would otherwise be present in the absence of material), the magnetization M results. Then, the magnetic field B can be thought of as consisting of the applied field H and the magnetization M. This relationship is captured by the following equation [26] [27]:

$$B = \mu_0 H + \mu_0 M \tag{1.3}$$

where M has units of [A/m]. After combining equation (1.2) with equation (1.3) [26]:

$$M = \chi H \tag{1.4}$$

It must be noted that M is dependent on H in all cases, while the susceptibility χ may or may not be independent of H. Again, in the case of magnetized ferromagnetic materials (known as possessing a remanent magnetization), one can interpret the equation as giving an infinite susceptibility when H is zero; however, it may be better to say that the equation does not apply for ferromagnetic materials [27].

A solid body possesses a magnetic moment that results from the aggregate of many smaller moments (Figure 4(a)), whose origins are described later. Because a body has a magnetic moment, the body experiences a torque when placed in a magnetic field – just as a loop of electric current does (Figure 4(b)). M is related to the magnetic moment μ_m of a body and the body's volume V by the relation [26]:

$$M = \frac{\mu_m}{V} \tag{1.5}$$

An alternative definition of M is the mass magnetization, which replaces volume V with mass m. The preceding definition is thus sometimes referred to as the volume magnetization.

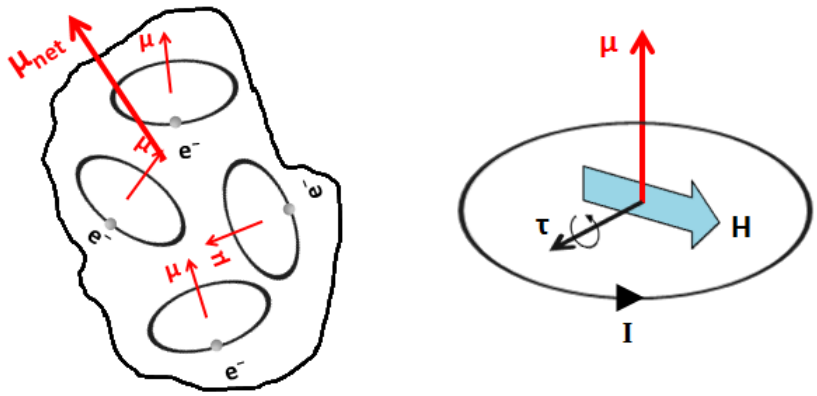

Figure 4. a) Magnetic moment due to loop of current, b) simplified schematic of net magnetic moment due to sum of moments in a solid body.

A material is said to display one of five types of magnetism: diamagnetism, paramagnetism, ferromagnetism, ferrimagnetism, or antiferromagnetism. Although each magnetic behavior is a distinct physical mechanism, and multiple of these can occur simultaneously in a material volume (e.g., diamagnetism and paramagnetism), one effect will generally overshadow the others. Thus the magnetic behavior of the material is named for the dominant magnetic mechanism. Various materials have a disparate range of permeability values as a direct result of the various mechanisms. Because of the fundamental differences between these mechanisms, the permeability value generally narrows the list of possibly active mechanisms, as shown in Table 1.

Table 1. General sign and magnitude of magnetic permeability and susceptibility corresponding to magnetic classification of a material, based on [26] **and** [27]**.**

	Susceptibility χ	Permeability μ
Free space, air (practically)	0	1
Diamagnetic	negative, small	slightly less than 1
Para-, antiferro- magnetic	positive, small	slightly greater than 1
Ferro-*, ferri- magnetic	positive, large	large
*For ferromagnetic, dependent on *H* and history of *H*. All values except diamagnetic dependent on temperature *T* (diamagnetic is essentially insensitive to *T*). Other dependencies also exist.		

The ***origin of magnetic moments*** will now be described. Magnetic moments arise from the motion of electrons. For the present purpose, electrons around an atomic nucleus may be simplified as particles which orbit about the nucleus in a simple, circular path. Then, an electron orbiting a single nucleus possesses two degrees of freedom in its motion: the orientation of the axis of its orbital motion, and the direction of its spin (Figure 5(a)). These generate two magnetic moments, known as the orbital magnetic moment μ_{orb} and spin magnetic moment μ_s. The orbital magnetic moment is analogous to the magnetic moment created by a loop of electric current, where the moment vector can be found using the right-hand rule (Figure 5(b)). This allows visualization of how the orientation of an electron orbit changes the direction of the magnetic moment. Because of constraints imposed by quantum mechanical theory, a full electron subshell will have an equal number of electrons with opposite orbital axis orientation (orbital angular momentum) and an equal number of electrons with opposite spin. The result is that a subshell must be unfilled (incompletely filled) to affect the net magnetic moment of the atom [27]. Finally, the orbitals (wavefunctions) of electrons in solid matter are affected by bonding (including metal bonding) [27], which plays a key role in the magnetic behavior exhibited by a given material.

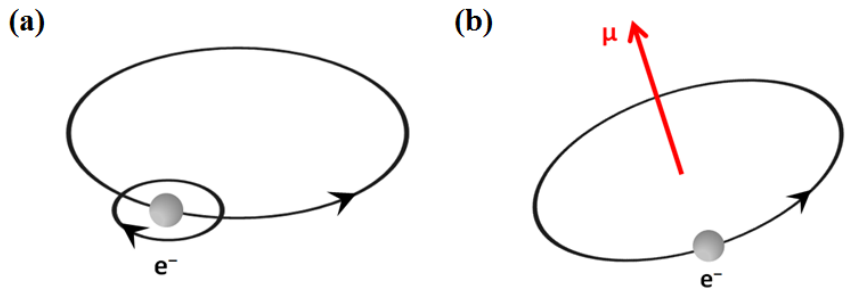

Figure 5. (a) Orbit and spin motions of an electron in a simplified orbit model. The electron orbits around the nucleus, but also possesses a spin. (b) Magnetic moment due to an electron's orbital motion when viewed with the simplified orbit model.

Paramagnetism will be the first magnetic behavior explained. Paramagnetism can include two effects: spin paramagnetism and electron-orbit paramagnetism. Spin paramagnetism is necessary for paramagnetism, while electron-orbit paramagnetism is an additional, less common mechanism. Spin paramagnetism is due to the net sum of spin magnetic moments, which arise due to the electron spin that is shown schematically in Figure 5. Due to the Pauli exclusion principle, at most two electrons can occupy an electron state, and these electrons must have opposite spin. Thus, spin paramagnetism is more likely to occur in materials which have a partially filled electron orbital. Electron-orbital paramagnetism is a distinct effect which is most notable in rare earth elements and their compounds and salts [26]. It is noted that in special cases (at extremely high applied fields), paramagnetic materials might exhibit saturation magnetization (described later for ferromagnetic materials), but are generally thought to lack the saturation phenomenon.

Ferromagnetism is a magnetic effect which provides for special, useful magnetic properties including high susceptibility, saturation magnetization, and remanent magnetization. At room temperature, pure solids of only three elements exhibit ferromagnetism: iron, cobalt, and nickel. In these, the effect results from an aggregate alignment of spin paramagnetism moments of electrons in partially filled d-band orbitals [26]. However, alloys and compounds which also exhibit ferromagnetism exist; e.g., the commercial permanent magnet alloys of samarium-cobalt and neodymium-iron-boron, and manganese can be alloyed to become ferromagnetic [27]. Heusler alloys, to which Ni-Mn-Ga belongs, are ferromagnetic and are described in section 1.4. Additionally, gadolinium and dysprosium become ferromagnetic at

points below room temperature. Dysprosium is notable for the first observation of magnetoplasticity. Ferromagnetism is essential in magnetic shape memory alloys because it provides the high level of magnetically induced stress necessary for MFIS.

The alignment of spins is a result of the ***exchange interaction***, a quantum mechanical consideration which results in a decrease in electrostatic energy when spins of partially filled orbitals are parallel. This alignment is energetically favorable overall in only a limited number of elements and alloys, and ferromagnetism is not common for this reason [27].

The defining phenomenological features of ferromagnetism are a ***hysteresis*** in magnetization M with respect to applied field H (or magnetic field B with respect to applied field H) and a ***saturation magnetization***. An example of such a curve, also known as a hysteresis loop, is shown in Figure 6 (note that in the figure, magnetic field B is used in place of M, giving a B vs. H curves). From the curve, it is seen that as applied field is increased, there comes a point past which no further increase in magnetization is achieved. This magnetization is the saturation magnetization M_{sat} (equivalent to B_S in the figure). It is also seen that ferromagnetic materials which have been exposed to a magnetic field show a magnetization at zero applied field, known as ***remanent magnetization*** M_r (also known as residual magnetization; equivalent to B_r in the figure). A body with a large remanent magnetization is called a permanent magnet (to distinguish from an electromagnet). To temporarily reduce remanent magnetization to zero, a ***coercive field*** H_C must be applied. To permanently remove the magnetization, the body would have to experience multiple hysteresis loops until the last loop terminates at the origin of the plot. Practically, this can be accomplished with a “degaussing coil”. Alternatively, the ***Curie temperature*** of the material may be exceeded (described later). The origins of hysteresis and saturation come from the domain structure of ferromagnets, which will now be discussed.

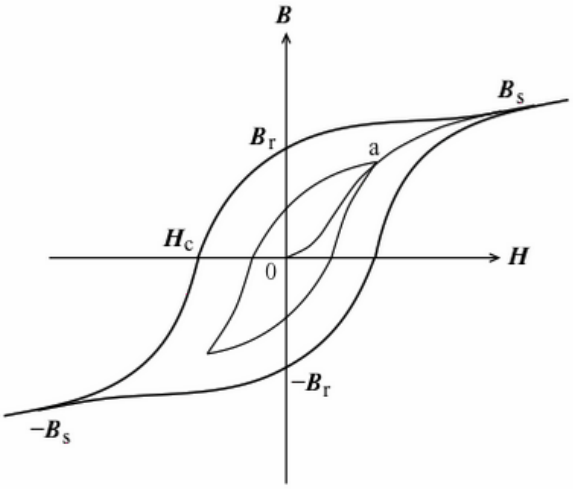

Figure 6. Magnetic field vs. applied field for a ferromagnetic material, exhibiting the characteristic hysteresis behavior. Reprinted from Spaldin NA, Magnetic Materials: Fundamentals and Applications, second ed. Cambridge: Cambridge University Press, 2010 under blanket permission of Cambridge University Press. [28]

Ferromagnetism results in the "cooperation" of magnetic moments by alignment in one direction within an energetically limited volume, called a magnetic domain. Magnetic domains within a material are schematically shown in Figure 7. The size of these domains, which is typically on the order of 1 – 100 μm [26], is determined by competition between magnetostatic energy and exchange energy: the former reduces the size of a domain due to the lower energy of the external magnetic field created by the domain, while the latter increases the size of a domain due to lower energy caused by alignment of the spins. Domains within a crystal are separated by a domain wall (also known as a Bloch wall), which is a continuous gradient in the orientation of the magnetic moment on the scale of hundreds of atomic distances (in iron) [26] [27]. Despite the presence of domains, a material may have zero magnetic moment if domains distribute in such a way that no external magnetic field is present. This is called a closure structure and occurs when a material is cooled from the Curie temperature [27] (described later) in the absence of a magnetic field (e.g., in newly solidified material). However, the "pinning" of magnetic domains by defects likely is the reason that a closure structure does not form spontaneously in a magnetized body.

Importantly, magnetic domains are responsible for the saturation magnetization behavior in ferromagnetic materials. As the applied magnetic field is increased, the magnetic moments of

domains align, and favorably oriented domains may potentially grow. The resulting net magnetic moment, taken per unit volume or per unit mass, is referred to as magnetization. When an entire crystal is covered by one domain, technical saturation is reached. However, a further increase in magnetization can be seen. This is explained by the higher field strength aligning those spins whose axes of rotation deviated from the domain's alignment due to "thermal activation" [26].

As temperature increases, thermal energy reduces the alignment of moments and eventually causes a transition to paramagnetism. The temperature at which this transition occurs is called the Curie point. As mentioned, domains (domain walls) can become pinned at defects, and pinning must be overcome by application of increased field. This restriction on domain motion is the origin of *M* vs. *H* hysteresis in ferromagnetic materials. Additionally, magnetic anisotropy also plays a role in saturation behavior, especially in polycrystals.

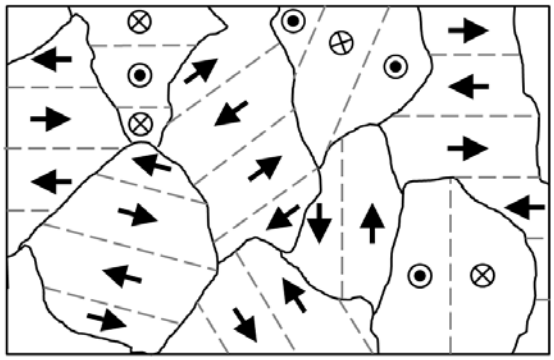

Figure 7. Simplified schematic of ferromagnetic domains in a polycrystal, with magnetic moments indicated by arrows. The boundaries between domains are shown as dashed lines. The moments are arranged in such a way that the net magnetic moment of the body is zero.

Due to their structure, crystals exhibit ***magnetic anisotropy***. Anisotropic magnetic properties include the magnetic permeability along a crystallographic direction and, for ferromagnetic behavior, the difference in the applied magnetic field required to reach saturation magnetization along a crystallographic direction. While the saturation magnetization does not vary with direction, the applied magnetic field required to reach saturation does. Taking the area underneath the curve on an *M* vs. *H* plot results in a quantity, with units of energy, that is useful when describing the anisotropy of saturation magnetization. This quantity is called magnetic

anisotropy energy, denoted *K*. Generally, structures with lower symmetry exhibit a greater degree of anisotropy. As seen in Figure 8, materials may possess a direction of minimum *K*. Such a direction is known as an ***easy direction*** or ***easy axis***. If a plane contains a constant *K* which is also the minimum value of *K*, the plane is known as an ***easy plane*** [29]. Martensites of Ni-Mn-Ga have either an easy axis or easy plane, depending on their modulation, as indicated in the next section. An additional note will be made to relate magnetic anisotropy to saturation magnetization: in a grain of a polycrystal exposed to increasing applied field, a domain aligned with an easy direction will grow to cover the entire grain, and then the aligned spin of the domain will rotate until it is parallel with the applied field. When this process has completed for all grains, saturation is reached within the polycrystal.

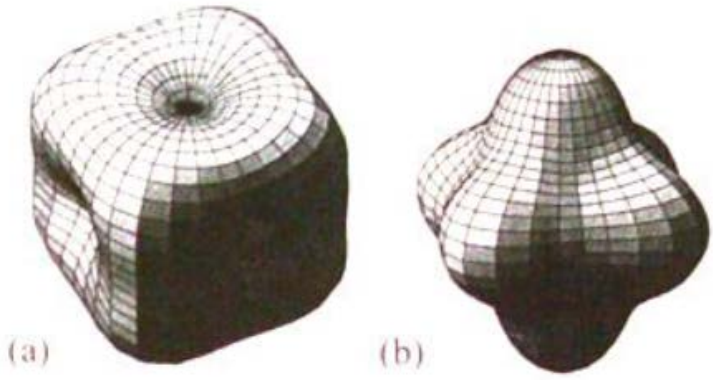

Figure 8. Surfaces of equal magnetic anisotropy energy for single crystals of (a) iron and (b) nickel. Reprinted from Modern Magnetic Materials: Principles and Applications by Robert C. O'Handley with permission of John Wiley & Sons, Inc. Copyright © 2000 by John Wiley & Sons, Inc. All rights reserved. [29]

Stress and magnetization are coupled in ferromagnetic materials due to magnetic domains and magnetic anisotropy. A ferromagnetic body placed in an applied field will experience lattice strains if the material is also magnetically anisotropic. This effect is referred to as ***magnetostriction***. The inverse effect is ***piezomagnetism*** [26], and is also known as the inverse magnetostrictive effect. Piezomagnetism is the change in susceptibility of a material under applied stress. In MSMA research, the stress generated by magnetization and the resulting force on twin boundaries has been analyzed [30], and is known as a ***magnetostress***.

1.6 PHASES OF NI-MN-GA

Considering compositions of interest in the literature (within 10 at % of Ni_2MnGa for each component) and near-room-temperature, Ni-Mn-Ga occurs as either austenite or as one of a group of martensitic structures. As in other systems, austenite is the name used for a high temperature phase, while martensite is a low temperature, non-cubic phase.

The path from the melt to the near-room-temperature phases will now be described. Ni-Mn-Ga compositions in the vicinity of Ni_2MnGa exist at high temperatures after solidification as the B2' phase [31], which can be viewed as Ni atoms at the center of a simple cubic unit cell with Mn and Ga at the corners (or alternatively, as two interpenetrating primitive cubic lattices). Upon further cooling, the material takes on the $L2_1$ structure, which is referred to as ***austenite***. This structure is described in section 1.4 and is illustrated in Figure 2. Magnetically, austenite is ferromagnetic below its Curie temperature, and contains many easy directions of magnetization. For Ni_2MnGa, $L2_1$ is the room temperature structure. Still further cooling brings about the martensitic transformation, whose completion leaves the material in one of three lower-symmetry structures, all of which are collectively referred to as martensite.

The three ***martensite*** types are distinguished by chemical ordering and lattice ***modulation***. The three structures are referred to as NM (nonmodulated), 10M and 14M; alternatively, the latter two have also been called five-layered (5M) and seven-layered (7M) martensites respectively. The 10M and 14M structures are shown in Figure 9. Modulated crystal structures have a repeated variation in substitution or position which is not otherwise described by the crystallographic point group. If this variation does not repeat in a length which is a multiple of the unit cell which would be used for the point group (the unit cell that would be used if there were no variation), it is termed ***incommensurate modulation***. Detailed discussions of approaches to determining, modeling and describing the martensite structures are given in [32–36]. Nonmodulated martensite exhibits no chemical ordering and no modulation in structure, while the latter two martensites possess chemical ordering and modulation which repeats every ten and fourteen layers, respectively (five and seven, if the alternative definition is used). The structures of the latter two martensitic phases are often simplified as possessing a pseudo-tetragonal and pseudo-orthorhombic unit cell, respectively. A view of the pseudo-orthorhombic unit cell along [110] is shown in Figure 10; when translated and rotated to

overlap with the modulation, this cell recreates the full structure's unit cell. Because the pseudo-cell is in effect an "average" unit cell of the structure, it can be identified in diffraction experiments (especially laboratory x-ray diffraction, where often only the most intense peaks are visible). The resemblance of this unit cell to the $L2_1$ structure is also notable. Finally, the nonmodulated phase belongs to the tetragonal crystal system. The structures of the austenite and martensite are summarized in Table 2. The lattice parameter of the austenite of Ni_2MnGa has been measured as 5.82 Å [37], while lattice parameters of the martensite structures are given in

Table 3. However, it should be noted that the structures of martensitic phases is debated in the literature, as discussed later in this section.

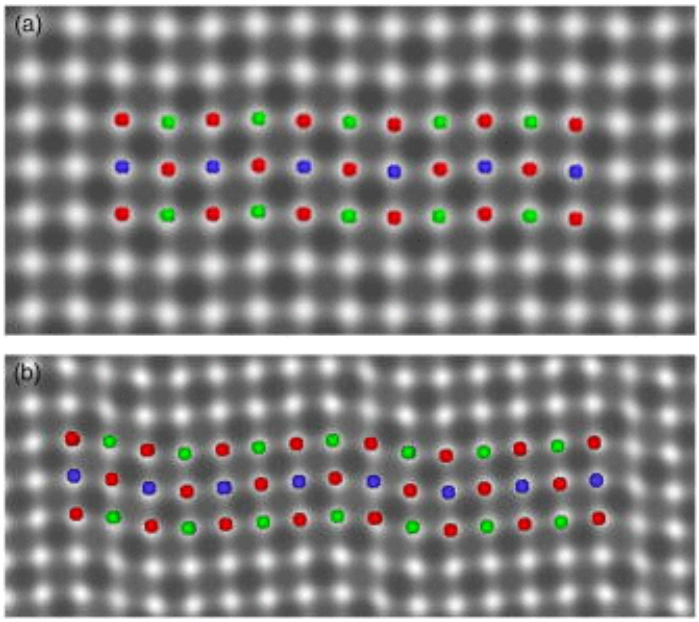

Figure 9. Model structures of (a) 10M martensite viewed along [010], and (b) The 14M martensite viewed along [010] (reprinted from [33]). Modulation is difficult to discern but present in (a). The overlaid positions (in color) correspond to one model, while the simulated TEM image which forms the background was formed using a slightly different model. Reprinted from "Long-period martensitic structures of Ni-Mn-Ga alloys studied by high-resolution transmission electron microscopy" by Jaume Pons, Rubén Santamarta, Volodymyr A. Chernenko, and Eduard Cesari, Journal of Applied Physics 97, 083516 (2005), with the permission of AIP Publishing.

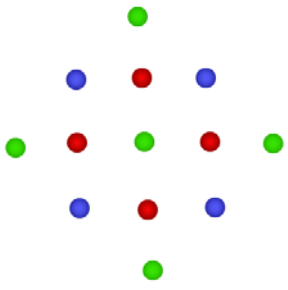

Figure 10. Pseudo-orthorhombic unit cell for 14M martensite. This cell is partially visible in Figure 9 (positions are approximate). Adapted from [33] **and** [12]**.**

Table 2. Structures of the austenite and martensite phases of Ni-Mn-Ga. Information compiled from [12]**,** [32]**,** [38]**, and** [39]**.**

	Phase			
	Austenite	**Martensite**		
Martensitic structure		NM	10M	14M
Alternative descriptor for martensitic structure		2M [35]	5M	7M
Stacking sequence in Zhdanov notation (when appropriate unit cell chosen) [32]			$(\bar{3}2)_2$	$(\bar{5}2)_2$
Lattice system	cubic	tetragonal	monoclinic	monoclinic
Space group (various approaches)	$Fm\bar{3}m$		Pm, C2/m, I2/m, Fmmm	Pm, C2/m, I2/m, I4/mmm
Space group number (various approaches)	225		6, 12, 12, 69	6, 12, 12, 69
Strukturbericht	$L2_1$			
Pseudo-unit cell's lattice system			tetragonal	orthorhombic

Table 3. Example lattice parameters and angles of Ni-Mn-Ga (as reported in [33]**,** [37] **and** [40]**).**

Martensite structure	Model and/or composition used	Lattice parameter (Å)			Lattice angle (°)		
		a	b	c	α	β	γ
NM	Tetragonal, $Ni_{52.1}Mn_{27.5}Ga_{20.6}$ [40]	5.46		6.58	90		
NM	Tetragonal, $Ni_{46}Mn_{24}Ga_{22}Co_4Cu_4$ [1]	5.55		6.36	90		
10M	Full structure, "Modulation" in [33]	4.17	5.54	20.8	90		
	Full structure, "Stacking" in [33]	4.24	5.66	20.5	90	90.5	90
14M	Full structure, "Modulation" and "Stacking" in [33]	4.23	5.51	29.4	90	93.5	90
10M	Pseudo-tetragonal [37]	5.94	5.94	5.59	90		
14M	Pseudo-orthorhombic, $Ni_{50}Mn_{29}Ga_{21}$ [37]	6.07	5.83	5.53			
14M	Pseudo-orthorhombic, $Ni_{50}Mn_{30}Ga_{20}$ [37]	6.12	5.80	5.50			

The properties of these phases which are specifically relevant to the magnetic shape memory effect (MSME, described later in section 1.8) include magnetic classification, magnetic anisotropy, anisotropy of the unit cell dimensions, and twinning stress. All of the phases are ferromagnetic (at temperatures below the relevant Curie points). Twinning is particularly important to the MSME, as the presence of deformation twins and the ability to move their boundaries results in twin variants with different but crystallographically related orientations. The growth of one twin variant versus another amounts to a net reorientation of the lattice, which coupled with the anisotropic dimensions of the unit cell, results in overall deformation of the material (further described in section 1.8). The 10M and 14M martensites easily form twins with mobile boundaries upon application of an external force (induced magnetically or mechanically), while the NM martensite forms twin boundaries which are generally not movable by the limited magnitude of magnetically induced stress (in the case of Ni-Mn-Ga without additional elements). A discussion of how the relative magnitude of starting and finishing twinning stresses compared

to the magnetically induced stress affects MFIS magnitude is given in [32]. However, the highest magnitude of MFIS was observed in NM martensite in Ni-Mn-Ga-Co-Cu [1]. The remaining properties are also summarized in Table 4. However, it should be noted that the data in this table are representative values that were obtained from a small number of studies.

Table 4. Selected properties of Ni-Mn-Ga martensites.

Martensite structure	**NM**	**10M**	**14M**
Easy axis or easy plane of magnetization	ab	c	c
Magnetic anisotropy energy (10^5 J/m^3) [32]	-2.03	1.45	1.6 (K_a), 0.7 (K_b)
c/*a* ratio (for 10M and 14M, pseudo-unit cells are used)	1.15 (Ni-Mn-Ga-Co-Cu) [33], 1.21 (Ni-Mn-Ga) [40]	0.94 [37]	0.90, 0.91[37]
Maximum demonstrated MFIS, %	0.17 (Ni-Mn-Ga) [41]	6 [42]	9.7 [1]

Interestingly, the determination of which martensite structure is present under given conditions is a contested and complicated subject. Results from various experiments show disagreement on which martensite is present at a specified composition (at room temperature) – see Figure 6.18 of [12]. One might argue that measurement of sample composition lacks sufficient accuracy in many studies, especially where energy dispersive spectroscopy (EDS) was used. A change of just 0.5 at% in the composition, when near the (contested) boundary between structures (on a plot of composition), can move the martensite safely to a different structure (again referencing Figure 6.18 of [12]). The uncertainty in EDS measurements can be on the order of 1 at%, so it may simply be that the compositions reported do not correspond to the structure observed. Further ideas based on the imperfection of experiments include the presence of residual stresses or defects (including impurities), unbeknownst to researchers or unquantified by them. Others may argue that the concept of variously modulated martensite structures may be misapplied or unnecessary (see “adaptive phase” and “nano-twining”). A review of data and

arguments for the existence of modulated phases, including commensurate and incommensurate modulation, versus the concept of an adaptive phase, is found in the introduction of [35].

Transformations among the phases and structures of Ni-Mn-Ga will now be discussed. It is noted that the austenite ($L2_1$) does not grow by precipitation, but rather is likely a second-order phase transformation. In one study [31], data on quenching of annealed Ni_2MnGa from the B2' phase showed that the transformation to $L2_1$ happens in under 0.5 s. Additionally, retained B2' phase was not definitively observed nor ruled out, but its possible proportion was thought to be small.

Premartensitic transformations, observed in a limited range of compositions above the martensitic transformation temperature while cooling austenite, are changes in the vibrational state of the lattice (phonons) without a decisive change in the crystal structure. This is referred to as "phonon softening" and has been observed as a change in the elastic modulus [43].

Transformation from austenite to martensite, known as the ***martensitic transformation***, occurs upon undercooling (to overcome non-chemical energy barriers) and over a finite temperature range. The range is referred to as the "breadth" of the transformation. Transformation does not occur instantaneously across a crystal, and has been observed to proceed by the growth of self-accommodated martensite variants (twins). This was observed in [24], where the authors called the twins "platelets" (see Fig. 5 of that reference). Richard et al. [44] found that when transforming from austenite to a 14M structure, the breadth is greater than when transforming to a 10M structure. The authors reasoned that the larger incompatibility between the 14M and austenite lattices results in a greater strain energy barrier, thus broadening the transformation. Transformation in the reverse direction, from martensite to austenite, is known as the ***austenitic transformation***. Overcoming non-chemical energy during transformation results in undercooling or superheating during the martensitic and austenitic transformations, respectively, causing hysteresis in the transformation process and a difference in the martensitic transformation temperatures (M_s and M_f) and austentic transformation temperatures (A_s and A_f) (where *s* stands for start and *f* for finish).

Transformations between martensite structures are referred to as ***intermartensitic transformations***. It is also possible for intermartensitic transformations to overlap with the martensitic transformation. Some intermartensitic transformations may be examples of "phonon softening", as was discussed for premartensitic transformations earlier in this section.

1.7 PROCESSING OF NI-MN-GA

Processing routes for Ni-Mn-Ga and other magnetic shape memory alloys can be broken down primarily into methods which intend to produce a single crystal, and methods that do not. Single crystal growth methods include Bridgeman, Czochralski and Slag remelting and encapsulation (SLARE). Polycrystalline methods are much less common and more varied (excluding thin films). The most notable of these is the creation of foams by replication casting. Additionally, thin films have been produced by various methods and are largely polycrystalline, including at least one instance of epitaxial growth.

Most often, studies on Ni-Mn-Ga have obtained specimens by ***single crystal growth*** methods, including the Bridgeman method [20] [45], the Czochralski method [46], and the slag remelting and encapsulation (SLARE) method [47]. This is because the most touted behavior of MSMAs, the MSME, is for practical purposes inactive in a dense, non-textured polycrystal. The Bridgeman and SLARE methods involve moving a crucible with a seed crystal through a decreasing temperature gradient (out of the hot zone of a furnace) in order to slowly move a solidification front through the melt. The SLARE method (shown schematically in Figure 11) is particularly advantageous because it includes a fluxing slag. The slag protects the melt from the inert gas above the melt, reduces evaporation of low vapor pressure elements, and draws impurities out due to a high solubility of those elements. Thus, use of SLARE can result in lower gas porosity, smaller overall compositional change relative to the initial charge, and lower impurity content [47].

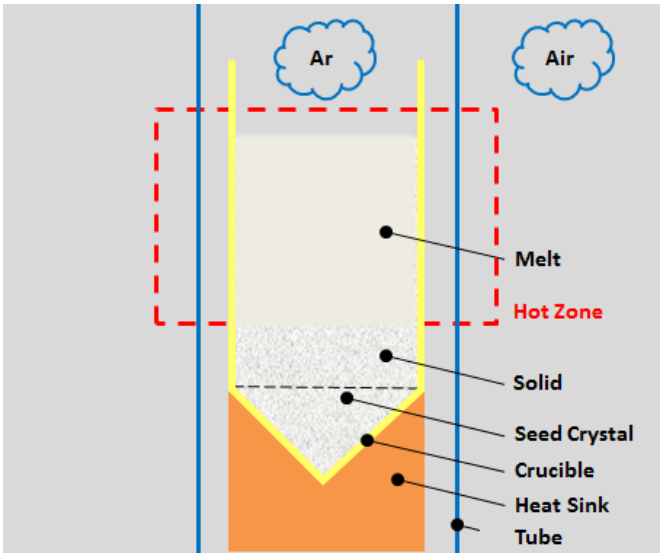

Figure 11. Schematic of a single crystal growth furnace.

Successful single crystal growth has a great ***advantage*** in the quality of the material produced. Successful single crystal growth results in a piece with no distinct grains (high-angle grain boundaries). However, small-angle grain boundaries have been observed in Ni-Mn-Ga single crystals [48].

While necessary to produce single crystals, the crystal growth methods have interrelated ***drawbacks*** in chemical segregation and productivity. Because Ni-Mn-Ga solidifies over a distinct temperature range (measured in one study as 18 °C for Ni_2MnGa) and also due to natural convection, chemical segregation occurs during single crystal growth [49]. The segregation is of a macroscopic scale, and results in compositional gradients along the growth direction of the single crystal. Depending on the method used, evaporation from the melt may also be significant – in Ni-Mn-Ga, Mn is said to be the element of concern ("loss of Mn" [12], "loss of volatile elements, like the manganese in Ni-Mn-Ga" [47]). The result of even a successful crystal growth is a single crystal with compositional gradients parallel to the solidification direction, and efforts at homogenization are not completely successful at removing these gradients. Keeping the sensitivity of the Curie temperature, phase transformation temperatures and room temperature structure to composition in mind, MSMA functionality is affected along the length of the crystal. Additionally, due to the temperature gradient perpendicular to the length of the crystal, the cross-sectional center of the crystal shows a greater number of defects. The likelihood of defects

increases as the temperature gradient decreases, and the gradient decreases with increasing crystal diameter [47]. Viewing crystal growth as a technological process, these effects reduce the yield of valuable product from the process, compounding its already high cost. This reality has been noted in the literature, for example in [50].

Grain boundaries and misorientations neighboring grains largely inhibit the MSME [50], and so, ***polycrystals*** do not readily experience an MFIS. However, an approach pioneered by the research groups of Dunand and Müllner overcame this barrier by creating foams with designed grain and pore sizes [50–53]. By creating single grains which span struts (the structural units of the foam), the barrier to the MSME is removed for individual grains, and an overall strain for the polycrystalline foam becomes possible.[1] In what is known as the replication method or replication casting, foams are created by infiltrating a ceramic powder inside with liquid Ni-Mn-Ga, and then dissolving the ceramic particles (which act as placeholders) with etchants.

Thin films of Ni-Mn-Ga have been processed by magnetron sputtering [54,55], ion beam sputtering [56], pulsed laser deposition [57], and laser beam ablation [58]. Studies of thin films have also reported epitaxial growth [59–61].

One study has experimented with a composite structure consisting of Ni-Mn-Ga particles in a polymer matrix [62].

Other processing strategies are rare and generally only occur as single instances in the literature. However, if a method involves ***high cooling rates***, it may have special relevance to the topic of this thesis. Rapid solidification of Ni-Mn-Ga has been investigated in melt-spinning followed by sintering [63], in suction casting [64], and incidentally in laser drilling [65] [66]. Melt-spinning was often used to produce samples for fundamental investigation of Ni-Mn-Ga, and in these cases processing was not the focus of the studies. In [63], a textured sample with satisfactory ferromagnetism was found. In [64], a martensitic transformation temperature for Ni_2MnGa was found that was lower than that of the arc-melted sample in [24].

---

[1] One may wonder how foam struts with a random or near-random orientations can produce a net strain. With the help of the discussion of MFIS in section 1.8, it can be understood (for a two-dimensional view) that struts will only contribute a positive strain along the direction perpendicular to the magnetic field. In the worst case of a 45° minor angle between the *c*–axis and the field line, the unit cell will still contribute a positive strain perpendicular to the field line. At least in the two-dimensional model, no "cancelling" of strains should occur. See Supplementary Figure S5 of [52].

It must be noted that rapid solidification is a relative term. The technologies mentioned achieve various cooling rates, and often, the cooling rate is not determined experimentally. For suction casting, one numerical study reports cooling rates on the order of 100 °C/s with Fe-Ni and Al-Cu alloys [67]. In general, processes which achieve melting by a laser heat source may involve the highest cooling rates – one set of authors claims that the Laser Engineered Net Shaping (LENS) process (see sections 1.9 and 2.1.1) produces cooling rates of 10^3 to 10^5 °C/s [68]. As cooling rate has a significant influence on solidification microstructures, any comparison to literature would do well to be informed about cooling rates. Unfortunately, cooling rates are often not reported, likely due to the experimental difficulty of measuring them.

Biffi and Tuissi [65] conducted blind and through-hole ***laser*** drilling experiments of 1.8 mm $Ni_{46}Mn_{27}Ga_{27}$ plates, and observed effects on the composition of the perimeters of, and of resolidified material near the perimeters of, entrance and exit holes due to the laser beam. While the perimeters of entrance holes, shielded by inert gas during drilling, showed Ga loss and compositional change limited to approximately 1 at. % in any element, the authors noted the presence of a formation adjacent to the entrance and exit each with much more dramatic compositional changes. The formations consisted of resolidified material which was presumably ejected from the hole; both were found to have Mn enrichment by EDS analysis of their surface. In a formation at an entrance hole, Mn content was found to be 53 at%, while Ni and Ga were lost but approximately retained their original ratio. At the exit hole, the formation's surface was found to consist of approximately 97 at% Mn. Differential scanning calorimetry (DSC) revealed a decrease in the austenitic/martensitic transformation temperatures (although it is not clear what portion of the laser-drilled plate was used for analysis). No change in the corresponding peak breadth or shape was seen, and no other peaks were seen. The shift was attributed to compositional change (loss of Ga), while the lack of a distinct peak was taken as evidence of a lack of secondary phases forming (but perhaps the contribution of a sufficiently small volume of a second phase at the edge of the hole would not create a visible peak). Furthermore, the authors noted cracks which span the resolidifed surface of blind holes and are visible at the perimeter of through-holes. The cracking was categorized as brittle, and was attributed to the thermal effects of laser drilling on a material which is known to be brittle.

Craciunescu et al. [69] subjected $Ni_{46}Mn_{34}Ga_{20}$ and $Ni_{48}Mn_{32}Ga_{20}$ samples to a laser beam in 2011, predating [65]. Using a pulsed wave laser and two power levels, they achieved

both penetration and spots, much like through-holes and blind holes. By EDS, the authors found that the perimeter of a spot was enriched in Mn, while the center was similar in composition to the base material. It was assumed that the spots solidified from the perimeter to the center, leaving the center as the last place to solidify. The center displayed an irregular area of higher brightness on backscattered electron images, which seemed distinct from the surrounding spot material. Moving radially outward from the center, the brightness gradually changed until the perimeter was approached. At the perimeter the brightness changed more rapidly, thus indicating segregation of an element. On EDS line scans shown in Figure 12, it is seen that the perimeter features a maximum in Mn signal, which decreases to the base material level as the surrounding base material is approached or as the spot is approached. The authors report that composition follows a "concentric" pattern in the spot. Furthermore, the large signature of O, combined with the enrichment with Mn, was taken to indicate the presence of manganese oxide. This finding was treated as very significant because an oxide inclusion has serious implications for MSME functionality in its vicinity. In contrast to the work of Biffi and Tuissi [65], the material presumably ejected from through-holes was seen to be 94 at% Ni, and not primarily Mn. Finally, cracking was also observed and attributed to the brittleness of the Ni-Mn-Ga system.

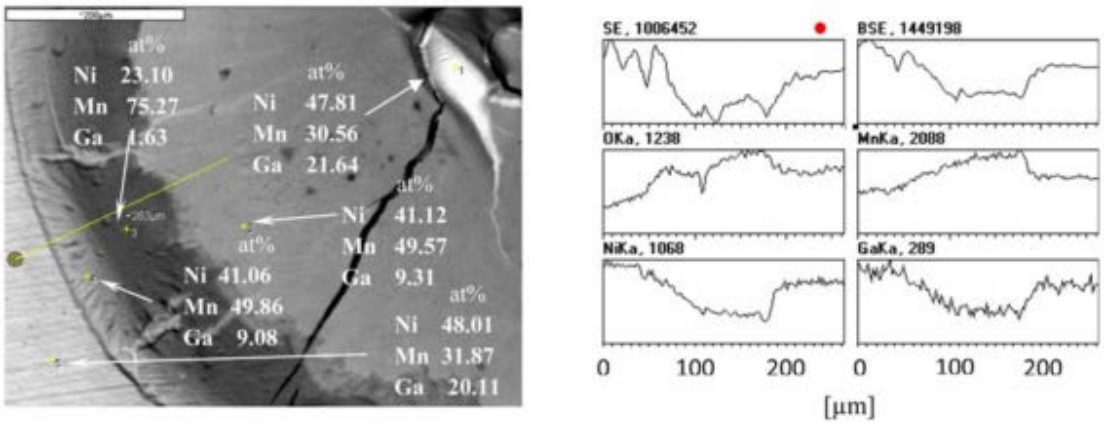

Figure 12. Compositional variation in one quarter of a circular laser spot, reprinted from [69]**. The plots on the right are the result of an EDS line scan which proceeded along the yellow line in the left-center area of the image. Reprinted from Optics and Lasers in Engineering, volume 49, C.M. Craciunescu, R.M. Miranda, R.J.C. Silva, E. Assunção, and F.M. Braz Fernandes, Laser beam interaction with Ni–Mn–Ga ferromagnetic shape memory alloys, pages 1289-1293, Copyright 2011, with permission from Elsevier.**

With exception of thin film deposition studies (which by definition put material through the vapor phase), the two articles just noted are the only publications on the effect of laser processing on magnetic shape memory alloys (including Ni-Mn-Ga(-x) alloys) to the author's knowledge. It is noted that neither study measures nor estimates the cooling rate. Even if the authors were interested in cooling rates, the experimental difficulty of such a measurement likely would have discouraged them from doing so.

1.8 MAGNETIC FIELD-INDUCED STRAIN

The magnetic field-induced strain (MFIS) phenomenon, also known as magnetically induced reorientation (MIR), will now be explained in more detail. MFIS is an example of magnetoplasticity, meaning that a plastic deformation is brought upon by interaction with a magnetic field. Because the deformation is plastic, the material will not revert to its pre-deformation state once the magnetic field is no longer present. However, it has been stated previously that MFIS is reversible; MFIS may be reversed by application of a magnetic field in a specific, orthogonal direction, or by application of a compressive mechanical force in the antiparallel direction [10].

Compiling some of the items mentioned in previous sections, we see that the necessary conditions for MFIS include ferromagnetism, magnetic anisotropy, the presence of deformation twinning and a low stress to move the twin boundary, and a unit cell with a non-unity c/a ratio. A more succinct explanation of requirements for MFIS is found in [60]: "The basic requirement of MIR is high magnetocrystalline anisotropy and a particular microstructure of differently oriented twin variants connected by an easily movable twin boundary". To compare this quote with the requirements set out previously, "magnetocrystalline anisotropy" is a magnetic anisotropy which correlates with the crystal lattice, while "high" may essentially require ferromagnetism (because ferromagnetism generally generates much higher forces than other magnetic mechanisms). The quote also indicates that the microstructure of twins is important, as the orientation and scale of twins affects the magnitude of MFIS.

The process which leads to MFIS will now be described step-by-step but in a simplified way. Starting with a true single crystal, no twin boundaries are present (only a single variant is

present) (Figure 13(a)). The *c* axis is the easy axis of magnetization, and if a magnetic field is applied perpendicular to this axis, a second twin variant may nucleate and grow (Figure 13(b)) until the entire crystal is consumed by the second variant (Figure 13(c)). Nucleation is thought to occur at defects in the lattice. The nucleation and growth of the second twin variant occurs by disconnection – a crystallographic defect which consists of atoms leaving the equilibrium position in one lattice and moving by a fraction of an interatomic distance into the equilibrium position in another (Figure 14). This movement is termed a lattice shear. Twin variants are by definition two lattices with a specific orientation relationship. Critically, the orientation relationship is such that the *c* axis in the second lattice is (nearly) orthogonal to the *c* axis of the first lattice. A simplified way to view the growth of the second twin variant (lattice) under a strong magnetic field as favorable is by noting that the second variant's lattice has its easy axis of magnetization parallel to the magnetic field direction. Thus, the second variant achieves a higher magnetization at a given field strength (this can be seen for the various orientations in Figure 15). Another way to under the growth of the second twin variant is through the force exerted on the twin boundary plane that results from a shear stress induced by the magnetic field on the boundary [30]; the direction of this force is such that the twin variant with its easy axis aligned with the magnetic field will grow. A development of the magnetostress concept is given in [30].

As the second twin variant grows, an overall reorientation of the lattice of the crystal takes place (notably, this reorientation occurs without the diffusion of atoms). It is seen that because of the non-cubic nature of the unit cell of a martensite - specifically due to its *c/a* ratio - the reorientation results in a non-negligible change in the overall dimensions of the crystal. Specifically, the change is an extension along the original direction of the original *c* axis and a contraction along the direction of the new *c*-axis (nearly perpendicular to the original *c* axis). Finally, it is important to understand that real samples contain many twin variants, and the magnitude of MFIS is highly dependent on the detailed microstructure which these twin variants form [12], including "coarse" and "fine" twins, and their orientations and scales. "Training" of an MSMA is a process which aims to establish a favorable arrangement of twins. Cyclic actuation of an MSMA is essentially another form of training, and so, may lead to a progressive change to another arrangement of twins. For this reason, the magnitude of MFIS often varies over many cycles [10].

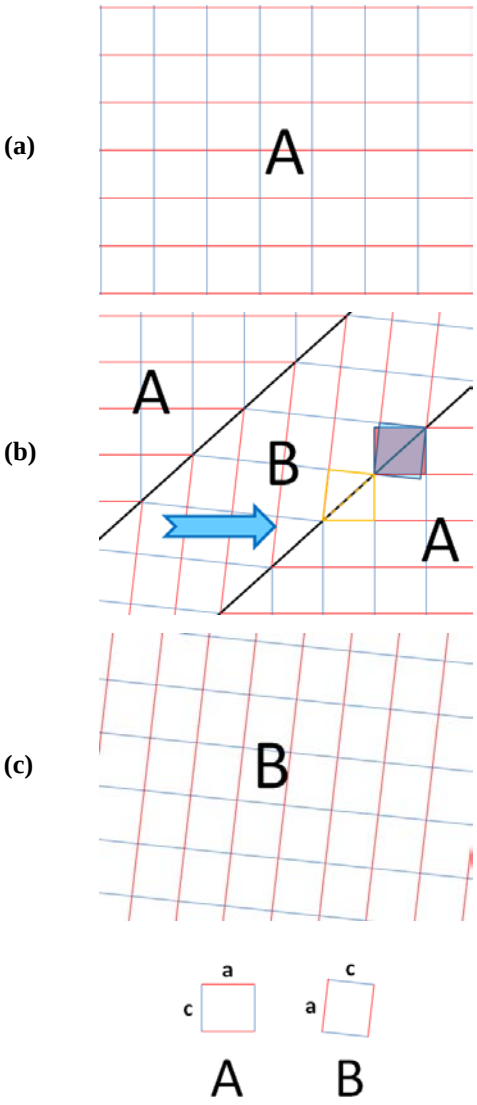

Figure 13. Demonstration of the MFIS process in a single MSMA crystal. (a) The crystal contains only a single variant, labeled A. (b) A second variant (labeled B) has nucleated and grows. The original pseudo-unit cell, approximately as it existed before the second variant, is highlighted in red. The second variant's pseudo-unit cell is highlighted in blue as it will exist once the twin boundary continues moving. Their overlap results in a purple color. The halves of pseudo-unit cells, which are in immediate contact with the twin boundary, are shown with an orange outline. (c) The crystal consists of only the second variant after growth is complete. The unit cell axes corresponding to each variant's pseudo-unit cell are shown at the bottom, and the magnetic field direction is shown with an arrow in (b). Adapted from [12].

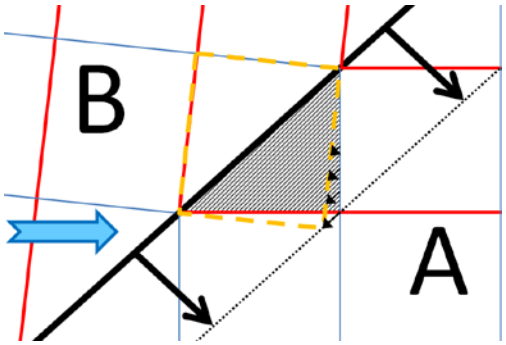

Figure 14. Schematic illustrating the lattice shear by which the twin boundary moves. The dashed, orange outline represents the new, full pseudo-unit cell which will be formed by twin boundary motion. The shaded area is that area of one half-pseudo-unit cell of the consumed variant (A), which experiences lattice shear and contains several atoms. As an example, the small arrows show the direction of shear for points lying along one edge of the half-pseudo- unit cell (of course, shear is not limited to only the shaded area). Finally, the dotted black line represents the new twin boundary after twin boundary motion. Adapted from [12]**.**

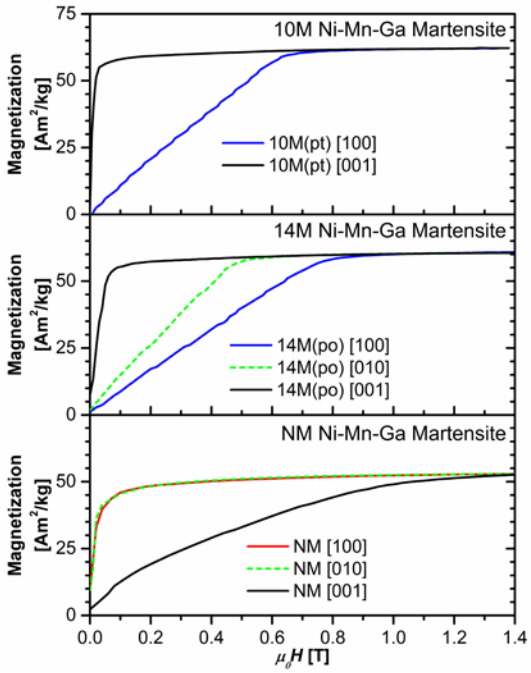

Figure 15. Magnetization vs. magnetic field strength data obtained by VSM for Ni-Mn-Ga single crystals along each orthogonal crystal axis of the pseudo- unit cells. Subplots show data for each of the martensite structures. Created with data from [12]**.**

As previously stated, MFIS is reversible. However, energy must be applied to an MSMA element to cause reversal. This is desirable in that the element will maintain its shape without a need for continuous energy application, and will do so even in the face of an opposing mechanical stress of magnitude lower than the twinning stress (the twinning stress for the configuration of the twin microstructure present; also, assuming that elastic deformation is taken as negligible). Thus, in order to reverse MFIS, a compressive mechanical stress must be applied along the direction of extension, or a magnetic field perpendicular to the field which caused the MFIS must be applied. Reversing the polarity of the original field is not sufficient, because it is a perpendicular reorientation of the easy axis which caused MFIS, and so only another perpendicular reorientation of the axis can reverse the MFIS. Furthermore, it can be seen that an easy axis is not influenced by the polarity of a magnetic field, but only by the difference in direction between the axis and the field [10]. Applying these lessons to a (continuously) rotating magnetic field, it can be seen that an appropriately oriented MSMA element will go through one complete cycle of MFIS and reversal during one half-rotation of the field. Thus, the element will experience two complete cycles for one full rotation of the magnetic field. This is demonstrated by the plot in Figure 16.

A rotating field is not the only way to cycle an MSMA element. Electromagnet windings could be positioned in such a way that a change in the field direction is achieved. In a design realized in actuators, a biasing (or restoring) stress is introduced to the element by a compression spring and an electromagnet with fixed direction is the only magnetic field source. However, it must be remembered that reversing the polarity of the field (applying an anti-parallel field) is not sufficient to reverse MFIS and so cannot cycle an MSMA element.

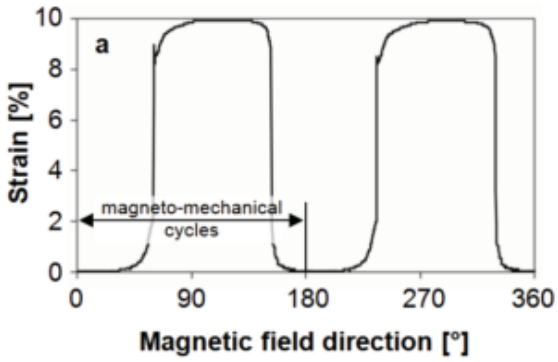

Figure 16. MFIS vs. direction of an applied, rotating magnetic field. Reprinted from "Large cyclic magnetic-field-induced deformation in orthorhombic (14M) Ni–Mn–Ga martensite" by P. Müllner, V. A. Chernenko and G. Kostorz, Journal of Applied Physics 95, 1531 (2004), with the permission of AIP Publishing. [10]

An additional note about maximum actuation frequency will now be made. While practical actuators built have been reported to achieve frequencies as high as 800 Hz [2], this limitation is not due to the MSMA element, but due to the high forces generated rapidly moving the load against which the element does work, and limitations of electromagnetic and/or mechanical components of the surrounding actuator system. Importantly, the velocity of twin boundary motion has been measured in one study as 82.5 m/s, with a response time of 2.8 µs [70]. Perhaps MSMAs might be able to actuate against a negligible load at much higher frequencies – if a magnetic field can be controlled appropriately at these higher frequencies and limitations from the rest of the system were removed. Making a simplified model of a rectangular element with *c* and *a* axes aligned with the macroscopic dimensions, and taking into account the response time, the twin boundary speed, and the fact that a single twin boundary would have to pass through the length of an element twice to complete one cycle, one can find that a hypothetical element as large as 45 mm x 10 mm (as an example) could still exceed an actuation frequency of 1 kHz. Of course, this treatment ignores inertial considerations (which would decrease the viable frenquency), and speaks of one twin boundary even though elements with fine (dense) twin structure are generally preferred [71] (which would increase the viable frequency). To conclude, even though the preceding discussion may be entirely hypothetical, actuators based on MFIS have already been demonstrated to achieve frequencies not reached by other active materials with comparable actuation strains (these include conventional shape memory alloys, shape memory polymers and piezoelectric polymers) [3].

1.9 ADDITIVE MANUFACTURING

Additive manufacturing (AM) is a set of processes which add material to a part in successive layers by using largely automated tools. While AM is colloquially referred to as "3D printing", the term AM is used to make clear that a process is capable of producing end-use parts, including dense, metal parts. Some synonyms for AM are listed in Table 6 at the end of this section. AM has seen continuous growth over the past 20 years or so [72] and is an outgrowth of rapid prototyping (RP) technology, whose beginnings trace back to the 1980s [73,74]. The touted benefits of AM [72] might be summarized in the categories of (1) design, (2) cost and environment, and (3) logistics or supply chain. More specifically, design advantages (1) may include increased freedom in part design which allows for improved function and/or reduced weight, and the possibility of novel microstructures and materials [73] (although many novel ideas are still largely in the research phase); cost and environmental advantages (2) may include reduced material waste, potential for reduced energy usage, reduced costs in some situations (for low production volumes, high-cost materials and difficult-to-machine materials); and logistical or supply chain advantages (3) may include highly responsive scaling of production, dramatically reduced lead time for first parts, and the possibility of producing parts near their location of use.

A multitude of AM processes is known today, as seen in Table 5. All of these proceses share one common, central feature: they create parts by adding material along specific geometric paths or patterns in many steps, until the part is complete. Paths or patterns are typically confined within a two-dimensional layer, allowing a three-dimensional part to be built layer-by-layer. This is done by either binding powder together without any melting and then post-processing the resulting part (***binder jetting***), or by directly applying an energy source to completely or partially melt powder particles (referred to here as "***direct***" processes). In both categories, many processes utilize a ***powder bed***, which pre-positions a layer of unmelted powder at the beginning of each layer (Figure 17). Some "direct" processes, known as ***powder feed*** or deposition processes, deliver powder to the location where energy is being applied simultaneously (Figure 18). In some deposition processes, a wire may be substituted for powder. Deposition processes are also well suited to repairing, adding features to, or coating/cladding existing parts. For the vast majority of "direct" processes, the energy source is either a laser or an electron beam. In many

direct powder bed processes, the energy source is not applied in a continuous path within a layer, but rather in a discontinuous pattern (in order to manage the buildup of heat).

Out of the advantages of AM given earlier, a vision for producing MSMA elements by AM might mainly focus on the available freedom of shape, paralleling the "design" and "difficult-to-machine materials" advantages of AM. However, it must first be demonstrated that the material properties that are important in MSMAs can be achieved when processing them by an AM method. For that reason, this thesis focuses mainly on the potential for AM to produce small-scale samples with desired properties. Thus, this usage has parallels with the potential AM advantage for "novel materials". It may also be possible that this work or future work might demonstrate unique microstructural properties of MSMAs processed by AM, thus paralleling the "novel microstructures" potential.

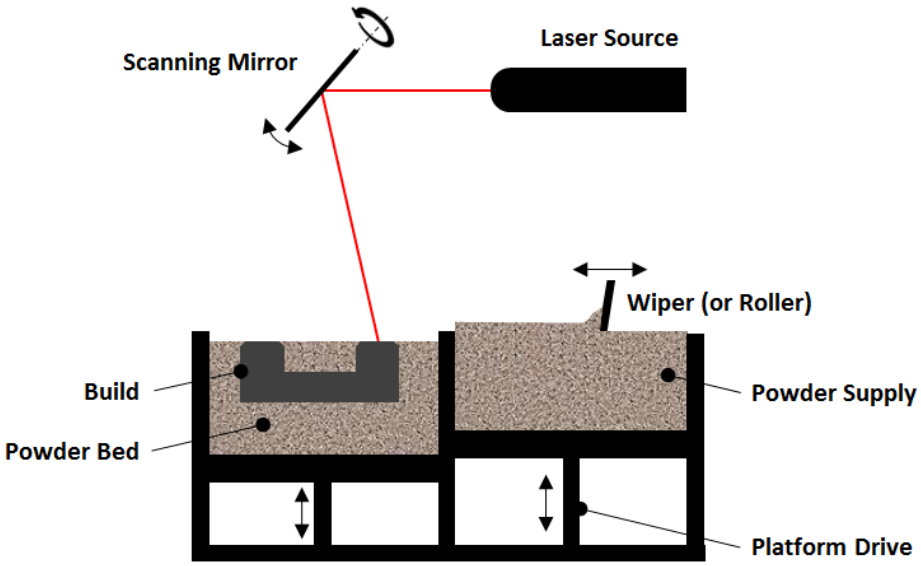

Figure 17. Schematic of a powder bed system with a laser energy source. Note that in this figure, the roller (rake, wiper) spreads powder over the powder bed to prepare for formation of the next layer. Adapted from [72]**.**

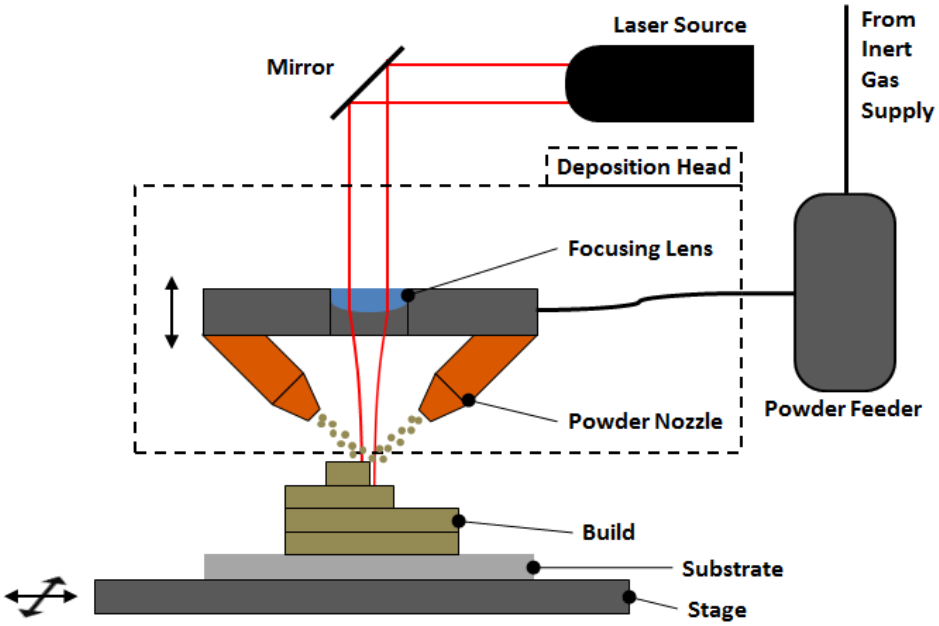

Figure 18. Schematic of a powder feed system. Adapted from [72].

Table 5. Industrial additive manufacturing (AM) processes regularly used for metals. Only the most prominent commercial processes are listed for brevity, while generic names and ISO/ASTM standard nomenclature allows for extension to less known and future processes. A large number of commercial processes are listed in [72]**.**

Binding or Direct	Powder bed or Deposition	(Deposition only) powder feed, wire feed, or both	OEM process name	OEM	Classification based on generic names from literature**	ISO/ASTM 52900:2015*** category
Binding	Powder bed		Binder Jetting	ExOne	binder jet printing (BJP)	binder jetting
Direct	Powder bed		Direct Metal Laser Melting (DMLM), Direct Metal Laser Sintering (DMLS)	EOS	Laser melting (LM), Laser sintering (LS)*	powder bed fusion
			Selective Laser Melting (SLM)	SLM Solutions		
			Electron Beam Melting (EBM)	ARCAM	Electron beam melting (EBM)	
	Deposition	Powder feed	Laser Engineered Net Shaping (LENS)	Optomec	Laser metal deposition (LMD)	directed energy deposition
			Direct Metal Deposition (DMD)	DM3D		
		Wire feed	Electron Beam Additive Manufacturing (EBAM)	Sciaky		

*Laser melting and laser sintering are essentially the same process from the equipment point of view, differing in only the power density delivered to feedstock. As indicated in the name, the two processes differ metallurgically.

**[73][74][72]

***Supersedes ASTM F2792

New possibilities with additively manufactured parts are not limited only to geometry, but also extend to controlled changes in composition (by mixing powders) and novel and optimized microstructures (by varying process parameters).

The distinguishing features of AM processing by "direct" methods are very high cooling rates (e.g. $10^3 – 10^5$ °C/s [68] [75]), highly directional heat transfer, reheating and even remelting of previous layers, and the presence of distinct lines and layers in the finished part. Additionally, for most processes, these lines and layers begin as powder. These processing characteristics lead to ***rapid solidification microstructures*** (characterized by micro-segregation, dendritic growth and fine features), ***directional grain growth*** (esp. resulting in columnar grains oriented perpendicular to layers and potential for epitaxial growth), a ***complex thermal history*** which is dependent on part geometry and the path taken by the heat source (and which can alter previous rapid solidification microstructures to a various degrees in various regions of the part), and the possibility of ***porosity*** (originating from within particles, or from incomplete melting and/or gas entrapment between particles or layers).

While this thesis does not focus on the production of industrial parts, the potential of AM technology for processing MSMAs is the central theme. It is recognized that AM processes which are capable of full melting of metals from a powder feedstock could be used to produce MSMA samples. Processes which require small amounts of powder are particularly useful as tools for investigation. For this reason, powder feed processes are well suited to the experimental work in this thesis. Laser Engineered Net Shaping (LENS) was used to produce samples for this work, and is described in detail in section 2.1.1.

Table 6. Selected synonyms for additive manufacturing.

Selected synonyms for additive manufacturing
rapid manufacturing, free form fabrication, direct digital manufacturing, 3D printing

2.0 EXPERIMENTS

2.1 DEPOSITION OF SAMPLES BY DIRECTED ENERGY DEPOSITION

2.1.1 Laser Engineered Net Shaping

The samples in this work were created by a LENS 450 additive manufacturing (AM) system. The advertised industrial uses of the LENS® family are repair, rework, addition of features to existing parts, building of new parts, and potentially materials development. These systems successively deposit material in order to build a part of a specified three-dimensional shape. Deposition is accomplished by melting a powder (sometimes referred to as feedstock). Initially, deposition happens on a substrate material, which then participates in a metallurgical joint with the deposited material – much like a weld bead on a plate. Thereafter, the system may deposit upon previously deposited material, resulting in a "building up" of material. Each pass at a new vertical position is called a layer. By controlling the location of deposition according to a set of instructions, the system can create three-dimensional geometries – within certain limits. This process typically achieves full melting within the material deposited, in addition to melting some of the substrate material. One may think of the system as a welding machine which, instead of joining two workpieces, continually deposits filler metal in a computer-controlled pattern in order to add features to a workpiece. When the desired material is substituted for the words "filler metal", the analogy essentially becomes reality. For this reason, the solid material resulting from one pass of deposition may be referred to as the weld bead or deposition bead.

A notable feature of many AM methods is a rapid cooling rate from the liquid phase. Concerning the cooling rate experienced by material in the LENS process, one set of authors wrote that it ranges from 10^3 to 10^5 °C/s [68]. Another group, using numerical simulation and experiments with stainless steel, found the range to be 10^3 to 10^4 °C/s [75].

In this work, a major advantage of the LENS (which may extend to other powder feed methods) is the ability to begin a build with very little material. This is because only a small amount needs to be present in the powder feeder (described later) for deposition to take place, while powder bed methods require enough powder to completely fill several layers of the bed, if not more.

2.1.2 LENS® 450 system specifics

The practical aspects of the functionality of the LENS 450 will now be discussed. First, the powder feeder mechanism will be described, followed by the deposition head, the chamber and working area, and the control interface. Figure 19, below, is a photograph of the system used in this work, and a general schematic that is fully applicable to the LENS 450 is shown in Figure 18 of section 1.9.

Figure 19. Optomec LENS 450.

The path that the powder takes to the deposition head can be traced in the aforementioned figure (Figure 18), and starts at one or more powder feeders. A powder feeder is a mechanism which causes powder particles to become entrained in a carrier gas (typically argon) for later

delivery to the melt pool. The powder feeder consists of a “hopper” and a core. The hopper is positioned above the core, and includes a funnel-shaped connection to the core. Powder is loaded into the hopper, and flows into the core gradually to replace powder which has been fed. The core consists of a cylindrical chamber at the back of which a specialized wheel, called a wiper, turns. As the wheel turns, holes in its thickness collect powder particles from the mound of powder which forms due to flow of powder from the hopper. At a certain point along the wiper’s circle of rotation, gas is admitted to the chamber through a port directly behind the wiper. The gas flows through the holes in the wiper, and so entrains particles. At the side of the chamber, another port allows the gas-powder mixture to exit the powder feeder, and flow through tubing to a junction with tubing from a second powder feeder (the LENS® 450 can be equipped with two powder feeders of two different types. The “small” powder feeder is particularly useful, because its smaller chamber allows for very small amounts of powder to be used, e.g. 100 g of Ni-Mn-Ga).

The mass flow rate of powder from each powder feeder is a function of the speed of rotation of the wiper (“powder feeder speed”), the volumetric gas flow rate, the flow behavior of the powder (determined by its size distribution and morphology, among other possible influences), and perhaps by other variables. The other variables may or may not include the pressure of the gas supplied to the system, and the level of powder within the powder feeder’s hopper; at the time of this writing, it is not clear how these variables affect the mass flow rate. Multiple users have reported inconsistencies in the mass flow rate after holding process parameters (those settings that do not include “other variables”) constant. The pressure of gas supplied to the system is set by a regulator external to the system, and is relatively constant with occasional need for adjustment. The volumetric flow rate of gas supplied to each of the two powder feeders must be controlled by the user, via a manual valve equipped with a rotameter. The powder feeder speed is controlled by the system to allow for programmed changes, but must be determined by the user when creating instructions for the software to execute, or otherwise must be directly input in the user interface. It is important to note that while the powder feeder speed may be varied on demand, the mass flow rate changes for a period of time before steady-state is reached.

Turning to the energy source, the laser beam starts at a laser unit (IPG Photonics, 400 W maximum power, continuous wave, near-infrared, Nd:YAG fiber laser), whose laser output

power is commanded by the LENS control software. Next, the laser beam enters the deposition head. This part (shown schematically in Figure 20) consists of a column through which the laser beam passes, a focusing lens, an opening through which the beam may pass to the chamber, and powder delivery nozzles which are located approximately at the opening. The deposition head receives the combined gas-powder mixture of two powder feeders because it is located downstream of a "y" junction in the tubing. The junction is not a valve and is not adjustable. The gas-powder mixture is separated into four streams within the deposition head, and then emerges out of four nozzles. The nozzles are fixed in position, and are directed so that the four streams of gas-powder mixture converge again at approximately the location of the melt pool (assuming that the height of the deposition head above the melt pool is of the appropriate, constant value known as "stand-off" height). The standard nozzles are declined from the horizontal plane by 45°, and an alternative assembly with a 30° declination is available. Additionally, the focusing lens is protected from condensation of deposition vapors and from other contaminants by a stream of gas which is directed away from the lens and towards the melt pool location. The volumetric flow rate of this gas is also controlled via a manual valve equipped with rotameter. Finally, the column of the deposition head is a telescoping assembly, and a stepper motor is used to change the height of the deposition head (this direction is referred to as the z-direction).

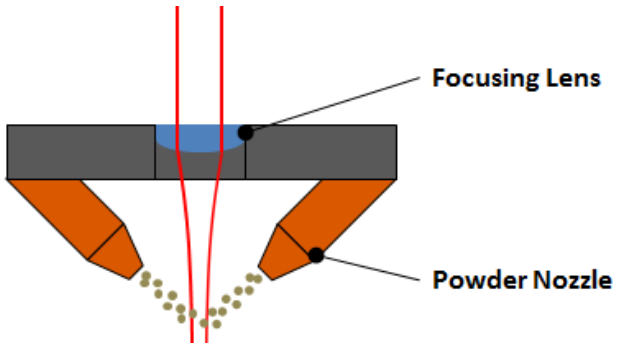

Figure 20. Schematic of the LENS 450 deposition head.

Next, the deposition stage and the chamber are described. The deposition stage consists of a tray, within which a plate with threaded, through holes is attached. The plate is attached so that a space remains between its bottom surface and the tray. This arrangement allows a substrate to be fixed to the plate, and excess powder to fall through the holes and into the tray. The tray

can later be emptied and the powder disposed of or recycled (reused for a future build). The assembly is fixed to two linear stepper motor stages, each allowing movement in either the x- or y-direction. According to the designer, the stage is capable of creating a dense steel cube of edge length of up to 100 mm or slightly more. Finally, both the deposition head and stage are enclosed in a chamber which is purged before deposition. The purge is done by flowing gas through the chamber at a rate which is higher than that used during deposition. During both purge and deposition, the chamber is to be kept at a positive pressure (higher pressure on the inside of the chamber). Oxygen content in the chamber is monitored by a Trace Oxygen Analyzer manufactured by Alpha Omega Instruments Corp., and reports values as low as 0.1 parts per million of oxygen.

Finally, the functionality of the control interface is described briefly (considering only the original system without modification). The control software of the LENS allows manual or automated control of the motion in x, y, and z, the speed of a motion, the acceleration and deceleration of a motion, the opening and closing of the laser shutter, and the speed of each powder feeder. It should be noted that the powder feeder speed cannot be changed continuously during a motion, but only before a motion or after a motion is complete. The implication of this is that a continuous “weld bead” with a compositional gradient cannot be deposited in a controlled way as of this writing. Automated motion can be input by 1) directly writing code (.dmc extension), or 2) by using additional software supplied with the system to convert a three-dimensional file (e.g., STL format) to a set of toolpath-like instructions (called a “slice” file with .sli extension) and then converting this file to code with other software supplied with the system.

2.1.3 Mechanism of deposition

Now that the mechanisms that allow deposition to occur have been described, details of the deposition process itself will be discussed. As stated before, in LENS® (and similar processes), a melt pool is created within the target area (this may be on a substrate or on a previously deposited layer) while powder is carried into the melt pool by a carrier gas. A portion of the powder stream is captured by the melt pool, melts completely, and becomes a part of the melt pool. As the deposition head moves, the melt pool moves. Thus, a cooler, solidifying “tail” of the melt pool continuously adds material to the deposit.

It should be noted that the previous discussion assumes that optimal ***process parameters*** are used. These parameters include the laser power, laser travel speed (also called traverse speed or deposition head travel speed), powder mass flow rate, and initial deposition distance above the substrate (stand-off height), in addition to the parameters which are used when determining the path to be followed by the deposition head (generally referred to as geometry). Of the latter, the layer height (referred to as "software layer height" in this thesis) is critical, as discussed next. First, however, some general relationships in processing parameters will be discussed. In general, higher laser power results in greater width in a deposited line, and also greater mass of material deposited per length of line (a study which finds this conclusion for an extremely similar system is [76]). Laser travel speed, on the other hand, has the opposite effect. For this reason, some authors [77,78] have used the concept of "***linear energy***" or "linear heat input", defining a ratio of laser power over travel speed with units of $[\text{energy}]\cdot[\text{length}]^{-1}$ (typically J/mm). However, as seen later, there is an effect where laser power and travel speed are not both influential. So, it should be understood that equal linear energies do not necessarily produce the same result.

Due to the fact that the laser used in the LENS, like many optical instruments, comes to a focus point, the laser ***spot size*** at different distances from the aperture is different. However, the power of the beam remains constant. Thus, at different distances from the aperture, the ***energy density*** is different, and this has serious implications for materials processing by the use of a laser beam as a heat source. (However, it should be noted that the severity of this effect is reduced by the presence of a "necking region", where the decrease in the spot size, with respect to increasing distance from the aperture, is reduced. This region is elongated by selection of an appropriate focusing lens with a longer focal length.) One can define a laser power density as the laser power divided by the laser cross-sectional area at the laser/material interface (known as the "spot"). Of course, the laser power density will vary with laser optics, their configuration, and the height of the deposition head above the laser/material interface (stand-off height). Furthermore, the amount of energy absorbed by the material will also be dependent on the interaction of the laser with the sample: the amount of laser energy reflected versus the amount of energy absorbed. From there, the link to solidification rates, thermal gradients and cooling rates (which govern microstructure) will pass through the laser travel velocity, the amount of material available to become part of the melt pool (powder mass flow rate), the material's thermal properties, and the heat transfer situation specific to the previously deposited geometry,

substrate and even the convective cooling caused by the center purge and powder feed gas supplies.

The ***height of the deposition head*** above the target area is critical, especially in builds involving multiple vertical layers. As the layers build on top of the previous layer, the height from the deposition head to the target area is determined by the previously deposited layer's height and by the software layer height. For a constant layer height, this results in a situation whereby the previously deposited layer's height must be equal to the software layer height. This height must not change with each subsequent layer, or else the height between the deposition head and the target area will vary as the build progresses to further layers. One might imagine that this variation would produce an oscillation in that actual layer height about an average value. However, in the author's experience, the actual layer height often diverges from the software layer height. If the layer height is increasing ("overbuilding"), the distance to the deposition head is decreasing, resulting in a larger beam spot; if the layer height is decreasing ("underbuilding"), the distance to the deposition head increases, and a smaller beam spot results. The former decreases the energy density supplied to the target area, while the latter increases it. Overbuilding often proceeds to the point of significant vaporization of the material, resulting in visible smoke rising from the build and subsequent stoppage of the build process by the operator. It should be noted that A study with an extremely similar system found that powder feed rate, number of nozzles (never varied on the specific LENS 450 used in this study), and laser travel speed had the most influence on maximum stable layer height [76], with powder feed rate as the most influential.

Now that the process parameters that are easily accessible to the operator have been discussed (at least as they pertain to the LENS 450), it should be noted that there are aspects of hardware set-up and condition of the system which affect the delivery of energy by the laser. The laser focusing lens may be moved vertically within the laser column, thus changing the distance between the aperture and the focus point. This allows the laser spot size, and so the energy density of the spot, to be varied. (If this is done without adopting a drastically different distance from deposition head to substrate, the orientation of the powder nozzles is still set for delivery of powder to the melt pool). Finally, it is important to note that the laser focusing lens does become coated with unintended substances, despite the center purge gas flow that is intended to protect the focusing lens. As the lens becomes coated with more additional material, the power

transmitted through it necessarily decreases, resulting in a decreased energy density at the laser spot.

A frequent questions concerns the exact time of melting of the powder. One may ask whether melting of powder particles occurs before or after the powder enters the melt pool. one might argue that the time of flight of the particles within the relatively small spot size (for the LENS 450, 240 μm nominal diameter at the melt pool surface, with standard settings and standard deposition head height) is negligibly brief, but this is not based on any analysis or observation. It can also be proposed that the outside of the particles will melt first, and the portion of liquid is likely to be dependent on an individual particle's size.

2.1.4 AM terminology and other processes related to LENS®

Related terms for the technological process will now be discussed. The process can be categorized under the generic term of Laser Metal Deposition (LMD, as put forth by Gu et al. [73]), and also by the more recent classification of Directed Energy Deposition (DED), which was established by ASTM committee F42. The latter is less restrictive, as it does not require a laser as an energy source. Specifically, the system used is a LENS® 450, manufactured by Optomec (Albuquerque, NM, USA). Competing, proprietary processes at the time of this writing, although covering various scales in rate and resolution of deposition, include the following: Direct Metal Deposition (DMD), fielded by DM3D Technology (formerly POM, a University of Michigan spin-off); Powder-Feed Laser Metal Deposition process, fielded by EFESTO; and Precision Additive Manufacturing (PAM), offered by Huffman. Additionally, IREPA LASER uses its CLAD® technology in-house, TRUMPF incorporates Laser Metal Deposition (LMD) in some of its products, and the Laser Consolidation (LC) process was at some time marketed by an entity known as Accufusion [79]. Additional DED processes which do not utilize powder do exist. Electron Beam Additive Manufacturing (EBAM), fielded by Sciaky, operates at much larger length scales than LENS® and utilizes an electron beam as a heat source and wire as feedstock. DED processes that are based on arc welding also exist, and most of these use wire as feedstock (but at least one does use powder). Information about other processes, and AM in general, was included in section 1.9.

2.1.5 Deposition of samples within this thesis

Three samples were deposited with identical deposition paths (geometries) but various laser power settings in order to vary the energy density. Deposition took place by moving the deposition head in a path shown by Figure 21 and with parameters listed in Table 7. The deposition path was repeated five times, and at the end of each path execution (shown by the diamond in Figure 21), the deposition head was moved away from the substrate in the z-direction by approximately 0.25 mm (that is, a software layer height of 0.25 mm was used). An approximately 51 x 51 x 6 mm plate of 99.99 % nickel was used a substrate. Prior to deposition, the plate was rinsed and wiped with acetone, followed by the same procedure using isopropyl alcohol. It is acknowledged that a layer of NiO_2 is likely to have formed on the surface after removal of the plate from its inert gas packaging, and no steps to attempt removal of such a layer were taken (and no other steps are regularly taken during manufacturing operations with LENS systems). The "small" type of powder feeder was thoroughly cleaned before use and loaded with the feedstock powder (described in section 2.2). The substrate was fixed to the deposition stage, and deposition took place after a thorough purge of the chamber with argon (which was necessarily also used as the carrier gas).

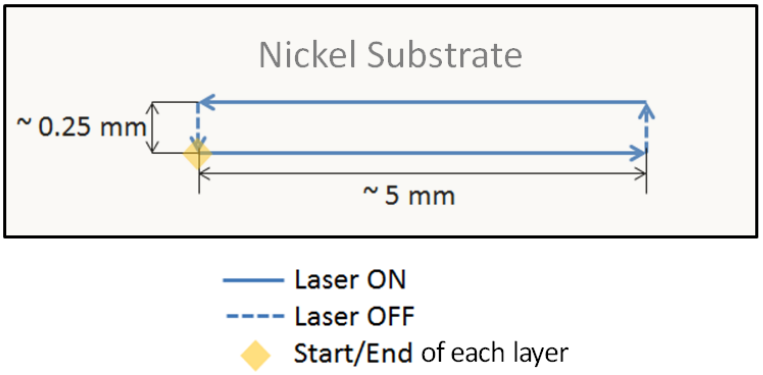

Figure 21. Deposition path used for each layer of the deposited samples. This path was not rotated or changed in any way among the layers. View normal to the substrate.

Table 7. Process parameters used for deposition of samples.

Sample	**200 W**	**250 W**	**300 W**
Nominal laser power* (W)	200	250	300
Nominal laser energy density (x 10^9 W/m^2)	(0.3 − 0.9)**	(0.4 − 1.2)**	(0.5 − 1.4)**
Nominal laser spot diameter (μm)	(520 − 900)**		
Laser travel speed (deposition head travel speed) (mm/s)	2.5		
Powder feeder speed (rotations per minute)	5		
Powder feeder gas volumetric flow rate (liters/minute)	10		
Center purge gas volumetric flow rate (liters/minute)	15		
Nominal height of deposition head above deposition surface (“stand-off” height) (mm)	9		
Acceleration and Deceleration for laser travel (deposition head travel) (counts/minute^2)	120 000		
Chamber gauge pressure (x 10^3 Pa)	1.2		
Measured oxygen content in chamber (ppm)	0.1		
Laser type	Nd:YAG, continuous wave		
Laser central wavelength	1070 nm		
*Laser power transmitted to the laser spot may have been lower due to the likely build-up contamination on the laser focusing lens. **There is considerable uncertainty in the laser spot diameter, because the laser focusing lens may have been left at a position other than its default position unbeknownst to the author. This necessarily affects the laser energy density. For both, the ranges listed are not all-inclusive, and it is possible that the true values were outside of the respective ranges given here.			

Photographs of the resulting samples, taken before removal from substrate, are shown below in Figure 22. As may be surmised from the photographs, the 200 W sample did not deposit continuously. Instead, two distinct, unconnected pieces of different size were deposited. From here on, these pieces will be referred to as the “large” and “small” piece of the 200 W sample. The masses of the samples are given in Table 8. Finally, terms used to refer to directions pertaining to the samples are defined visually in Figure 23.

Table 8. Masses of the deposited samples after removal from substrate.

Sample	200 W *	250 W	300 W
Mass (g)	0.044	0.028	0.054
*The total mass of both pieces of the 200 W sample is reported.			

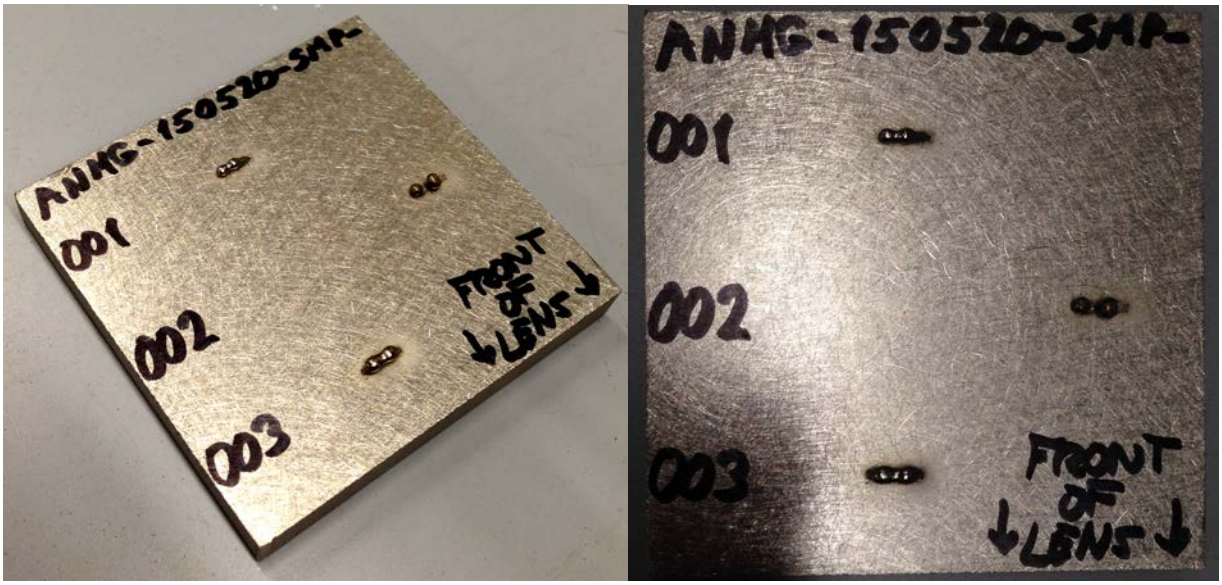

Figure 22. Deposited samples while still joined to the substrate. The 200 W sample is labeled "002", the 250 W is labeled "001" and the 300 W is labeled "003".

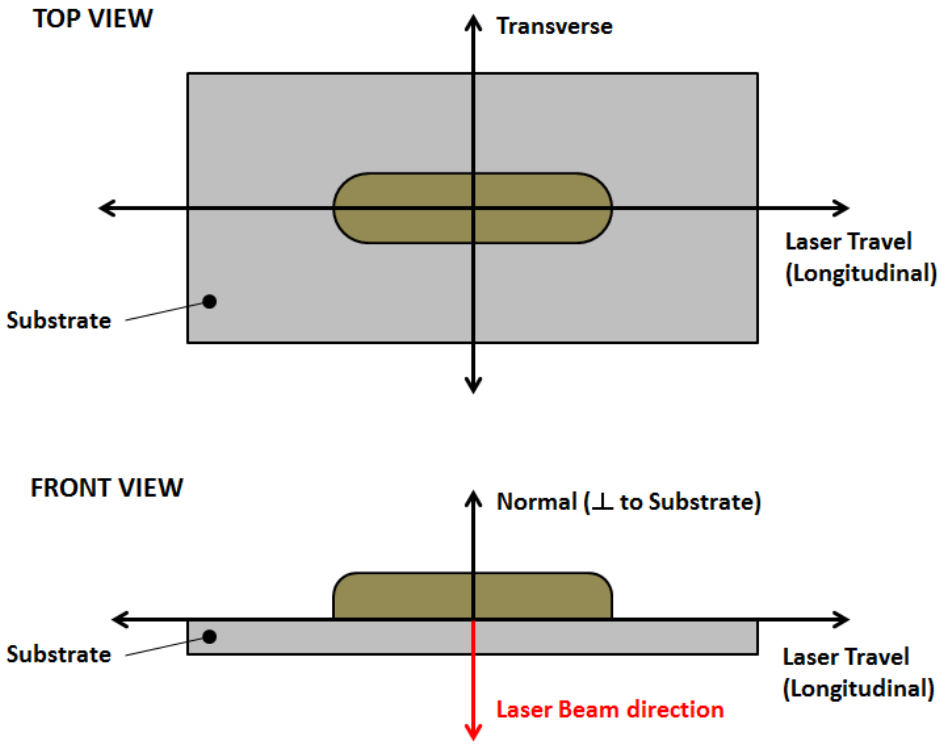

Figure 23. Schematic demonstrating sample directions and terminology used.

2.2 PREPARATION OF POWDER FEEDSTOCK

The feedstock powder was prepared by Dr. Peter Müllner's research group at Boise State University. The powder was crushed manually from an ingot, and separated into large and small size ranges. The reported composition and particle size range for each powder size are shown in Table 9. The large-size powder became the feedstock powder due to its better fit with the ~50 – 150 µm size range recommended for the LENS system by its manufacturer.

Table 9. Properties of the Ni-Mn-Ga powder, including properties of the feedstock powder.

	at%			Particle size range (μm)
	Ni	Mn	Ga	
Large powder*	51.5	26.3	22.2	54 – 106
Small powder				≤ 53
*The large powder size was used as the feedstock powder.				

For all experiments on powder except composition measurement by energy dispersive spectroscopy (EDS), the small size range powder was used. This was done in order to preserve as much of the large size powder for production of samples. Because Ni-Mn-Ga is a single-phase material, it is not expected that smaller and larger particles have differences in composition and properties. So, sieving the powder should not result in an unintended selection of some properties over others. One exception may be difference in the average amount of lattice strain, resulting from the mechanical method used to reduce the material into powder.

2.3 ANNEALING HEAT TREATMENT APPLIED TO POWDER

A sample taken from the small size range of Ni-Mn-Ga powder, described in section 2.2, was annealed to better reveal the properties of the powder without some of the residual effects of mechanical comminution (crushing). The powder was encapsulated in a quartz tube, which was evacuated and backfilled with Ar to a pressure somewhat below 1 atm before it was closed. The encapsulate powder was subjected to an annealing heat treatment at 800 °C for 10 h. After removal from the tube, the powder was noted to clump or coalesce into large, macroscopic pieces, possibly indicating sintering along the particle boundaries. These were easily crushed into powder by hand, creating powder samples for DSC experiments.

2.4 SAMPLE SECTIONING

Samples were sectioned along the laser travel (longitudinal) direction (the longest sample dimension for the 250 W and 300 W samples), producing two nominally symmetrical halves from each sample. This was done to allow mounting of one of the resulting cross-sections for microscopy. The cross-sectioned surfaces contain the laser travel direction (parallel to the longer dimension of the cross-section surface) and the normal direction (normal to the substrate surface, and now parallel to the shorter dimensions of the cross-section surface). These directions were also previously defined in Figure 23 of section 2.1.5.

The sectioning was accomplished with a WS-22B wire saw with goniometer option, marketed by Princeton Scientific Corp. (the saw is also marketed in Europe under the Unipress name). This wire saw creates cuts by passing a smooth wire in a reciprocating motion over the sample. An abrasive mixture is dripped onto the location of the cut by an automated dispenser. It is the abrasive mixture which truly creates the cut as it flows between the sample and the reciprocating wire. To aid the cut, the sample is also rocked in an oscillatory manner in the plane of the wire. Abrasive powder mixed with cutting oil and a 50 μm wire were used, resulting in minimal material loss.

2.5 VIBRATING SAMPLE MAGNETOMETRY

2.5.1 Overview

In the sense used here, a magnetometer is an instrument used to measure the magnetization of a sample of material. Perhaps the most common method used in the materials science and metallurgy field is the Vibrating Sample Magnetometer (VSM). VSM experiments can determine the magnetic properties of materials such as their hysteresis behavior (if any), and furthermore, are useful in observing phase transformations involving phases with distinctly differing magnetizations. Invariably, VSM measurements show the value of the magnetic moment (or

magnetization) as a function of another variable, including magnetic field strength[2], temperature *T*, orientation of the sample within the magnetic field, or others, given the necessary accessory equipment. Some VSM setups can also determine the direction (vector) of the sample's magnetic moment. The magnetic moment measured by the system is typically normalized by sample mass, resulting in magnetization values, which can be used to determine the magnetic field within the sample according to equation (1.3) in section 1.5. Magnetic permeability and susceptibility can also be calculated according to equations (1.2) and (1.4), respectively.

At the core of the working principle of the VSM, as implied by its name, is a controlled oscillatory motion (vibration) of the sample. This is distinct from an earlier invention which vibrated the pickup coils. The working principle is shown schematically in Figure 24. The motion of a body possessing a magnetic moment within an external magnetic field produces a change in the magnetic field lines within that field. While the average strength of the field will not be disturbed by a consistent oscillatory motion, a periodic oscillation in the magnetic field lines will result. Since it is also known that a changing magnetic field induces a changing current in an electrical conductor located within that field, an oscillatory (alternating) current will be induced in that conductor by an oscillatory motion of a body possessing a magnetic moment. VSM designs exploit this principle by placing multiple pick-up coils in the vicinity of the sample, and given a controlled motion of the sample and a known calibration constant (or multiple constants), the alternating current induced in the pick-up coils is compared to the signal used to control the motion and its amplitude then related to the magnetic moment of the oscillating sample. Some VSM designs may also incorporate a superconducting quantum interference device (SQUID) for magnetic moment measurement.

[2] VSM instruments typically report the magnetic field strength in units of tesla (T) or gauss (G). This value is the quantity $\mu_0 \cdot H$ (where the relative permeability of air is neglected) and is often measured by a probe inserted into the magnetic field. Thus, the applied field *H*, which would have units of amperes per meter (A/m) or oersted (Oe), is not reported directly. See footnote 3 of section 2.5.3 for more detail.

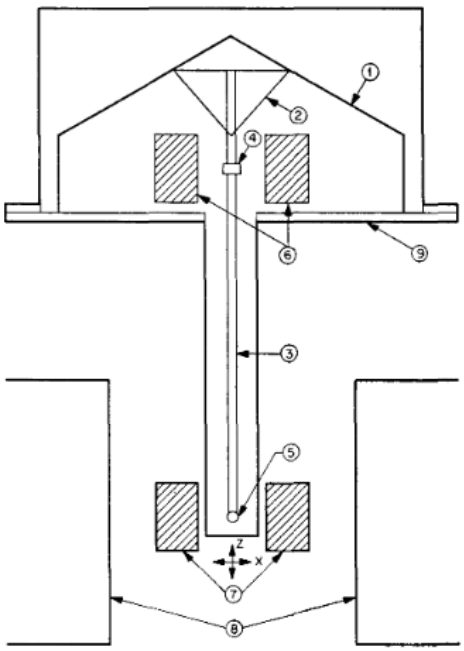

Figure 24. Simplified schematic of an early vibrating sample magnetometer (VSM). 1,2,4 and 6 are components of the drive mechanism (head drive), 3 connects the drive to the sample, the sample is located at 5, the pickup coils are shown by 7 and the electromagnet poles by 8. The metal container labeled 9 is not generally used in contemporary VSMs. Reprinted from "Versatile and sensitive vibrating-sample magnetometer" by S. Foner, Review of Scientific Instruments 30, 548 (1959), with the permission of AIP Publishing. [80]

In order to create accurate magnetization (or magnetic moment) measurements, the sample must be located in the intended center of the magnetic field. For irregularly shaped samples, the sum of the magnetic moments of the sample must be located at this point. This is either accomplished by adjusting the location of the sample within the field (known as "saddling"), or by preparing samples of pre-determined dimensions.

2.5.2 Physical Property Measurement Systems (PPMS) VSM Option

Experiments to determine magnetization as a function of temperature, resulting in *M* vs. *T* data, were conducted on a multi-purpose instrument that is known as the Physical Property Measurement System (PPMS) and manufactured by Quantum Design, Inc. The PPMS is essentially an instrumented liquid helium dewar with temperature control of the sample space.

The available temperature range is 4 – 400 K (-269 – 127 °C) (lower temperatures may be achieved with additional options). Importantly, the major feature that is integral with the PPMS are superconducting magnets which produce maximum fields of 7 to 16 T, depending on the magnets installed. Typically, the sample space is evacuated to an absolute pressure in the range of 10 – 15 torr (1.3 – 2 kPa). The PPMS functions as a VSM by installing a special VSM accessory in its sample chamber. The VSM option features sample "troughs" which hold the sample during vibration, and are shaped to accommodate a cylindrical specimen (the troughs resemble a tube with a minor angular section removed). The sample trough may only be "saddled" along their length (vertically in the system). In order to ensure centering in the horizontal plane of the magnetic field, the sample holder is intended only for cylindrical samples that are fabricated to fit directly in its inner diameter and which have homogeneous properties. Thus, the deposited samples studied within this thesis could not be centered in the PPMS VSM magnetic field. For this reason, results from these experiments are reported with a magnetization in "arbitrary units", because a proportional error has been introduced into the magnetization measurement by the sample's location within the instrument.

2.5.3 LakeShore model 7407 VSM

A LakeShore model 7407 VSM was used in this thesis to collect two types of data: 1) magnetization as a function of magnetic field strength (M vs. $\mu_0 \cdot H$ data[3], also known as hysteresis loops), which also determine the saturation magnetization of samples; 2) additional M vs. T data. This model of VSM utilizes an electromagnet with a horseshoe-shaped magnetic circuit. The physical continuity of the electromagnet is interrupted by an air gap, which allows for the placement of the sample into the magnetic field. The gap is bounded by the pole caps, which are flat surfaces which terminate the poles of the electromagnet. The poles, in turn, are geometrical features of the electromagnet which "narrow down", or decrease in cross-sectional

[3] Note that these curves are identical to M vs. H curves, except that the applied field is replaced by the magnetic field strength in the VSM air gap (into which the sample is placed). Neglecting the relative magnetic permeability of air, the magnetic field strength in the gap is practically equal to the applied field H multiplied by the magnetic permeability of free space, μ_0 (which is constant).

area, as the air gap is approached. This results in a multiplication of the magnetic flux density, resulting in greater magnetic field strength at the sample. The air gap also contains pick-up coils for magnetic moment measurement, and a magnetic field probe (gaussmeter) for closed-loop control of the magnetic field strength. A smaller air gap results in a greater magnetic field strength at the sample; however, enough room must remain for the instrumentation just mentioned and the sample holder. For this reason, the air gap is adjustable by movement of the electromagnet poles.

The sample or sample holder is connected via a sample tail to the head drive, which is an assembly which creates controlled, periodic oscillation of the sample. The sample tail can be moved by stage drives in three axes (X, Y and Z) and rotated about its axis (for orientation-dependent measurements). Finally, the pick-up coils provide the critical signal which is processed to create experimental data.

To collect M vs. T data, the model 7407 VSM was equipped with a model 74034 high-temperature oven, which can control its sample chamber temperature according to pre-programmed parameters. Unfortunately, due to limitations created by the relative location of the oven attachment points, the head drive, and the center of the magnetic field, perhaps exacerbated by the irregular shape of deposited samples, the samples could not be saddled for M vs. T experiments. For this reason, results from these experiments are reported with a magnetization in "arbitrary units", because a proportional error has been introduced into the magnetization measurement by the sample's location within the instrument.

2.5.4 PPMS VSM experiments

Where noted, the magnetic moment vs. temperature experiments which appear in the Results (section 4.1) were conducted with a PPMS with installed VSM option operated by the research group of Prof. Jeremy Levy in the Department of Physics and Astronomy. Bulk samples were attached to the inside of tubular "trough" sample holders, which resemble a tube with a minor angular section removed, and are constructed from brass and plated with gold. Adhesion of the samples to the holder was facilitated by Krazy® glue (colloquially known as "superglue"). The samples were approximately located along the length of the trough. Vertical centering was later improved after sample loading into the PPMS by an automatic centering operation performed by

the PPMS control software at a constant field of 250 mT. As mentioned, due to the shape of the samples used in this thesis, horizontal centering within the magnetic field was not achieved; However, the error introduced is significant in its effect on the recorded magnitude of the magnetic moment, and has no implication on observation of temperature-dependent phase transformations and the Curie point.

Magnetic moment versus temperature (*M* vs. *T*) experiments were conducted under a constant magnetic field of 25 mT. Samples were brought to 100 °C, then cooled in a "stabilization" mode in 1 °C steps to -50 °C, and then heated in the same manner to 373 K. The stabilization mode functions by delaying collection of a data point until the temperature of the sample space is evaluated as stable by the PPMS control algorithm, thus allowing for a significantly closer approach to thermal equilibrium between the sample and relevant temperature sensor than if a "sweep" (constant rate of change) mode had been used. For the experiments shown in this thesis, data collection was further delayed by 30 s after this criterion had been met. Changes from one temperature step to the next were conducted at a rate of 1 K/minute, and the entire experiment took place in a vacuum of 10 – 15 torr and with a vibration frequency of 40 Hz. The units of temperature in the recorded data were converted from kelvin (K) to Celsius (°C).

2.5.5 LakeSore VSM experiments

Saturation magnetization experiments were conducted with a LakeShore model 7407 VSM with a pole-to-pole air gap setting of approximately 22 mm. Deposited samples were attached to "side-mount" sample tails, where the longitudinal (laser travel direction) axis of the samples was parallel with the vertical direction, using Krazy® glue (colloquially known as "superglue"). A powder sample was poured into the sample holder designed for powder samples. This holder consists of an internally threaded cup, into which the sample is poured, and a pestle-like mating feature which threads into the cup to secure the powder in its place. This assembly, constructed of Kel-F© polymer, was then attached by a threaded connection to an appropriate "sample tail". Centering of the samples within the magnetic field was accomplished by movement of the drive head by the saddling technique, whereby the value of the magnetic moment is maximized in the "z" (vertical) direction, maximized in the "y" direction (this direction lies within the horizontal

plane and is orthogonal to the direction running between the electromagnet poles), and finally minimized in the "x" direction (the direction which runs between the electromagnet poles), thus placing the sum of the magnetic moments of the sample in the center of the magnetic field.

Saturation magnetization measurements were conducted by collecting magnetic moment versus magnetic field strength (M vs. $\mu_0 \cdot H$) data. The magnetic field was taken through a loop from zero strength to maximum positive strength, to maximum negative strength, and again to zero field. Leaving enough room for the sample and sample tail, the maximum field strength achievable was 2.37 T. Data was collected in steps of 50 mT from 0 to 1.5 T (in the interest of time), and in steps of 10 mT from 1.5 T to 2.37 T. The field was stabilized at each point. The output units of emu and gauss (G) were converted to $A \cdot m^2$ and tesla (T).

For M vs. T experiments, the LakeShore VSM software offers parameters which affect the degree to which the experiment approaches thermal equilibrium. The closer the sample temperature is to the measured temperature (taken by a thermocouple in or near the sample space in the oven), the more accurate the results will be. One way to evaluate this is to observe how parameters affect the degree of hysteresis between heating and cooling portions of an experiment: if the hysteresis is reduced, the hysteresis was caused by lack of thermal equilibrium (as opposed to a hysteresis inherent to e.g. a transformation). The parameters available include settle band and settle time. As the controller attempts to reach a specified temperature, it will overshoot its target and oscillate about it with reduced amplitude as time goes on. The settle band defines a tolerance about the specified temperature, and the settle time defines how long of a time this tolerance must be met for before a measurement is recorded. Of course, decreasing the settle band and increasing the settle time will increase the length of time needed to run the experiment. For this reason, two types of M vs. T experiments were conducted: a "quasi-continuous" experiment which explored the region from room temperature to above the Curie point, and a "quasi-settling" experiment which was limited to the Curie point. The latter achieved very little hysteresis in the Curie temperature, and so was used to obtain the results for Curie temperature from the LakeShore VSM shown in Table 15 of section 4.1. The values of the parameters for each type of experiment are shown below in Table 10.

Table 10. Parameters used for moment versus temperature (*M* vs. *T*) experiments with the LakeShore VSM.

	Parameter set	
	"quasi-continuous"	**"quasi-settling"**
Path (°C)	25 → 110 → 35	70 → 90 → 70
Increment between data points (°C)	1	0.5
Settle band (°C)	1	0.25
Settle time (minutes)	1	10

2.6 DIFFERENTIAL SCANNING CALORIMETRY

2.6.1 Overview

Differential Scanning Calorimetry (DSC) is an analytical technique suited to the observation of phase transformations and certain other thermodynamic transitions. When a sample experiences a phase transformation, the temperatures of the beginning and completion of the transformation, the direction of heat flow during the transformation, the breadth of the transformation in terms of temperature, and the overall qualitative nature of the peak can be observed. In this thesis, a transition of interest that is not a phase transformation is the Curie point.

The working principle of DSC will now be presented. Differential Scanning Calorimetry takes its name from the fact that the method compares two signals in order to provide a result. The method compares heat flow to a sample holder (sample pan), containing a sample, with heat flow to an identical sample holder (reference pan) that is left empty. This allows the system to isolate the signal which is due to the heat flow to only the sample, without the influence of the pan material or of overall changes in the heat transfer situation surrounding the pans. The pans themselves sit on pins which deliver or remove heat from the pans. Of course, the sample holders are necessary to allow exchange of samples and to prevent contamination of the sample chamber. As heat is passed to or from the pans, their temperature necessarily changes. In DSC experiments, the rate of heat flow to each is controlled so that the pans are both at the same temperature and so that a desired rate of change of their temperature (for example, 5 °C/minute),

is maintained throughout the experiment. In actuality, the sample pans are not in equilibrium and the sample pans are not instrumented with a temperature sensor; instead, it is the temperature of pins that is controlled. An example DSC result is shown in Figure 25. This plot features heat flow to the sample material along the vertical axis (ordinate), and temperature along the horizontal axis (abscissa). Note that these plots are commonly plotted so that numbers along the ordinate increase as the bottom of the page is approached; this is called “endo down” due to the fact that increasingly endothermic heat flow (heat flow to the sample) is plotted in the downward direction, and due to the convention that endothermic heat flow is a positive quantity. However, plots which are plotted in the opposite manner - that is, “endo up” - may also be encountered. Arrows indicate the direction of temperature change, and so can help determine the plotting method used in a DSC plot. Note that Figure 25 is not usual because cooling (the upper half of the curve) was conducted before heating (the lower half of the curve), but otherwise follows the common “endo down” plotting method.

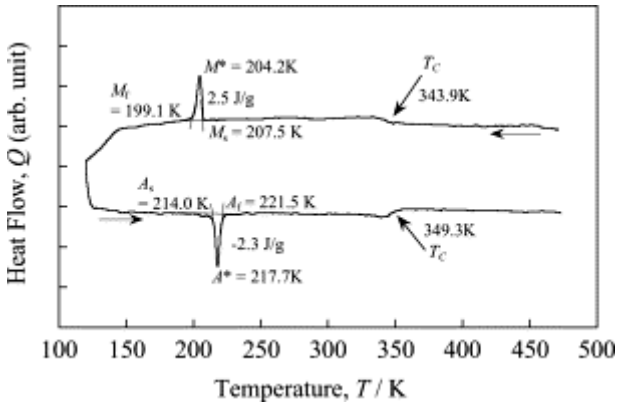

Figure 25. Example DSC curve collected with a Ni-Mn-Ga sample. Reprinted from Materials Letters, volume 57, S.K. Wu and S.T. Yang, Effect of composition on transformation temperatures of Ni–Mn–Ga shape memory alloys, pages 4291-4296, Copyright 2003, with permission from Elsevier. [81]

A few notes about effects which can reduce the fidelity of the result will now be made. First, rate of change of the temperature is an important consideration, as both rates higher or lower than is optimal may be detrimental to the quality of the result. Higher rates cause a larger difference between the controlled temperature of the pins and the temperatures of the sample and

pans, and this departure from equilibrium is a detrimental influence on the measured temperatures of points on the curve. A greater departure from thermal equilibrium leads to a greater "lag" of the sample temperature during heating and cooling, creating a higher measured temperature during heating and a lower measured temperature during cooling. It may also be possible that a greater rate of change may lead to non-negligible superheating or undercooling of the sample, thus shifting the transformation temperatures. On the other hand, lower rates reduce the amplitude of the recorded signal, because heat flow is a rate (energy per unit time). When coupled with the fact that any measurement will have a limited resolution, lower amplitude may have the effect of increasingly obscuring changes in the slope of the plotted data. This can be seen in example data shown in Figure 26. Second, the mass of the sample should be as large as practical (without causing overflow from the pan due to thermal expansion or physical and chemical changes) and the mass should be known with accuracy. A large mass provides a signal of greater amplitude, and using the same logic as for the effect of lower rates of change of temperature, allows for easier identification of changes in slope in the recorded data. Finally, the sample, pans, pins and chamber must be kept free of contamination. Contamination may result in variations in the signal, and these may or may not be distinguishable from those that are caused by the sample.

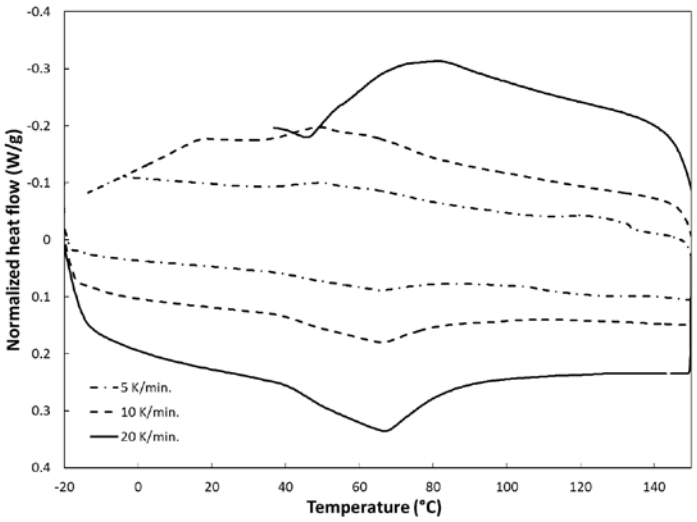

Figure 26. Example of the effect of rate of temperature change on the same sample. Conducted on the 200 W sample from this thesis.

2.6.2 DSC experiments

In this thesis, DSC experiments were conducted using a PerkinElmer Pyris 6 (for bulk samples), and also using a TA Instruments DSC Q10 (for powder samples).

The Pyris 6 DSC, as installed with cooling accessories in the Materials Characterization Lab of the Dietrich School of Art & Sciences, was able to achieve starting temperatures as low as -30 °C. The DSC may also be used up to temperatures of 400 °C and possibly higher, and is calibrated for rates of change of temperature of 5 to 10 °C per minute. While -30 °C could not be achieved during cooling portions of experiments because the controlled cooling rate could not be maintained, even with a 1 °C/minute rate, the DSC was able to reach below room temperature upon cooling. Experiments with slower rates reached lower ending temperatures. Samples were loaded into non-hermetic pans, with lids that simply lie flat on the pans (with the exception of the 200 W sample), and a continuous flow of nitrogen was maintained through the sample chamber. Due to the size of the larger piece of the two pieces of the 200 W sample, the lid could not be used for these experiments, but the other experiments were not repeated without lids. Some experiments were conducted at 5 °C/minute, and it was determined that this rate was not sufficient. So, experiments on all deposited samples were conducted at 10 and 20 °C/minute.

Experiments on powder samples in the TA Instruments DSC were conducted with lids on the sample pans and nitrogen gas purging the chamber. For as-received powder, the experiment was conducted at a rate of 10 °C/minute, while the experiment for the annealed powder was conducted at 1 °C/minute. The higher rate of 10 °C/minute is the reason why only the heating portion of the experiment was conducted for the as-received powder – since this DSC is not actively cooled, its capability to conduct cooling at high rates is limited. However, since no distinguishable features were seen after repeated experiments with the as-received powder (see Figure 32 in section 3.2), it is thought that the difference in experimental parameters between the two powders should not lead to any misleading conclusions.

2.7 OPTICAL MICROSCOPY

2.7.1 Overview

Optical microscopy allows the observation of myriad features of a material specimen, including but not limited to grain boundaries, twins, inclusions, pores, and second phase particles. By focusing light and magnifying the resulting image in a way that preserves some or all of the detail (down to the physical limit that comes from the wavelengths of visible light), the microscope can create images with resolution far beyond that of the human eye. While not all features may be visible, various lighting and imaging techniques can improve the visibility of many. When microscopy is preceded by chemical etching of the sample by an appropriate etchant, many microstructural features, including grain boundaries, dissimilar phases, or significant chemical segregation become easily visible. A commonly listed upper boundary for the magnification achievable with optical microscopy is 2000 times, or expressed another way, a lower boundary for resolution is on the order of 10^{-7} m [82]. Equipment which advertises higher magnification is available, although these values are still of the same order as the limit just cited.

2.7.2 Differential Interference Contrast (DIC)

Differential interference contrast (DIC) microscopy, also known as Nomarski contrast microscopy, is a technique in optical microscopy which increases contrast by probing a specimen with two differently polarized wavefronts simultaneously, recombining them, and then making small variations in the phase of the resulting, viewed wavefront visible as intensity variations (or even as color variations) [83]. When reflected light configurations are used to view opaque, nearly flat specimens, these variations in phase correspond to gradients present in the specimen's surface. As an example, Figure 27 shows a comparison of a brightfield image (a) to a DIC image (b). The detectable gradients typically connect surface features which differ in height by tens of nanometers to micrometers [83], and so are much smaller than gradients observable with brightfield optical microscopy. For this reason, DIC techniques can be powerful tools for observing defects which manifest themselves at the surface. In this thesis, DIC is used to observe crystallographic twins.

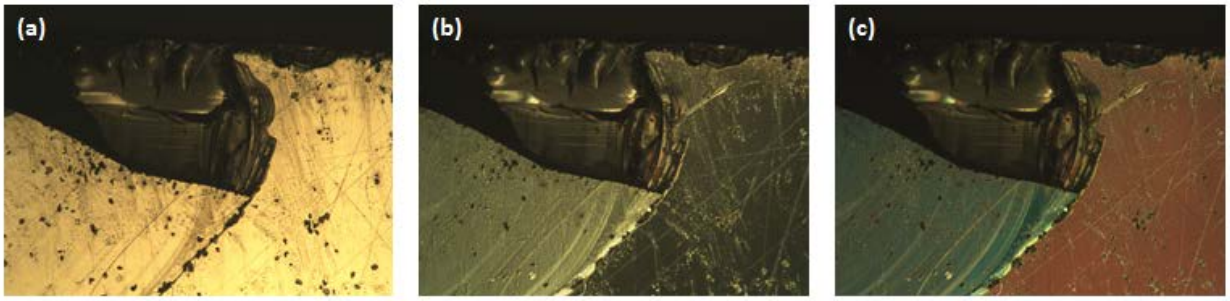

Figure 27. The same exact field of view (an edge of a notch in a piece of metal) is acquired with (a) brightfield microscopy, (b) DIC microscopy, and (c) DIC microscopy with optical staining. Note that white balancing of the camera was not done, and that this was not corrected for in order to present the differences accurately.

DIC relies on the optical properties of polarizers and birefringent crystals to divide an appropriate light source into differently polarized components [83]. An opaque, reflective surface can then create path differences between the components (producing phase differences), and recombine the components in a way that produces amplitude differences. These amplitude differences create darker or lighter areas of the image for increasing or decreasing surface gradients. The correspondence of brightness to the sign of the gradient may vary with settings, With a properly adjusted DIC setup which includes a bias (a phase difference in the differently polarized light waves which illuminate the surface), surface relief appears as if illuminated from the side by a flashlight. As a result, the direction of change in gradient can be interpreted qualitatively by observing the entire image. Thus, because the "location" of the "flashlight" can be altered by changing the setup of the DIC microscope, the correspondence of the sign of the gradient to the change in brightness is determined by the setup. So it is advisable to confirm the relationship on a case-by-case basis.

When amplitude differences are considered for a range of wavelengths, the DIC concept can be extended to amplitude differences across the spectrum of illuminating light. The resulting spectra appear as a specific subset of colors (called ***interference colors*** or Newtonian interference colors) in the image where surface gradients are present. Continuous areas of a given gradient appear in one color, and this effect is called ***optical staining*** [83]. Figure 27(c) is shows an example of optical staining. It may be realized in a DIC microscope by addition of an appropriate plate which acts on the phase of light waves to the optical path or by appropriate positioning of the birefringent crystal, depending on the DIC microscope design [83]. The optical

path in a reflected light optical microscope with DIC is shown schematically in Figure 28 (see next page) and described in detail in its caption. Specifically, a de Sénarmont design is shown because it is the type used to collect DIC images in this thesis.

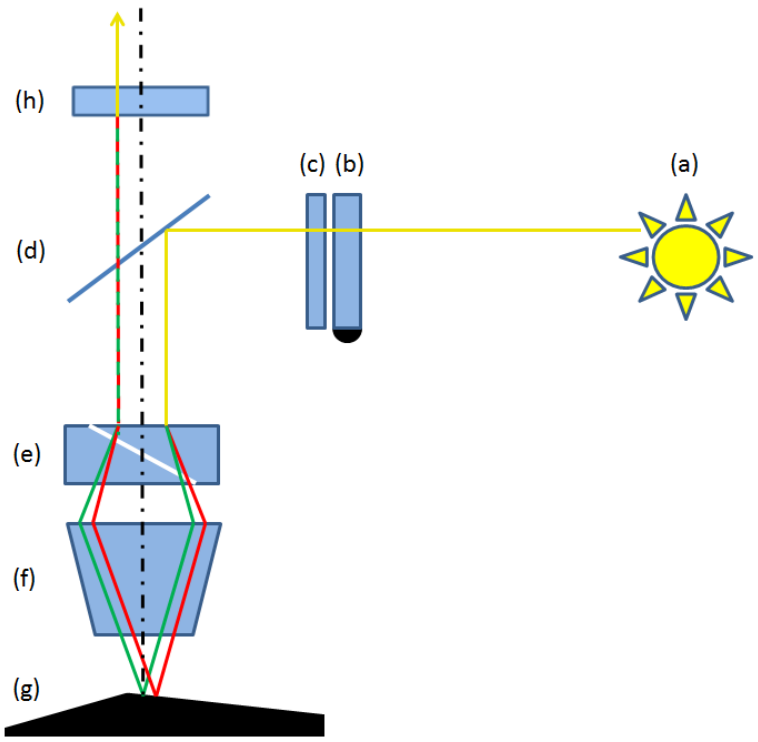

Figure 28. The optical path in a reflected light microscope with DIC in a de Sénarmont design (adapted from [83]**). A single ray of light is shown. The ray starts its journey at the filament or bulb (a), passes through the field and aperture diaphragms (not shown), and then encounters the polarizer (b). The ray emanating from the polarizer is polarized in one plane only, and this plane may be rotated by rotating the polarizer. Next, the polarized ray passes through a compensator or other phase-shifting plate (c), and is reflected downwards towards the objective by a half-mirror (d). Before the objective, the polarized ray enters the Nomarski (or modified Wollaston) prism (e), which separates the ray into two mutually, orthogonally plane polarized rays (due to its special construction from two birefringent crystals). These rays exit the prism with a special geometrical relationship, pass through the objective (f), and reflect from the specimen (g) at two very closely spaced points (the distance between the points is exaggerated in the figure). Because of the difference in height between the two points, a path difference and resultant relative phase shift is introduced to the two rays. The rays pass through the objective again and are recombined into a single ray by the prism. However, due to the phase shift between the two rays before recombination , the recombined ray exiting the prism is no longer polarized in the same manner as the single ray that originally entered the prism (for example, the recombined ray may be elliptically polarized). The recombined ray continues by transmitting through the half-mirror and encounters the analyzer (h), which is another polarizer. Because the amplitude of a ray after it passes through a polarizer is dependent on its polarization relative to the orientation of that polarizer, and the recombined ray's polarization is dependent on the phase shift produced at the specimen, the ray which passes through the analyzer will have an amplitude which corresponds to this phase shift. The ray finally passes to the eyepieces and/or camera (not shown), and intensity variations in the image will correspond to gradients in the samples surface.**

2.7.3 Optical Microscopy within this thesis

Specimens for optical microscopy and for scanning electron microscopy (section 2.8.2) were prepared in the same way; however, etching was an additional step before collecting some of the optical microscopy images. The common preparation for all samples consisted of mounting sample halves (produced by sectioning, see section 2.4) in epoxy and then grinding and polishing the samples' exposed surfaces. Mounting was conducted using epoxy, also known as "cold-mounting" − a type of mounting which consolidates without external application of heat or pressure. The specific epoxy used was Buehler EpoxyCure® 2 resin and hardener. The resulting "puck" shaped mounting is optically transparent and electrically non-conducting. As the surface of the sample was already flat and free of perceivable surface roughness after sectioning by wire saw (see section 2.4), a plane grinding step was not used, and the first and only grinding step was fine grinding with Struers 9 µm diamond suspension on a Struers MD-Plan gridning/polishing pad. Next, the samples were polished with Struers 3 µm diamond suspension on a Struers MD-Dac grinding/polishing pad, and final polishing was done with Struers OP-A™ colloidal acidic alumina solution diluted to 50% concentration with tap water on a Struers MD-Chem polishing pad. For microstructural observation, a mixture of 4 g $CuSO_4$ + 20 ml HCl + 20 ml H_2O was selected as an etchant, produced in a scaled-down quantity, and applied to the samples briefly (~15 s) by swabbing (HCl of concentration 36.5 – 38 w/w% and deionized H_2O used). The samples were then rinsed in deionized water.

Optical micrographs were collected with a Keyence VHX-600 digital microscope. The Keyence system is a modular design, with exchangeable objectives and multiple options for light paths. Each objective features a continuous zoom with lock-in settings for common magnification levels. With the available set of objectives, magnifications as low as 20 times and reportedly as high as 5000 times are available. An imaging chip mounted above the objective in use returns a digital image to the PC-based console. The console allows enhancements and the addition of measurements and scale bars to the image before it is stored in a digital file format.

2.7.4 Differential Interference Contrast (DIC) microscopy within this thesis

The DIC images within this study were collected in reflected light mode with a Nikon Optiphot optical microscope with a de Sénarmont DIC design, which was setup to achieve optical staining. Samples were prepared in the same way as for optical microscopy without etching. Multiple images were merged to form "composite" images of the entire surface of each cross-sectioned sample. After this first set of images was collected, the samples were heated[4] to above 100 °C in order to increase the visibility of certain features. These features appear during transformation from austenite to martensite in a sample that has one free surface, and was heated to austenite from martensite with this restriction already present. Variations in the surface topography (the free surface during the transformation) result. The heating temperature was selected in order to ensure complete transformation to austenite.

2.8 SCANNING ELECTRON MICROSCOPY

2.8.1 Overview

A scanning electron microscope (SEM) allows observation of features smaller than those observable through optical microscopy, with magnifications exceeding 50 000 times and resolutions approaching 10^{-9} m [82]. Images obtained by SEM also have a large depth of field: physical features appear focused for a large distance above and below the plane of the exact focus, in comparison to optical microscopy. This can be readily demonstrated by creating comparable optical and SEM images of non-planar objects or rough surfaces. In an additional, but potentially more powerful comparison with optical microscopy, SEM images collected in

[4] Initially, heating was conducted on a hot plate set to 120 °C. It was noticed that the 300 W sample, which had a higher level of mounting material between the hot plate and the sample, showed very little response. IT was surmised that the larger length of epoxy did not allow the sample to reach a sufficient temperature, and so, this sample was heated in a drying oven.

“backscatter” mode provide visual representation of areas with a difference in concentration of heavier and lighter elements. Given a material system composed of elements of sufficiently disparate atomic mass, segregation may be observed as lighter and darker areas in the backscattered image (lighter areas correspond to higher proportion of higher atomic number elements). Furthermore, these backscattered electron images may be able to reveal differences in crystallographic orientations in some cases with appropriate instrument settings, as demonstrated for twinning in section 4.5 of this thesis. Additionally, optional accessories can enable reasonably accurate, “semi-quantitative” measurements of chemical composition (energy dispersive spectroscopy – see section 2.9) or identification of phases by crystal structure or mapping of grain size, morphology and orientation (electron backscatter diffraction).

The working principle of the SEM (shown schematically in Figure 29(a)) will now be briefly described. Under vacuum, an electron source (either a thermal filament gun or field emission gun) provides a beam of electrons which is then modified and focused by a set of electromagnets (“lenses”). Another set of electromagnets then “rasters” the beam across the sample [84], meaning that the beam moves in a grid-like pattern. The area covered by the beam depends on the magnification set by the user. Within the surface of a sample, the beam’s electrons interact with those of the sample in a number of ways (as demonstrated by the graphic in Figure 29(b)). Those of importance in this discussion are the emission of secondary electrons (due to an inelastic collision) and the backscattering of electrons (beam electrons leave the sample surface due to Bragg diffraction within the surface). Each type of electrons is detected by a dedicated detector, if installed. Finally, an image is constructed from the detected electron intensities at many “rastered” points. Additionally, for imaging to work properly, a sufficient conduction path from the sample to a ground must be available. This is accomplished by connecting the sample to the grounded sample holder via conductive tape, and non-conductive samples (and even conductive samples, to improve conduction) can be prepared by coating with a conductive layer of elements such as C, Pd, or others.

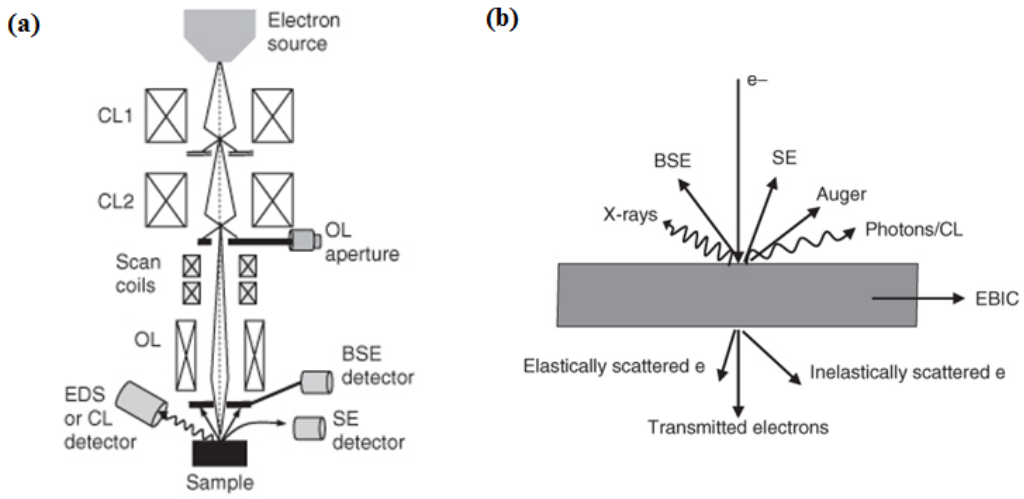

Figure 29. (a) Schematic of a scanning electron microscope. (b) Graphic demonstrating the categories of particles ("signals") created by interaction of an electron beam with a sample. Reprinted from Low Voltage Electron Microscopy: Principles and Applications by David C. Bell and Natasha Erdman with permission of John Wiley & Sons, Inc. Copyright © 2013 by John Wiley & Sons Ltd. [84]

It must be remembered that any SEM image is a virtual representation of the situation occurring inside of the SEM, and just like any representation or like an optical image, it is heavily influenced by many details, including the instrument settings used during acquisition of a specific image.

2.8.2 SEM images within this thesis

Samples were prepared for SEM with the same method as described previously in section 2.7.2, but were not subjected to etching. In order to create the necessary conduction path for electrons despite the non-conductive epoxy in which the samples were mounted, the surface of each sample was grounded using copper adhesive tape, a common practice. JEOL JSM6510 and JEOL JSM6610LV scanning electron microscopes were used at an accelerating voltage of 20 kV.

2.9 ENERGY DISPERSIVE SPECTROSCOPY

Energy dispersive spectroscopy (EDS) is a tool which allows for rapid evaluation of composition in a surface region of a material of interest and is installed as part of a scanning electron microscope. The technique is based on the inelastic scattering that occurs when electrons of an electron beam interact with electrons bound to the atoms of a solid material (Figure 29(b)). X-ray photons are produced as a result, and the energy (wavelength) of x-ray photons depends on the chemical element (atom) from which it was emitted. The relative proportion of the intensities (counts) of the x-ray photons can be used to determine the relative proportion of the elements in the material, and with some assumptions, to determine its composition. EDS uses a single wavelength-sensitive detector which captures a large portion of the useful range of wavelength, called a spectrum; Figure 30. Because the energy scattered from an element is not all exactly the same wavelength, but rather forms a peak with a measurable width when viewed on a spectrum plot, and because elements may overlap in the energy of the x-rays they scatter, peaks often overlap. Overlap limits the accuracy of compositions arrived at by analyzing the spectrum. Outside of the case of overlaps, EDS generally has an uncertainty of "+/- 2 % of the measured composition" "for a well-calibrated system" [85], and the detection limit may be 0.1 at% to 0.5 at% [85]. The spatial resolution of EDS is determined by that portion of the interaction volume of the electron beam that generates x-rays. Satisfactory spectra may be generated in some situations at reduced accelerating voltage and current, reducing the interaction volume, but this is not an order-of-magnitude improvement.

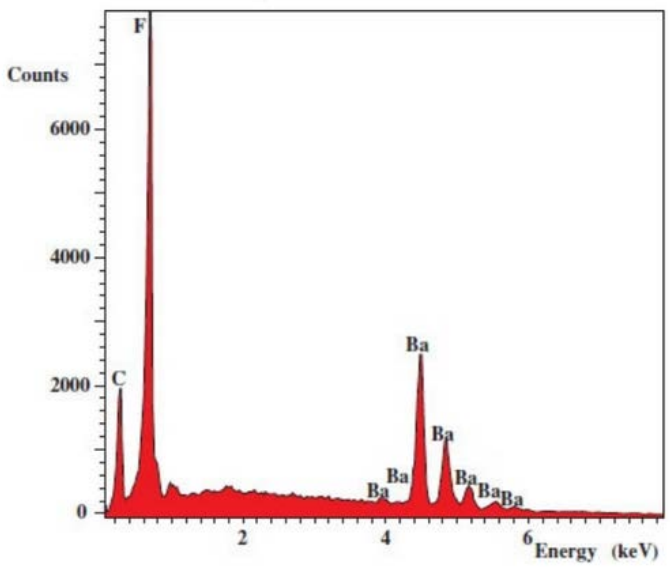

Figure 30. Example energy dispersive spectroscopy (EDS) spectrum. Reprinted from Microstructural Characterization of Materials by David Brandon and Wayne D. Kaplan with the permission of John Wiley and Sons. Copyright © 2008 by John Wiley & Sons Ltd. [85]

2.9.1 Energy Dispersive Spectroscopy in this thesis

EDS results within this thesis were obtained in a JEOL JSM6510 scanning electron microscope (SEM) equipped with an Oxford Instruments x-act detector and INCA® software. Accelerating voltage of 20 kV, magnification of 50 x were used. For deposited samples, a spot size of 60 was used. The geometry used for EDS scans is described in more detail in section 3.1 (for feedstock powder) and in section 4.2 (for deposited samples). Samples were prepared as for SEM, described in section 2.8.2.

3.0 RESULTS: POWDER FEEDSTOCK

3.1 COMPOSITION

Six EDS area scans were taken from facets of particles of the feedstock powder. Since all of the scans were equal in area, they were simply averaged. The result and its standard deviation is shown in Table 11, along with the composition reported during powder preparation.

Table 11. Measured and reported compositions of the feedstock powder.

	(at%)			standard deviation (at%)		
	Ni	Mn	Ga	Ni	Mn	Ga
Reported during powder preparation	51.5	26.3	22.2	-	-	-
Average measured EDS result for large powder	51.8	27.9	20.3	0.7	1.5	0.9

3.2 MAGNETIC PROPERTIES

Magnetization vs. magnetic field strength loops for the small size range of Ni-Mn-Ga powder, collected with the LakeShore VSM, are shown in Figure 31. By recognizing hysteresis and saturation in the curve (as described in section 1.5 and exemplified in Figure 6), one can see that the sample exhibits ferromagnetic behavior. Thus, the small size powder is ferromagnetic at room temperature. Because the small size powder was sieved away from the large size powder, it should be safe to assume that the feedstock powder (large size powder) is also ferromagnetic at room temperature (as discussed in section 2.2).

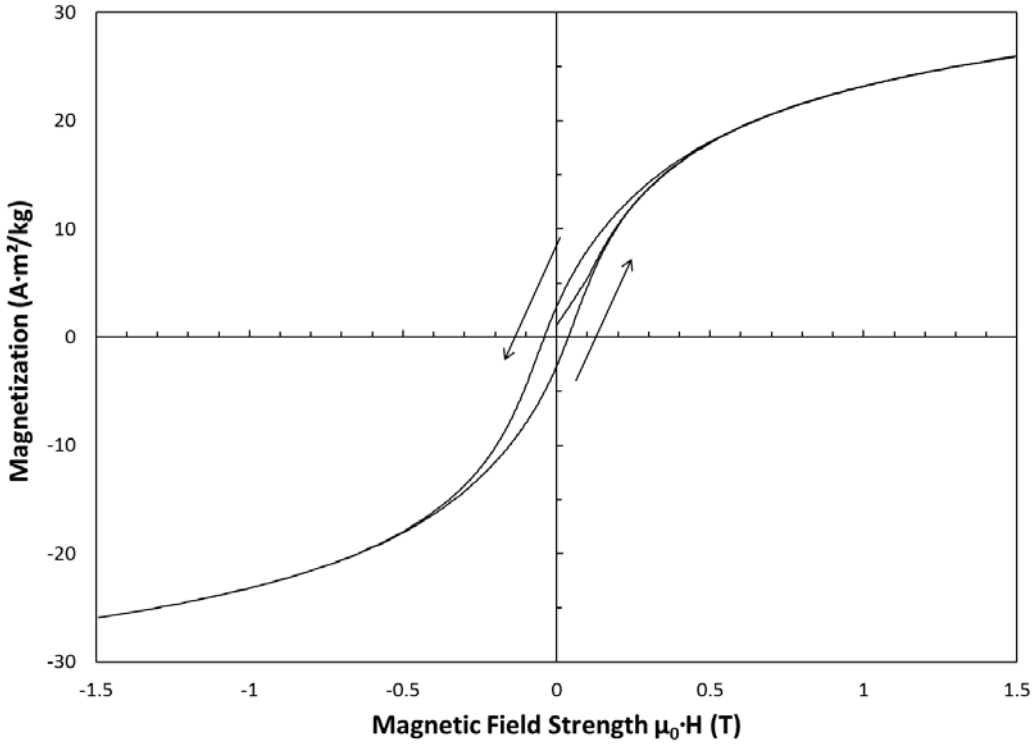

Figure 31. Magnetization versus magnetic field strength (*M* vs. $\mu_0 \cdot H$) curves for small size Ni-Mn-Ga powder in the as-received condition.

3.3 TRANSFORMATIONS

In any additive manufacturing process, the characteristics of the feedstock have a direct effect on the properties of the built material. For the present work, there is interest in determining whether the feedstock material exists in a phase necessary for the magnetic field-induced strain (MFIS) effect at room temperature. Although the presence of such a phase in the feedstock does not guarantee its presence in the deposited material, it is still prudent to investigate the feedstock.

DSC was used to attempt to observe the austenitic and martensitic transformations in the small size Ni-Mn-Ga powder. While not all martensite structures hold the possibility of MFIS, confirming that the feedstock is in the martensite phase and not in the austenite phase at room temperature eliminates an unfavorable possibility.

After observing no clear transformation in small size range powder in the as-received condition (Figure 32), it was thought that transformation may be inhibited by significant residual stresses imparted to the powder particles during preparation by mechanical comminution manual crushing). In order to relieve these stresses, a sample of the powder was subjected to a heat treatment of 800 °C for 10 h (see section 2.3). Upon conducting the same DSC experiment on the annealed sample, peaks which correspond to phase transformations were observed upon both heating and cooling (Figure 32), and the associated transformation temperatures were measured graphically (as indicated in the figure) and are given in

Table 12. Again, it is thought safe to assume that the transformation properties of the small size range powder are sufficiently similar to that of the actual feedstock powder (large size range).

Table 12. Transformation temperatures extracted from DSC experiment with annealed small-size powder (Figure 32). Values include: austenite start, peak and finish (A_s, A_{peak}, A_f); Curie temperature on heating (T_C, heating) and on cooling (T_C, cooling); and martensite, peak, and finish (M_s, M_{peak}, M_f).

	A_s	A_{peak}	A_f	T_C (heating)	T_C (cooling)	M_s	M_{peak}	M_f
T (°C)	47	58	66	88	87	55	47	41

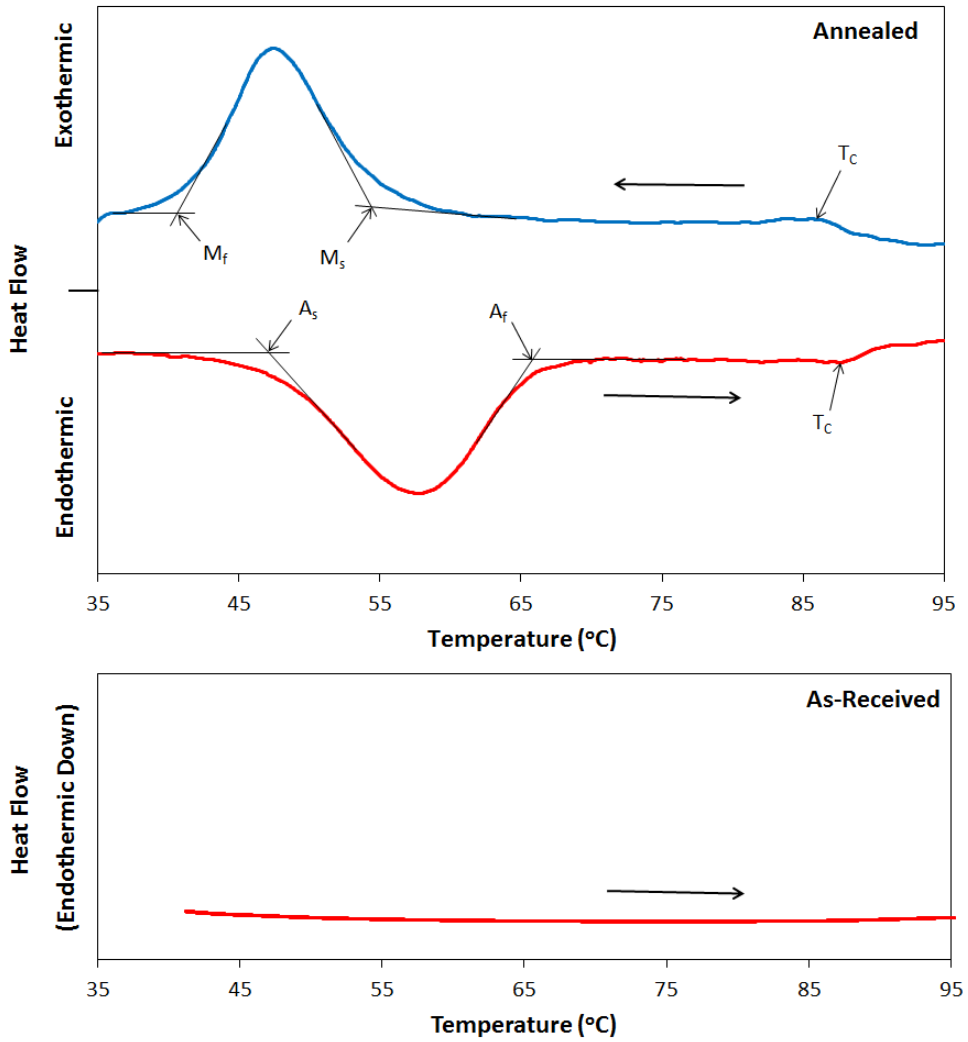

Figure 32. DSC experiment on small-size powder sieved during production of powder feedstock, in as-received condition and after annealing in vacuum for 10 h at 800 °C. Red curves were collected on heating and blue curves on cooling. Arrows indicate direction of temperature change. Rates of 1 (annealed) and 10 °C/min (as-received) were used.

4.0 RESULTS: DEPOSITED SAMPLES

4.1 SAMPLE MORPHOLOGY

The surface of all samples is made irregular by the presence of powder particles which did not melt or melted partially and adhered to the surface of the bulk deposit, as seen in Figure 33. The overall shapes of the 200 W and 250 W samples are irregular and do not match what is expected from the deposition path. The shapes of these samples seem to be influenced by anomalies occurring during deposition. In particular, the asymmetry of these samples along the scanning direction is notable and is discussed further in section 5.1. A further observation is the presence of orange-brown spots on all samples.

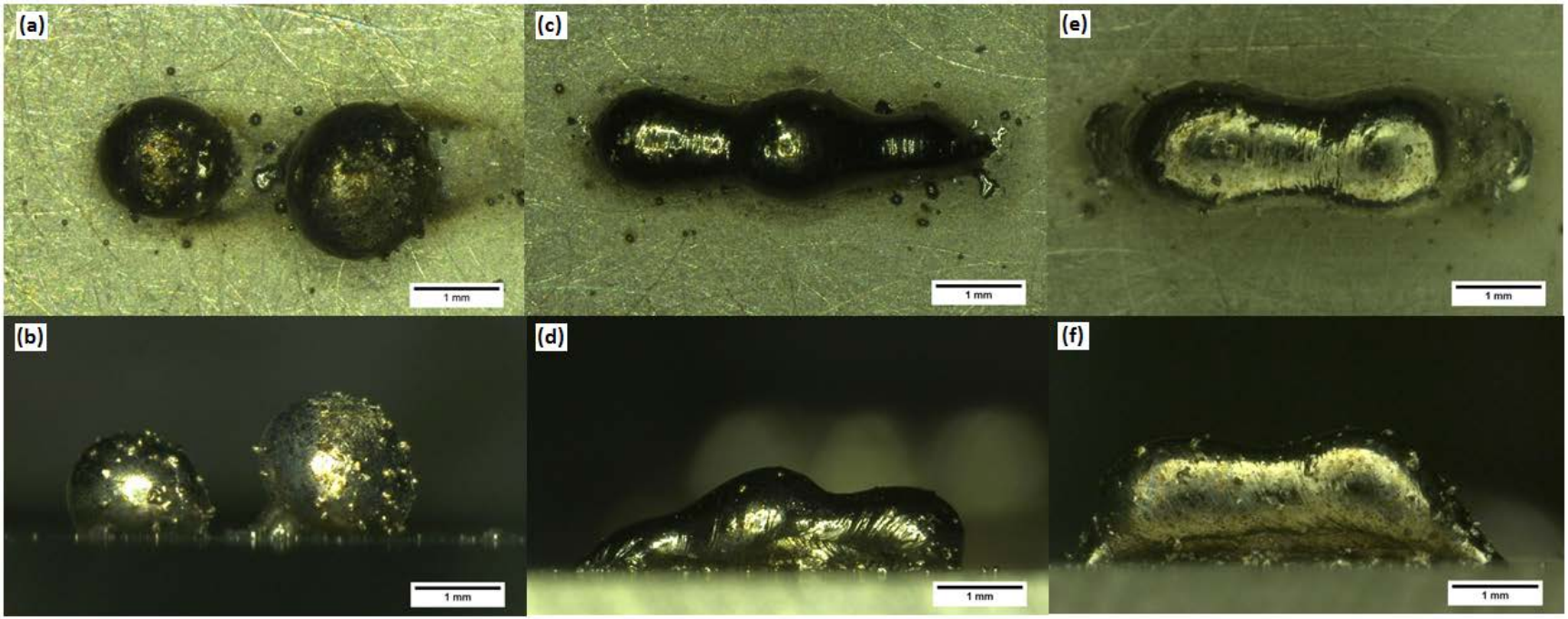

Figure 33. Views of samples in as-deposited condition. Top row contains views normal to the substrate while bottom row consists of views along the substrate. 200 W sample: (a) and (b), 250 W sample: (c) and (d), 300 W sample: (e) and (f).

4.2 COMPOSITION

To determine composition to a first degree of accuracy, EDS area scans across the sample surface were conducted. Since area scans use a rectangular area, multiple areas were used to incrementally cover the entirety of each cross-section surface. Due to the irregular shape of the samples, areas with different sizes had to be used. In order to represent the data accurately, the results for the area scans (which are inherently an average measured composition of one area) were averaged with weighting corresponding to the magnitude of each area. The resulting average compositions for each cross-section surface are shown in Table 13. It is seen that the average measured compositions deviate by at most 2.2 at% from the composition of the feedstock powder reported during preparation and at most 1.2 at% from the measured powder composition (both are shown in Table 13). For Ni alone, the deposited sample compositions are at most 1.5 at% higher than reported and 1.1 at% higher than measured; for Mn, at most 0.8 at% higher and 1.1 at% lower; for Ga, 2.2 at% lower and 0.2 at% lower, respectively. All samples show the same sign of difference (higher or lower) as just given, with the exception that one sample shows a negligible (<0.1 at%) difference in Ga compared to measured. As a group, the samples deviate from each other in measured composition by no more than 0.3 at% across all three elements.

Furthermore, to investigate variation in composition as a function of position on a cross-section, EDS line scans were conducted. These scans revealed no measureable variation in composition across different directions on the cross-section. Point scans conducted in sequential lines across a cross-section yielded variations in measured composition, but not in a systematic way, leading to the conclusion that the scatter in values was a result of either uncertainty associated with EDS or a result of compositional gradients on length scales too small to reliably evaluate with EDS. Thus, more sensitive tools may need to be used.

Table 13. Averaged energy dispersive spectroscopy (EDS) results obtained from each deposited sample and comparison to powder composition.

	at%			standard deviation (at%)		
	Ni	Mn	Ga	Ni	Mn	Ga
200 W*	52.9	27.1	20.0	-	-	-
250 W	53.0	26.8	20.2	0.14	0.12	0.04
300 W	52.7	27.0	20.3	0.12	0.04	0.17
Powder, measured	51.8	27.9	20.3	0.71	1.49	0.90
Powder, reported	51.5	26.3	22.2	-	-	-
*Large piece of 200 W sample. Only one area scan was used, so standard deviations are not available.						

4.3 MAGNETIC PROPERTIES

The saturation magnetization of the deposited samples was explored in order to enable comparison to literature. Magnetization vs. magnetic field strength ("M vs. $\mu_0 \cdot H$") loops were measured using vibrating sample magnetometry, resulting in the hysteresis loops seen in Figure 34. The experiment proceeded from zero field strength to +2.37 T, to –2.37 T, and finally to +2.37 T again, resulting in a hysteresis loop. In the figures, the first segment from zero to +2.38 T is omitted for clarity. It is seen that all three samples are near saturation at fields greater than 2 T in magnitude. Above fields of 2.1 T in magnitude, the slope of the curve becomes constant − or at least changes in the slope are smaller than the average changes in the slope created by small-scale variation in the magnetic moment values. This holds true for all three samples shown until a magnitude of 2.3 T is reached (with the exception of the 200 W sample at negative fields), at which point the slope begins to change again, under the criterion mentioned. In other words, the increase in moment for fields of magnitude greater than 2.1 T but less than 2.3 T is approximately linear.

Figure 35 shows a view of this dataset near zero magnetic field, better showing the hysteresis of the magnetization. Values which quantify this ferromagnetic hysteresis are given in

Table 14. Furthermore, some notable changes in slope are clear in the narrower view. These changes are discussed later in section 5.2.3.

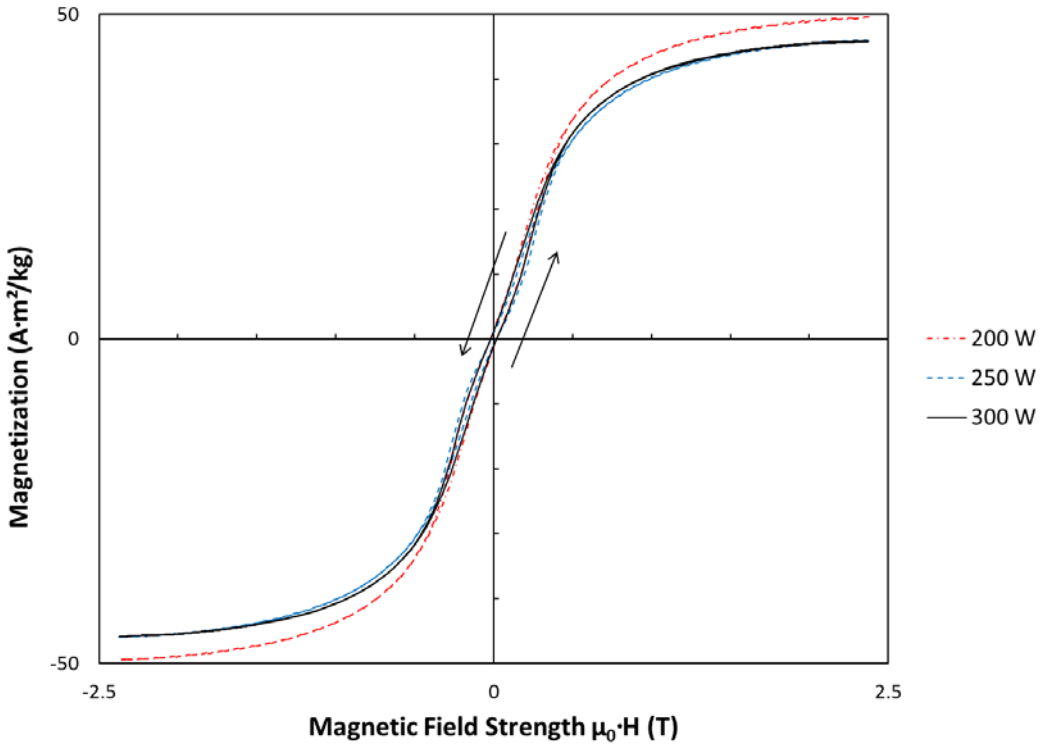

Figure 34. Saturation magnetization experiments on deposited samples by VSM at room temperature. Arrows indicate direction of experiment for curve nearest to arrow (for each sample). No shape factor (demagnetization factor) was applied.

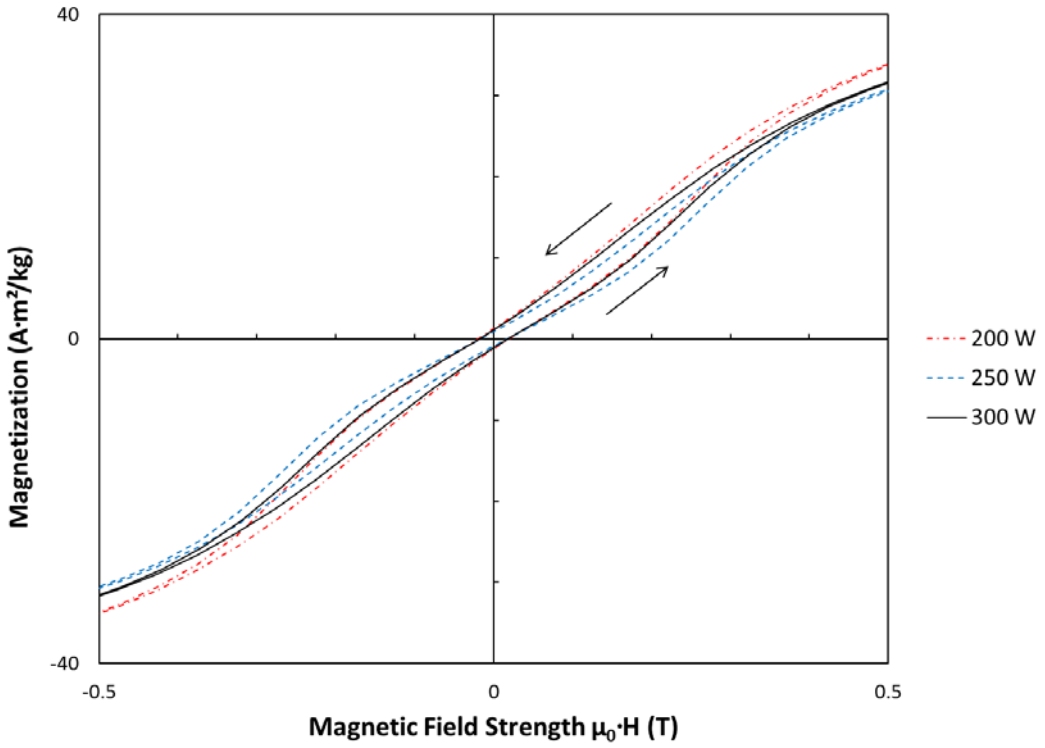

Figure 35. Close-up of data shown in Figure 34.

Table 14. Ferromagnetic properties determined from *M* vs. $\mu_0 \cdot H$ data.

	Sample		
	200 W	250 W	300 W
Saturation magnetization M_{sat}* (A·m^2/kg)	48.6	45.5	45.5
Remanent magnetization M_{sat} (A·m^2/kg)	1.3	0.9	1.2
Coercive field $\mu_0 H_c$ (T)	0.020	0.017	0.019
*Values obtained from the -2.38 T to +2.38 T segment of the M-H loop, by linear interpolation between data points for magnetization at 2.1 T			

4.4 TRANSFORMATIONS

The temperature-dependent transformation behavior of the samples was investigated with Differential Scanning Calorimetry (DSC) and Vibrating Sample Magnetometry (VSM). Both methods show that the samples, in their as-deposited condition, transform between the martensitic and austenitic phases over a broad range of temperature.

While both methods qualitatively indicate the broadness of the transformations, a quantitative measurement of a portion of the breadth has only been produced with VSM. This can be explained by the fact that DSC intrinsically relies on a transient effect (heat transfer resulting from a lack of thermal equilibrium between the pin and the sample), and so produces very broad, indistinct peaks for the case of a broad transformation; on the other hand, VSM results show the magnetization of the sample at a given temperature, and so do not rely on heat transfer as a measurement. Furthermore, during VSM measurements, each data point can be recorded at thermal equilibrium (given enough time to carry out the experiment). However, VSM is limited by the Curie point of the sample. Thus, the completion of the transformation is only measureable if it occurs at a temperature below the sample's Curie point. The samples in this thesis are of such composition that their Curie points indeed inhibit observation of the completion of the austenitic transformation (or, conversely, the onset of the martensitic transformation). To understand how the VSM results are interpreted, the following is considered. In magnetic moment vs. temperature measurements of Ni-Mn-Ga at a small and constant applied field, the austenite phase is indicated by a clearly higher magnetic moment. The higher magnetic moment is a result of the lesser degree of magnetic anisotropy in the austenite, compared to the magnetic anisotropy of the martensite. In a single crystal, the likelihood of orienting the crystal with its easy axis parallel to the magnetic field, and so potentially producing higher magnetic moment than austenite, is unlikely (unless intentional). This is compounded by the fact that the martensite generally exists as multiple twin variants, thereby reducing the volume which is oriented favorably (and the small field cannot cause growth of favorably oriented twins). In a polycrystal, even with some degree of preferred orientation, the measured magnetic moment of austenite is still further favored. Thus, the presence of austenite or martensite at temperatures surrounding the transformation range produces a step-like curve, as seen in [12].

For each of the three samples, the detectable breadth of the transformation is more than 50 K, as seen in Figure 36. Since the visibility of the transformation ends at each sample's Curie temperature, the values listed are only a minimum bound on the full breadth of the samples' transformations.

All magnetization vs. temperature curves shown below are calculated from original data by dividing the measured magnetic moment by the sample mass, in order to arrive at a magnetization with respect to mass. This step is preceded by converting from moment in the cgs unit (emu) to values in the SI unit ($A \cdot m^2$).

Magnetization vs. temperature curves, calculated from data obtained by the PPMS VSM (see section 2.5.2 for a description of the PPMS VSM), are shown in Figure 36. By reaching temperatures as low as -50 °C, this data set allows observation of the completion of the martensitic transformation. To enable comparison to data obtained by the LakeShore VSM with oven (shown next), the same data used to create Figure 36 is plotted again in Figure 37 with the more limited temperature range of the LakeShore VSM with oven (which cannot reach below room temperature).

Data obtained by the LakeShore VSM with oven (see section 2.5.3 for a description of this system), with use of "quasi-continuous" experimental parameters (see Section 2.5.5 for experiment details), are shown in Figure 38. Curves calculated from data obtained by the same system, but with use of "quasi-settling" experimental parameters, are shown in Figure 39. Due to the significant increase in experimental time with these parameters, only a limited temperature range of approximately 70 − 85 °C is investigated. This data is best suited for determination of the Curie point T_c of the deposited samples.

DSC data is presented in Figure 40 – Figure 42. Figure 40 shows data collected at a temperature rate of change of 10 °C/minute, while Figure 41 shows data collected at a temperature rate of change of 20 °C/minute. The greater rate displays the transformation behavior of the sample more prominently; however, temperature points extracted from this data will be further from the true values due to thermal "lag" or possibly due to greater superheating or undercooling. Because inconsistent deposition behavior resulted in two separate pieces of the 200 W sample, an opportunity to easily compare the transformation behavior of two points along the laser travel direction was potentially created (without additional sectioning of the sample).

Each piece of the two pieces of the 200 W sample (referred to as the small and large piece) were loaded into the DSC apparatus separately, and the resulting data is plotted in Figure 42.

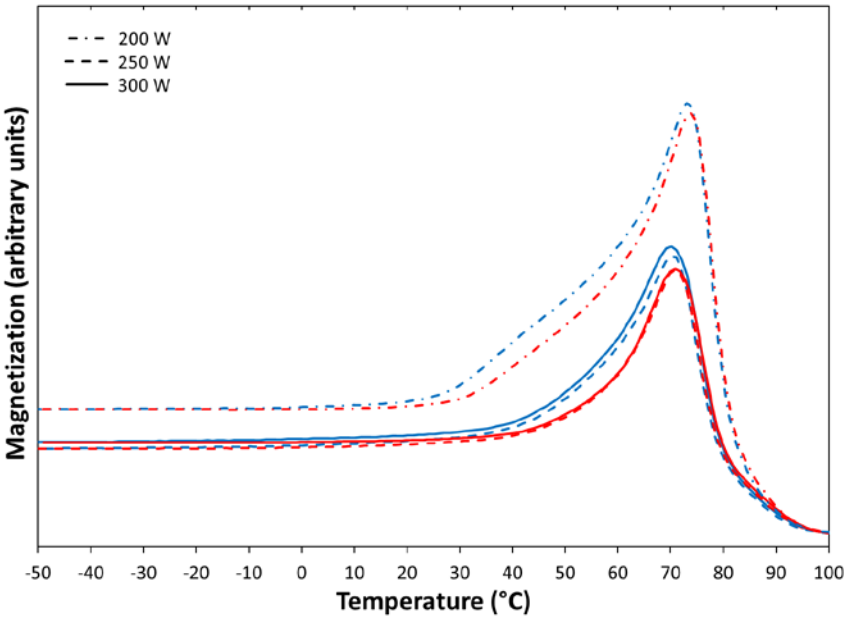

Figure 36. Magnetization vs. temperature curves obtained by use of the PPMS VSM in the range -50 °C to 100 °C. Heating curves are shown in red and cooling curves are shown in blue.

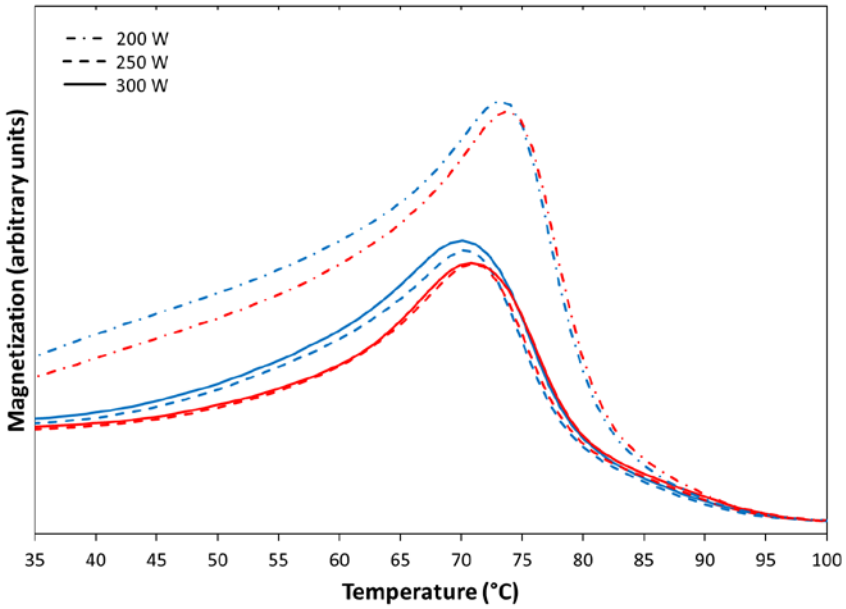

Figure 37. Plot of PPMS VSM data shown in Figure 36, limited to the range of 35 °C to 100 °C. The smaller plotted range is intended to ease comparison to the VSM results obtained by use of the LakeShore VSM, shown in Figure 38.

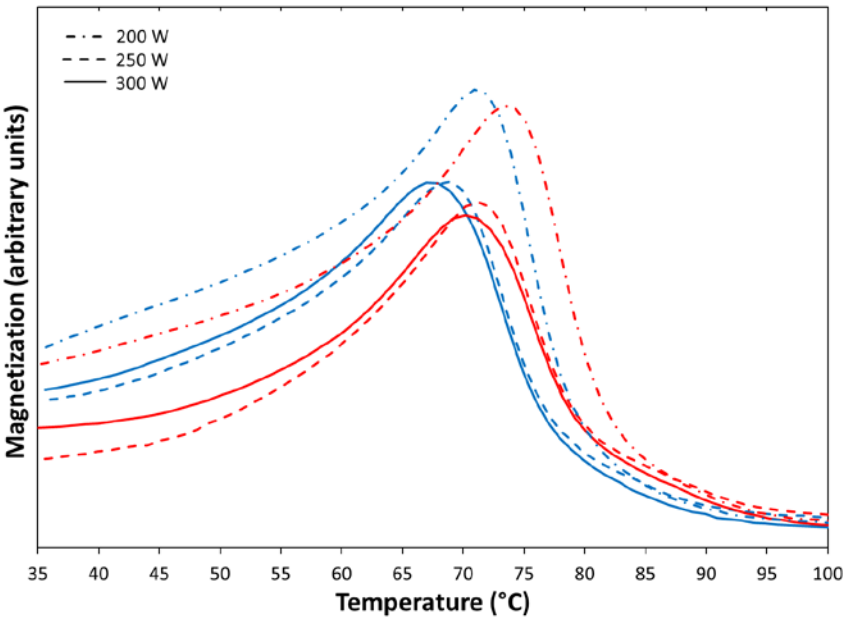

Figure 38. Magnetization vs. temperature curves obtained by use of the LakeShore VSM with "quasi-continuous" parameters. Heating curves are shown in red and cooling curves are shown in blue.

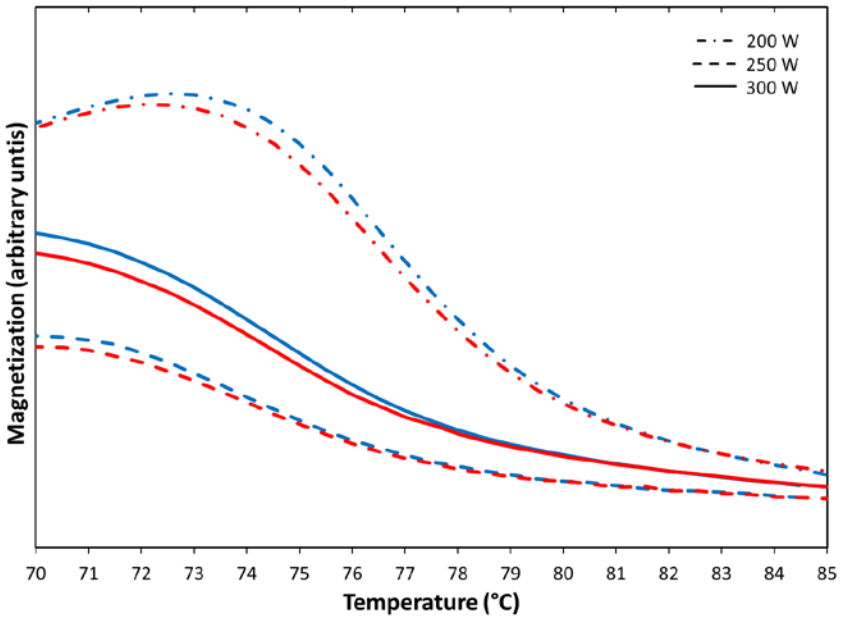

Figure 39. Magnetization vs. temperature curves obtained by use of the LakeShore VSM with "quasi-settling" parameters. Heating curves are shown in red and cooling curves are shown in blue.

Table 15. Curie temperatures and austenite start temperatures obtained from the data displayed in Figure 36 and Figure 39.

	Sample		
	200 W	250 W	300 W
Approximate austenite start from PPMS VSM data (K)	17	22-27	27
Curie temperature[1] from PPMS VSM data upon heating (K)	83	82	83
Curie temperature[1] from PPMS VSM data upon cooling (K)	82	81	82
Curie temperature[1] from LakeShore VSM data upon heating, "quasi-settling" experimental parameters[2] (K)	80	78	78
Curie temperature[1] from LakeShore VSM data upon cooling, "quasi-settling" experimental parameters[2] (K)	80	78	78

[1]Values obtained from extrapolation of approximately linear segments of magnetic moment vs. temperature curves in transition to paramagnetic region.
[2]See section 2.5.5

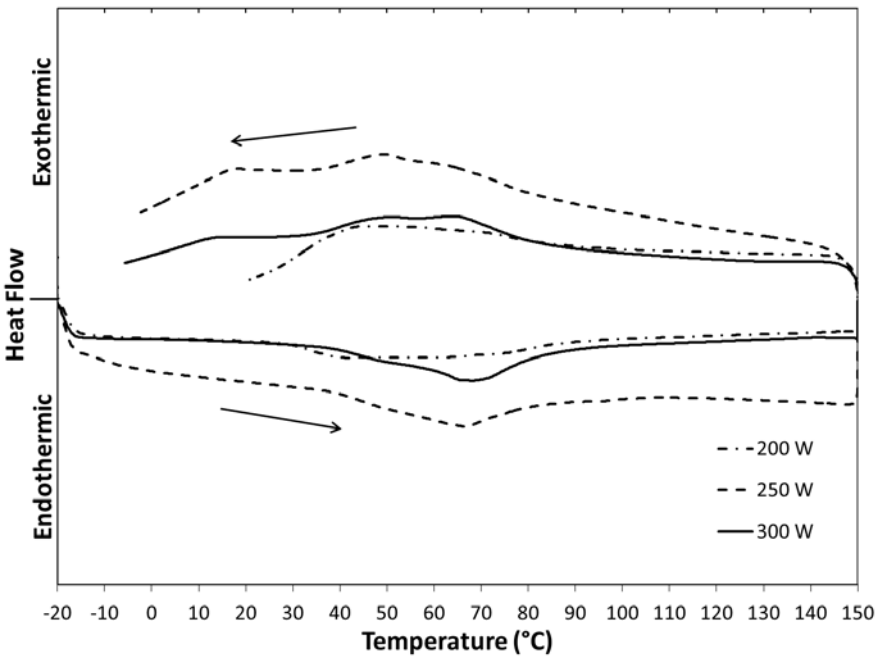

Figure 40. DSC experiments at temperature rate of change of 10 °C/minute, with heat flow to the sample ("endothermic") shown downwards. Arrows indicate direction of temperature change.

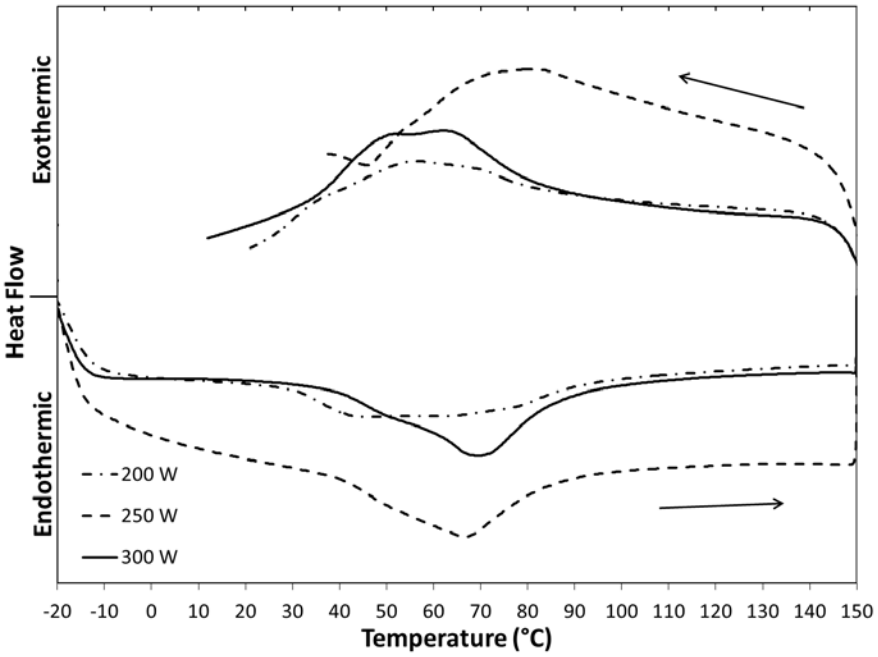

Figure 41. DSC experiments at temperature rate of change of 20 °C/minute, with heat flow to the sample ("endothermic") shown downwards. Arrows indicate direction of temperature change.

Table 16. Selected temperatures observed in DSC data on heating for feedstock powder (Figure 32 of section 3.3) and the deposited samples (at a rate of 20 °C/min, Figure 41). Points include the austenite start (A_s), austenite peak (A_{peak}) and austenite finish (A_f) temperatures, and Curie temperature (T_C). Only measureable points are given.

	Powder, annealed	200 W	250 W	300 W
A_s, °C	47	308	40[c]	27
A_{peak}, °C	58	-[a]	67	70
A_f, °C	66	93	88	89
T_c, °C	87–88	-[b]	-[b]	-[b]

a: No peak visible.
b: Curie temperature not visible in DSC data from deposited samples.
c: Curve continues with a significant slope from the beginning temperature of the DSC heating run, before changing slope. Location of change used as value.

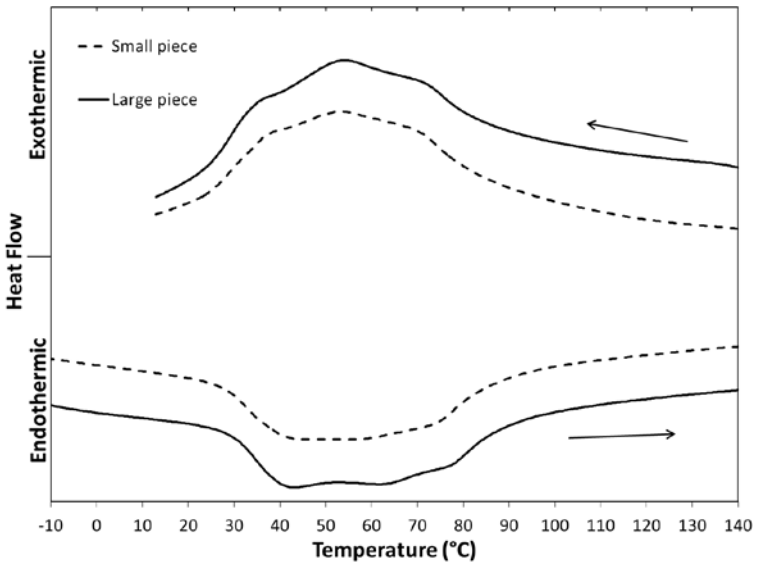

Figure 42. DSC experiments on the two pieces of the 200 W sample at temperature rate of change of 20 °C/minute, with heat flow to the sample ("endothermic") shown downwards. Arrows indicate direction of temperature change.

4.5 MICROSTRUCTURE

This section presents observation of the microstructure of the deposited samples. Thus, this section's results consist solely of microscopy. For clarity, note that the directions of the deposition process are displayed in Figure 43. These directions are the same in all micrographs of cross-section surfaces within this thesis.

The general appearance of the cross-sections is illustrated in Figure 44, showing an optical micrograph of the polished cross-section of the 300 W sample. The left micrograph features large voids, but other features are barely visible. On the other hand, the micrograph on the right (taken slightly out of focus) shows features which are not visible when the surface of the sample is in focus. These features become much more evident in later figures with the use of differential interference contrast (DIC). The fact that focusing on a different plane brings the features out, and that a surface gradient-sensitive method such as DIC does so as well, shows that they are topographical in nature. Note that both micrographs were taken after heating the sample to the vicinity of 100 °C.

Figure 45 − Figure 47 show the 200 W, 250 W and 300 W samples under DIC with optical staining. The samples are imaged in the as-polished condition and after heating to the vicinity of 100 °C.

Figure 48 shows cross-sections of the 200 W, 250 W, and 300 W samples after etching. A higher magnification view of the 200 W sample (Figure 49) reveals dendritic structures in the top-most layer of the sample and clearly shows the boundary between it and the underlying layer. This feature is seen in all three samples.

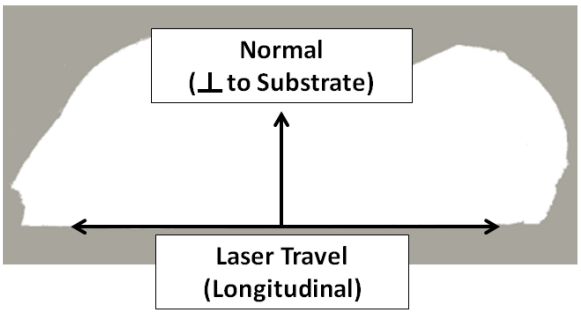

Figure 43. Directions on micrographs of deposited sample cross-sections.

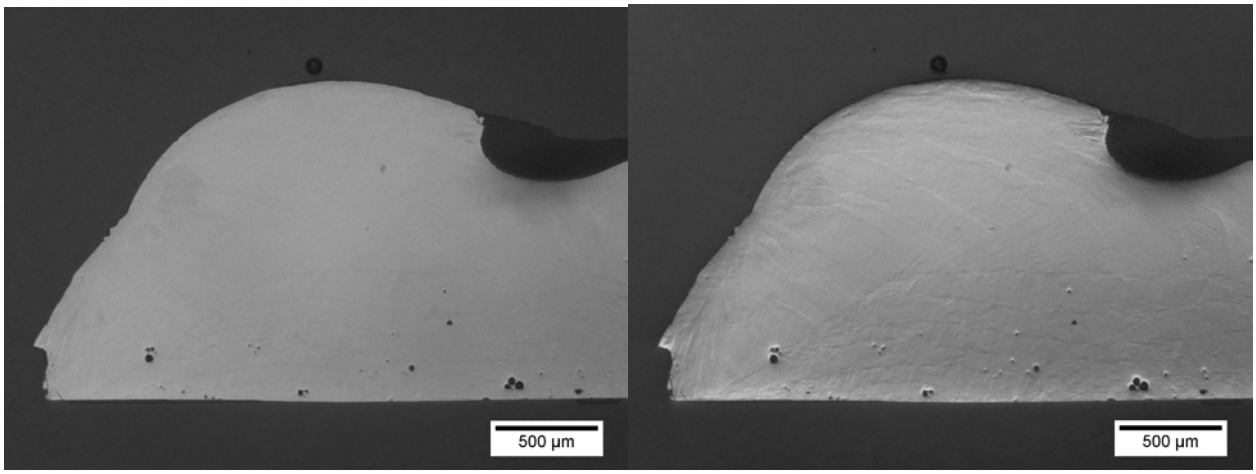

Figure 44. Optical micrograph of polished cross-section of 300 W sample, acquired while in focus (left) and out of focus (right). Both were taken after heating the sample above room temperature and cooling.

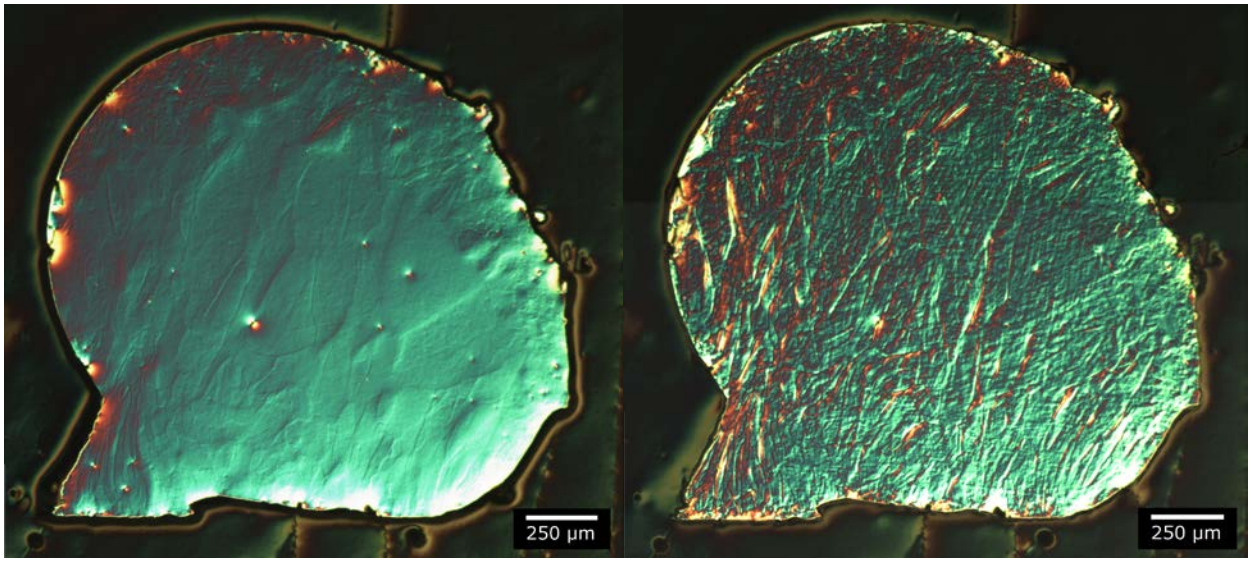

Figure 45. Composite image of differential interference contrast (DIC) optical micrographs of the 200 W sample in the as-polished condition (left) and after heating above room temperature (right).

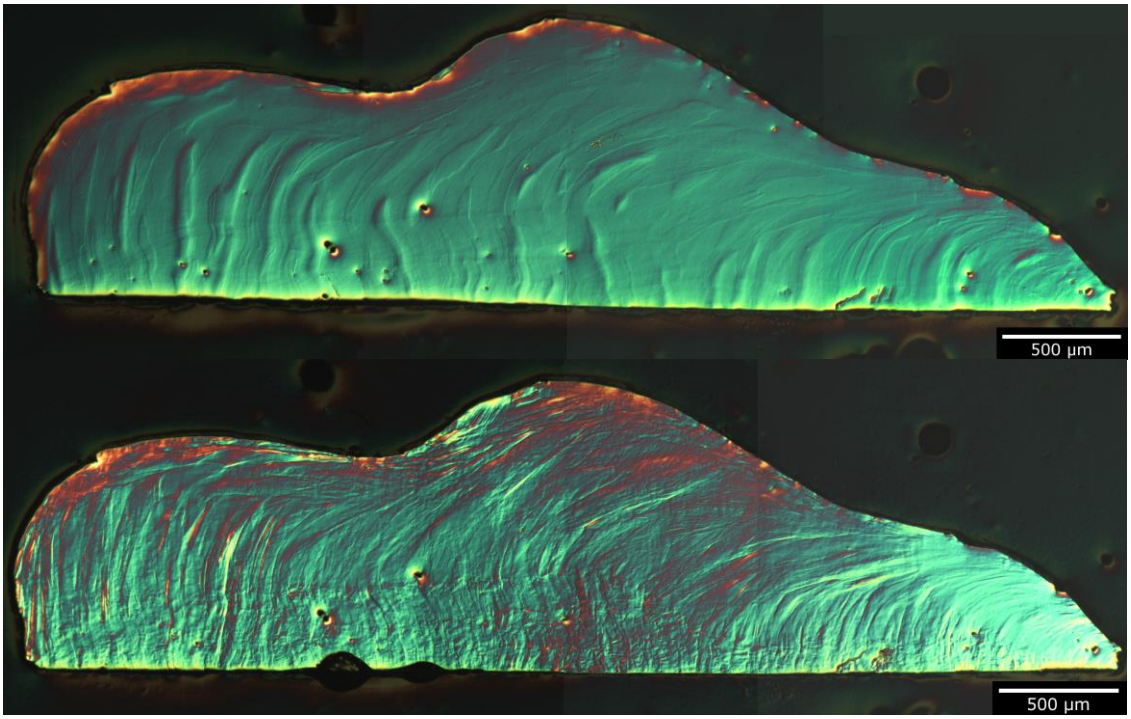

Figure 46. Composite image of differential interference contrast (DIC) optical micrographs of the 250 W sample in the as-polished condition (top) and after heating above room temperature (bottom).

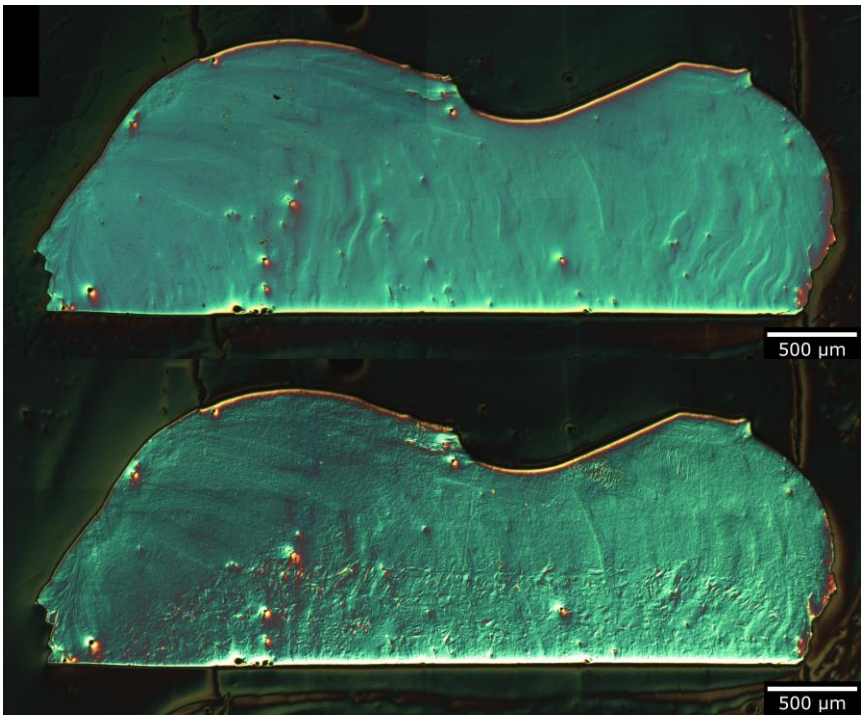

Figure 47. Composite image of differential interference contrast (DIC) optical micrographs of the 300 W sample in the as-polished condition (top) and after heating above room temperature (bottom).

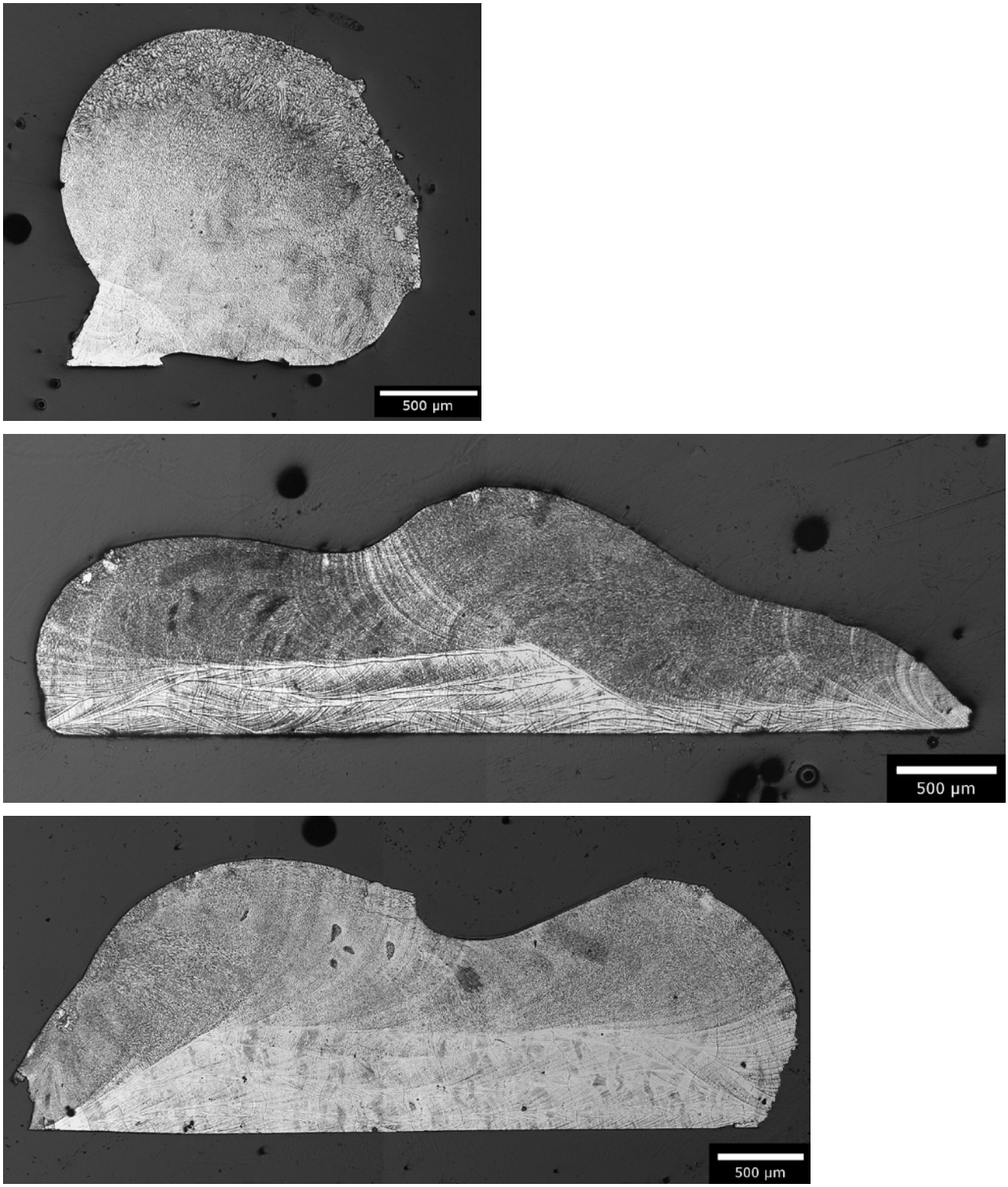

Figure 48. Optical micrographs of 200 W (top), 250 W (middle) and 300 W (bottom) samples after etching.

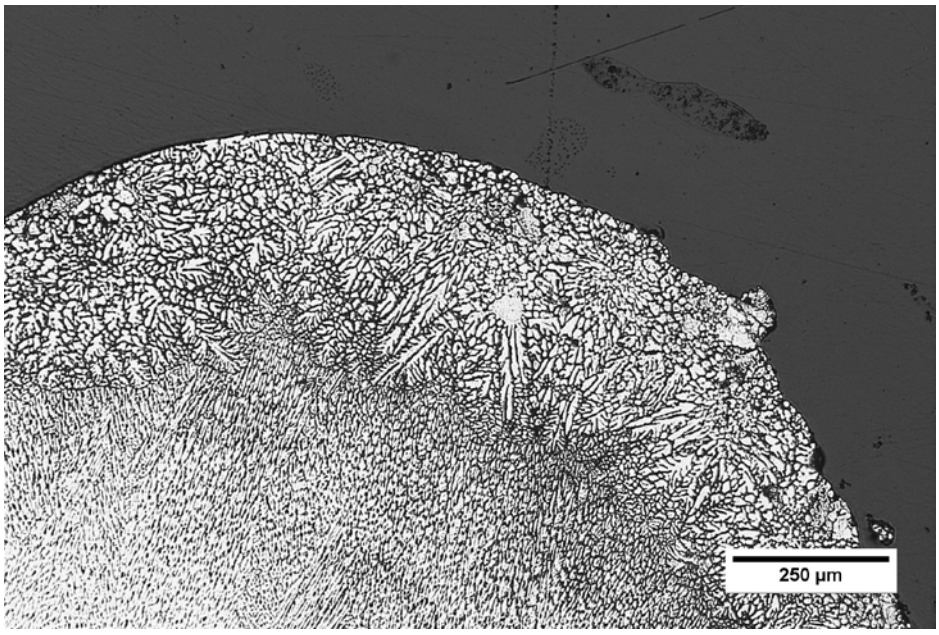

Figure 49. Optical micrograph of 200 W sample after etching, revealing the difference between the top layer of the sample and the underlying layer.

The remainder of this section will focus on twinning, which was not observed directly in the preceding micrographs. Figure 50 and Figure 51 show successively higher magnification backscattered electron (BSE) images of the polished cross-section of the 300 W sample. With increasing magnification (Figure 51), it becomes clear that the darker region which spans the first image diagonally is an area of fine, contrasting bands. The parallel bands are almost certainly twins. The sparser, wider bands which cross these parallel bands at various angles are remnants of scratches from previous grinding or polishing steps. A pair of large, irregularly-shaped features, seen in the bottom-right corner of Figure 50, are clearly voids. Similarly, the circular (or approximately circular), black features are thought to be pores. This last statement is supported by the observation that these regions show concavity when imaged with backscattered electron topography mode. It is interesting to note that these apparent pores are less regular in shape in larger sizes, but more circular in smaller sizes.

Figure 50. Backscattered electron image of the 300 W sample displaying contrast in regions, as well as in parallel bands within the darker regions. Two large pores are visible in the bottom-right corner.

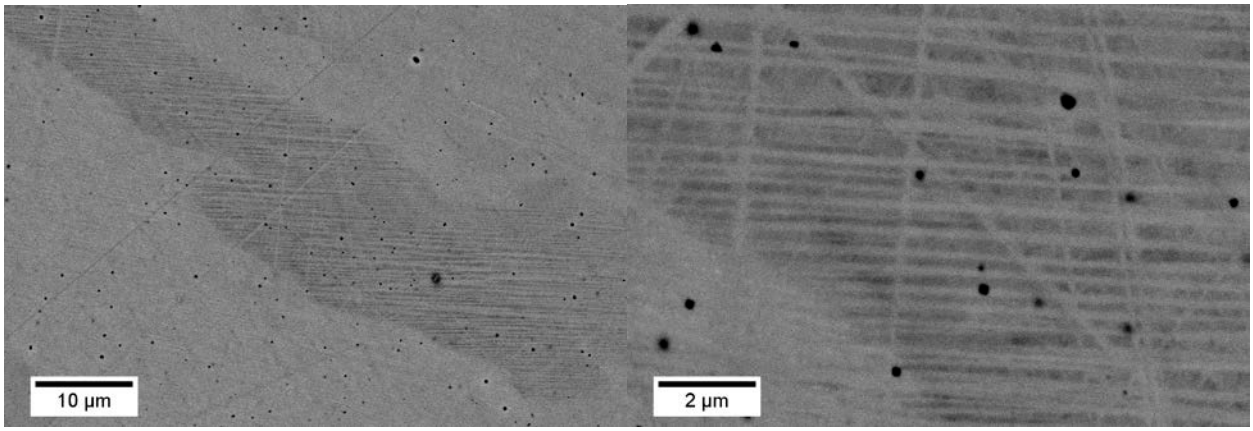

Figure 51. Backscattered electron image of the 300 W at higher magnification (left) and highest magnification (right). Bands are seen to be twins and small-scale porosity and scratches become easily discernable.

After heating, the mounted and polished cross-section of the 300 W sample displayed what appears to be surface topography indicative of twinning. These regions did not disappear on cooling to room temperature, and were further investigated by differential interference contrast (DIC) microscopy. Figure 52 − Figure 54 show successively higher magnifications of an area of

interest on the 300 W sample cross-section. In these images, areas of parallel lines appear, and again indicate that these regions may be twinned in such an orientation as to be visible. Notably, as seen in the progression of magnifications, twins seem to be crossing a layer boundary. Finally, bright circular and near-circular shapes which surround dark areas are almost certainly the edges of pores.

Additionally, taking a close look at the small spots visible in the highest-magnification DIC micrograph, many appear in the topographical relief of reflected-light DIC to have convex surfaces. This would contradict the earlier electron microscopy result which indicated that these features are pores (with concave surfaces). However, these features have diameters of less than 0.5 μm (Figure 54) - similar to or smaller than the wavelengths of visible light. Perhaps this may cause a change in their appearance under DIC.

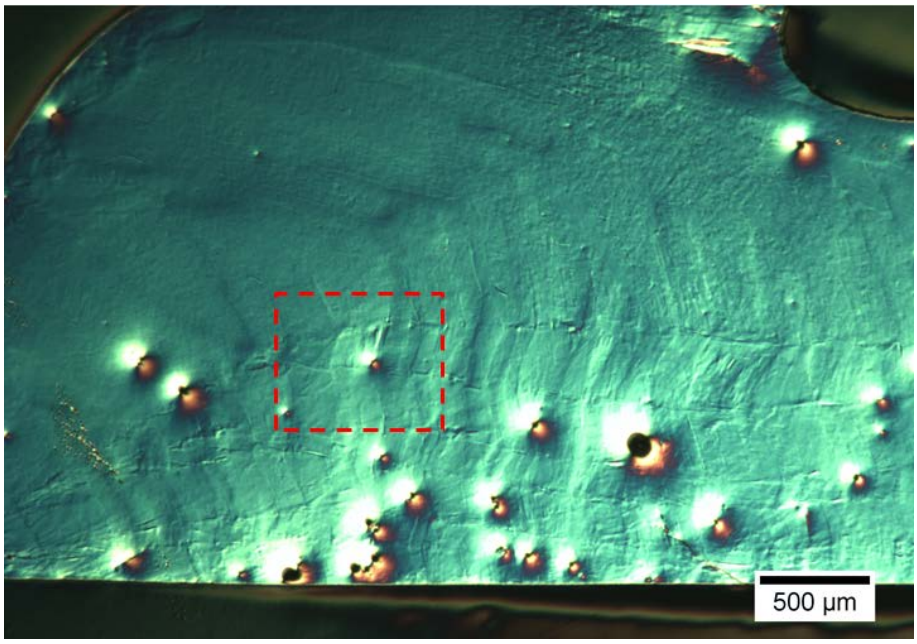

Figure 52. Differential interference contrast (DIC) optical micrograph of the 300 W sample. Boundaries between layers can be seen. The approximate area of the following figure is shown with the red dashed line.

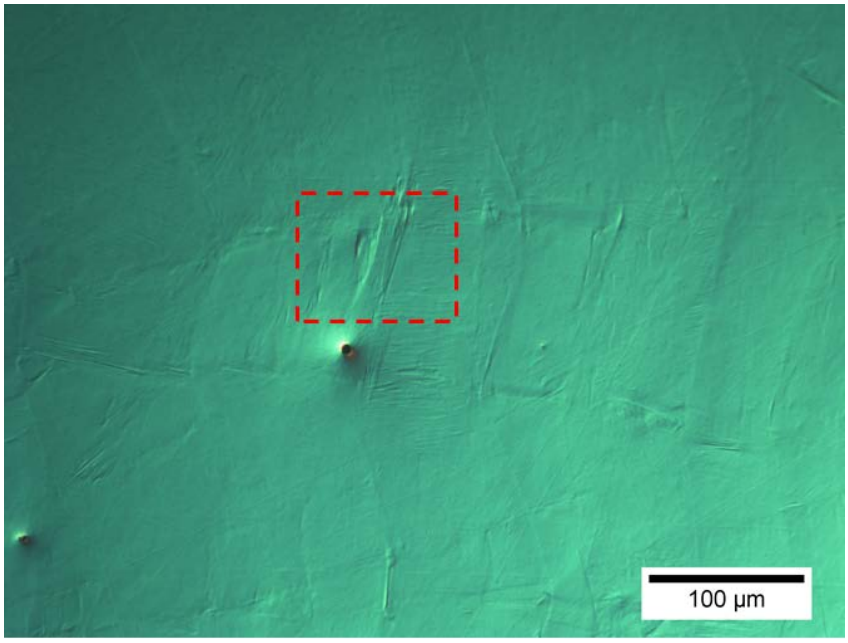

Figure 53. Differential interference contrast (DIC) optical micrograph of the 300 W sample. Boundaries between layers can be seen. The approximate area of the following figure is shown with the red dashed line. Parallel lines are indicative of twins.

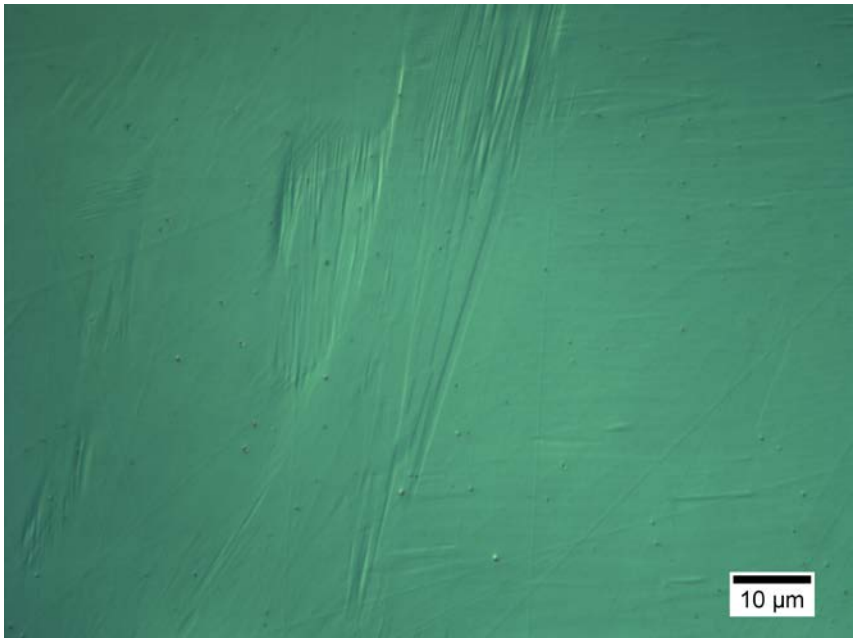

Figure 54. Differential interference contrast (DIC) optical micrograph of the 300 W sample at a layer boundary. Parallel lines are indicative of twins, and seem to extend across the boundary.

5.0 DISCUSSION

5.1 SAMPLE MORPHOLOGY

As seen in macroscopic images (Figure 33), the deposited samples are dense, have a significant surface relief and highly irregular shape. While density and visually noticeable surface roughness are typical of material produced by LENS, the irregularity in shape is not – in both the author's own experience with other materials in the LENS process, and in comparison to literature [87]. The variation in shape occurs both along the laser travel direction and among samples.

Along the laser travel direction, single lines (also known as beads) should be symmetrical about their midpoints to a first approximation. The start and end points of the line will generally be enlarged due to the necessary acceleration and deceleration of the laser travel (stage movement). When the laser (stage) is traveling at less than full speed, buildup of material is greater with respect to the length of travel. The result is a shape which may be likened to a double-ended cotton swab (or perhaps to a dumbbell). At sufficient distances away from its endpoints, a deposited line should show no major variation in shape, possessing a constant cross-section. Furthermore, the features at the lines ends should be approximately the same in shape. Noticeably, the deposited samples in this study show variation outside of what was just described. While the 300 W sample exhibits a decidedly pronounced dumbbell shape[5] which should be expected in such short laser travel lengths, the others show unpredictable changes in cross section along the laser travel direction. The 250 W sample appears to have a dumbbell shape, but it then extends into a segment with decreasing cross-sectional until the very end of the

[5] Note that the rounded checkmark-like shape which abruptly appears at the top edge of the cross section (visible in Figure 44, Figure 47 and the bottom image in Figure 48) is a result of accidental contact of the sample with a spinning abrasive saw blade during cutting of the substrate into more manageable pieces. Because it was not present immediately after the sample was produced, this absence of material is not visible in Figure 33(e) and (f).

sample. During building of the 200 W sample, the deposition process broke down completely for large portions of the laser path. Interrupted deposition resulted in two approximately spherical pieces[6], with either no deposition between the pieces or the deposition of only individual powder particles between the pieces. In a similarity to the highest points of the 250 W sample, the large pieces did not appear at the start and end points of the laser path – rather, at least one of them was produced during the main portion of the path, as evidenced by comparing the spacing between them (Figure 33(a) and (b)) with the programmed path (Figure 21). The explanation for this lies almost certainly with the powder morphology. Unlike the powders used during the author's previous experience, which are often spherical, the powder used was noticeably angular and irregular in both shape and size. Powders of this nature are known to the manufacturer of the LENS system to perform poorly in the powder feeding mechanism (described in section 2.1.2), and are not recommended for use by the manufacturer. While sub-optimal process parameters may have played a role, poor feeding likely caused large fluctuations in the mass flowrate of powder out of the deposition head and led to inconsistent deposition. This inconsistency would have resulted in increases, decreases or even absences in the mass deposited per length during building of at least two of the samples.

Although there were many issues with deposition, there was also a trend which was more in line with experience with the LENS process. Putting the inconsistency in deposition aside, the general relationship that increased laser power results in increased deposited mass (and so volume) per length of line holds true. This can be seen in photographs and optical micrographs, as the overall sample height increases from the 250 W to the 300 W sample. Although the height of the large piece of the 200 W sample is greater than the highest point on the 250 W sample, the 200 W sample is smaller overall, allowing the proposed trend to maintain some validity. This indicates a correlation of greater deposition rate (deposited mass per unit time) with greater laser power.

Another note should be made about wetting behavior of the molten deposit on the substrate. The 200 W sample showed a minimized contact area with the substrate, as seen in Figure 33(b), where the cross-sectional size of the sample increases with increasing height and so

[6] It is noted that data was often collected solely from the larger of the two pieces, except where explicitly noted in the results.

leads to a ball-like shape. Although it is possible for subsequent layers to deposit more material and so create a slight overhang to a small extent, it should be questioned whether the 200 W sample contained multiple deposition layers. First, no distinct deposition layer boundaries are visible on the outside of the sample or within the cross-section DIC micrographs (Figure 45, although the DIC images are not a focus of this section). However, micrographs of the etched cross-section of the sample (Figure 48 and Figure 49) show the effect of remelting and/or reheating on the dendritic structures. Perhaps the first deposition layer overbuilt due to a peak in the powder mass flow rate, and subsequent layers were carried out without a significant addition of material due to a prolonged interruption of powder flow, and so only remelting and/or reheating of the sample occurred. Ultimately, the deposition situation is difficult to reconstruct without some sort of process monitoring data. Returning to wetting, if the ball-like shape is a result of poor wetting between the Ni-Mn-Ga melt and the Ni substrate, one would expect to find evidence of poor wetting in the other two samples as well. Indeed the samples (Figure 33) do have a smaller contact area with the substrate than their largest cross-section (where the sectioning plane is parallel to the substrate), but they do not have as pronounced of a ball-like shape as the 200 W sample does. The surface energies of the melt and substrate and resulting wetting behavior may of interest in future work.

Additionally, the orange-brown spots seen on the samples are possibly indicative of an oxide forming on the samples. However, the spotted pattern adds additional complexity to that suggestion, because an additional argument is needed to explain why the oxide is not present over continuous areas of the sample.

5.2 MAGNETIC PROPERTIES

5.2.1 Overview

Magnetization experiments reveal that the deposited samples show ferromagnetic behavior with the concomitant saturation, in addition to some inflection points in the curves that are not found in “textbook” examples of data collected from ferromagnetic materials such as pure iron or pure

nickel. Also, the samples' saturation field is very high compared to other results for Ni-Mn-Ga. All of these points, along with Curie temperatures, are discussed in the following sub-sections.

5.2.2 Saturation magnetization behavior

From the magnetization versus magnetic field strength (M vs. $\mu_0 \cdot H$) data seen in Figure 34, saturation magnetization is reached at a relatively high magnetic field (~2.1 T) in comparison to data on martensite single crystals shown in Figure 55 (the comparison to martensite is justified by the conclusion that the deposited samples exist as martensite at room temperature, which will be given in section 5.3). The saturation magnetization value is on the order expected for Ni-Mn-Ga, but specifically approaches that of NM martensite in Figure 55. Also, the increase in magnetization is also seen to be rather gradual. Nearly identical behavior, but at lower field strength, was also observed in polycrystalline Ni-Mn-Ga produced by sintering [63] (but without the abnormal inflection points, discussed in the next sub-section). The following discussion addresses this gradual, high-field saturation behavior.

At a sample temperature of 87 °C, Heczko et al. [60] observed slowly increasing magnetization up to 2.0 T, which would continue further if this was not the highest field used. At the next lower sample temperature, the increase in magnetization is much more rapid. The increase is slightly more rapid at each subsequent lower temperature, with the exception of the lowest temperature (-173 °C). The authors attribute this to the proximity of the 87 °C curve to the Curie temperature (from these authors' plotted data, the Curie temperature for this sample is approximately 100 °C). It may be that, due to the proximity of the Curie points of the deposited samples in this work (78 – 80 °C) to room temperature (at which the M vs. $\mu_0 \cdot H$ curves were collected), the same effect is the cause of the gradual, rounded approach to saturation magnetization. However, it is acknowledged that the in the cited study, the 57 °C curve was closer in temperature to the Curie point than the samples in this thesis are to their Curie points, but did not show nearly as gradual of an approach to saturation (a difference of 45 °C versus a difference of 55 °C or more).

Another consideration is the contribution of varying orientations, and possibly of multiple structures of martensite. Variations in orientation are likely present in the samples in a way that influences VSM experiments. Laser metal deposition can and often does produce columnar

grains (preferred orientation) under suitable processing parameters [94], and the preferred direction of these columnar grains is often oriented normal to the substrate [94] or at least in a range of directions largely similar to but deviating from the normal to the substrate [75]. These columnar grains can have a preferred crystallographic direction, as mentioned in the last study cited. The mounting of deposited samples in the VSM was such that the field direction was approximately along the sample's transverse direction, which is perpendicular to both the laser travel and normal directions. Thus, if columnar grains are present, various crystal directions with a corresponding range of magnetic softness/hardness would have been aligned with the field. This would extend the M vs. $\mu_0 \cdot H$ curve's approach to saturation. However, if this effect alone were to explain the increased saturation field, it would have to be stronger than in the sintered polycrystal study mentioned earlier [63]. Additionally, as discussed in section 5.3, the presence of multiple martensite structures has not been completely ruled out. Variation in the shape of the curve as saturation is approached, and strength of the magnetic field at saturation, for various orientations and structures of martensite single crystals, is seen in Figure 55 (created with data from [12]). As shown, the saturation fields for these samples of different martensite structures vary. With a sufficient number of grains at various orientations and/or of multiple structures, it may be possible to create the rounded curves seen for the deposited samples (without producing a curve with visible steps). Finally, reorientation of the lattice of grains through twin growth may be a possible, small effect. If twin boundaries are able to move in some volumes of the sample, they will cause reorientation of the magnetically easy axis to a direction more closely aligned with the applied field, thereby increasing the sample's magnetization. However, it is expected that twin boundary motion can only happen in a small portion of the sample. This possible effect is discussed further in the next sub-section.

In summary, the slow approach to a high saturation field might be caused by proximity to the Curie temperature, by the contribution of harder directions from the polycrystal, and even possibly − although less likely − by the presence of multiple martensite structures.

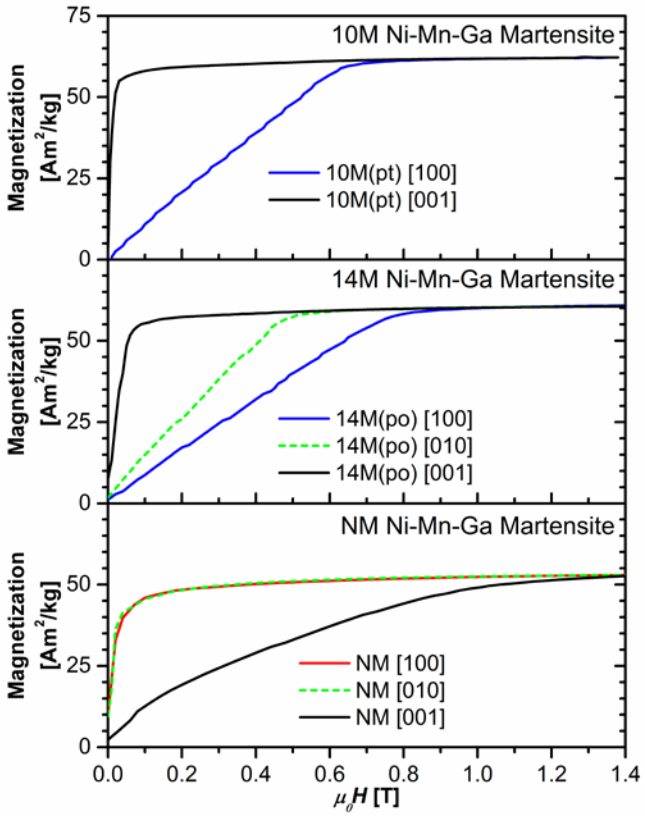

Figure 55. Magnetization vs. magnetic field strength data obtained by VSM for Ni-Mn-Ga single crystals along each orthogonal crystal axis of the pseudo- unit cells. Subplots show data for each of the martensite structures. Created with data from [12]**. (This figure is identical to the earlier Figure 15).**

5.2.3 Inflection points in the *M vs.* $\mu_0 \cdot H$ curves

Inflection points in the *M* vs. $\mu_0 \cdot H$ curves (most visibly in Figure 35 of section 4.3), which should not appear on "textbook" ferromagnetic curves, are possibly evidence of twin boundary motion [60]. The points in question are those points where the curve changes the sign of its curvature, found in segments of the curve in the region between fields of -0.5 T and +0.5 T. The *M* vs. $\mu_0 \cdot H$ curves must of course change curvature between the top and bottom part of the plot, but do so by transitioning through a nearly-linear region of indiscernible curvature (near the horizontal axis). The points in question are additional and noticeable curvatures in what would otherwise be the linear region, reuaslting in widened areas of between the curves. These features are similar to those seen in Fig. 3(b) of Heczko et al. [60], who attributed their presence to twin

boundary motion driven by the applied field. However, the M vs. $\mu_0 \cdot H$ curves within this thesis do not show two widened areas in one quadrant of the plot as the curves in the previously mentioned study and in [61] do. The cited articles show widened areas at the origin of the plot and again before the hysteresis curves collapse on themselves at higher field. In this thesis, the areas between M vs. $\mu_0 \cdot H$ curves are only widened once in each quadrant of the plot, and in the vicinity of the origin of the plot, the curves actually have a narrower area than in the widened area. The reason for the difference in magnetic hysteresis behavior is not known. At least the possibility that the shape of the curve is the result of a measurement artifact seems to be ruled out by an experiment, run with the same parameters on a pure nickel standard, that does not show the same anomalous shape.

It is reasonable to question whether twin boundary motion is physically possible in the deposited samples. The answer is likely that, to some degree, twin boundary motion is possible. The surfaces of the sample not used for sample attachment in the VSM experiment are free surfaces, which likely include the surfaces of multiple martensite grains. These surfaces could potentially allow movement of twin boundaries. As twin variants hypothetically grow or recede, they would cause the observed inflection point effect on the M vs. $\mu_0 \cdot H$ curves. Then, it must also be asked whether the twins involved make up sufficient volume (mass) to create enough of an influence on the overall magnetization of the sample − especially since they are only supposed to be in those grains with free surfaces. Due to the small size of the samples, it may be said that the deposited samples do have a considerable amount of surface area compared to their volume, giving favor to the possibility of observing twin boundary movement by magnetic means. Of course, this motion would best be confirmed by other means, for example by exposing the sample to a 1 T or -1 T magnetic field and observing twins by optical microscopy before and after each exposure.

5.2.4 Curie points

Comparing the Curie points of the samples (78 – 80 °C, choosing the “quasi-settling” data from Table 15 of section 4.1) and their measured compositions (approximately $Ni_{53}Mn_{27}Ga_{20}$) to a compilation of reported values (Figure 56, reprinted from [95]), good agreement is seen. The composition of the deposited samples falls about halfway between the 67 and 87 °C curves in the

figure, and so 78 – 80 °C Curie points are expected. However, it must be noted that the nearby data point for a composition of $Ni_{53.1}Mn_{26.6}Ga_{20.3}$ is a Curie point of 100 °C (by consulting [90]), so this particular data point does not correspond with the mentioned curves. Noting this, it may be that a 78 – 80 °C Curie point should not be expected after all. However, Lanska et al. [89] reported a Curie point of 71 °C in a $Ni_{53.7}Mn_{26.4}Ga_{19.9}$ sample, which does agree well with the results for the deposited samples.

It is interesting to note that the 200 W sample has the steepest approach to the Curie point, or in other words has the most rapid change to paramagnetism (demagnetization) with respect to temperature. This is consistent among all of the *M* vs. *T* data sets (Figure 36 − Figure 39 of section 4.1). Perhaps this indicates greater homogeneity in the 200 W sample.

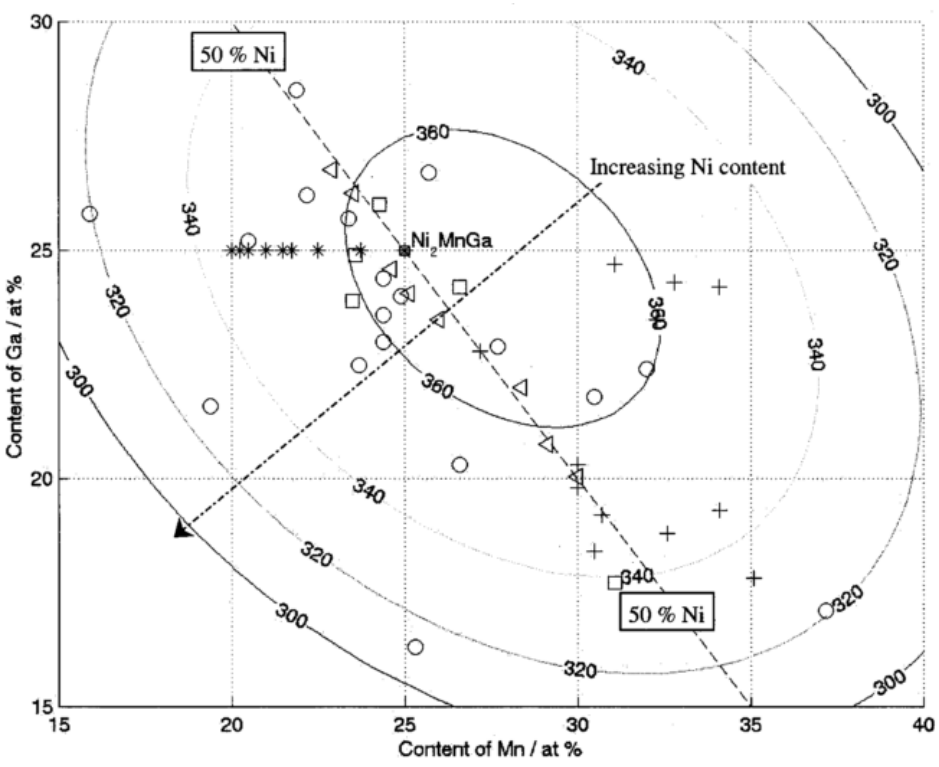

Figure 56. Compilation and curve fitting of Curie temperature data from literature. Reprinted from Empirical mapping of Ni–Mn–Ga properties with composition and valence electron concentration by X. Jin, M. Marioni, D. Bono, S. M. Allen, R. C. O'Handley, and T. Y. Hsu, Journal of Applied Physics 91, 8222 (2002), with the permission of AIP Publishing. [95]

5.3 PHASE

In the small size Ni-Mn-Ga powder, phase transformations induced by temperature change are investigated in DSC data (Figure 32, found in section 3.3). No transformations are revealed in the as-received powder – the DSC curve lacks distinct features and consists of gradual changes in slope over the entire range. The annealed material, however, clearly shows transformation to austenite and clearly shows the Curie point. Such improvement in DSC data has also been seen in ball-milled powder [88]. The appearance of transformations after annealing is due to their suppression in the as-received powder, which was produced by mechanically breaking an ingot into smaller pieces. Residual stresses imparted by the mechanical processing likely prevented the transformation to austenite from occurring within the expected temperature range, and may also have shifted or otherwise obscured the Curie point. Although it is true that the powder used for the DSC experiment was the small size range powder, while the feedstock powder was the large range powder, the results should not be excessively affected. Although the larger surface-to-volume ratio of the small powder may have a negligible effect on transformations, the possibility that the small powder particles inherited higher residual stresses from mechanical processing is more important. After annealing, this difference between the two powders would be removed and results from DSC scans of the two powders should yield the same result (if the larger powder were also annealed and analyzed). Turning to literature, the only transformation temperatures for alloys of similar composition (within 1 at% for all three elements; this is high in Ni relative to most of the field) found as of this writing come from two articles [81,89]. These values are listed in Table 17, alongside the values found in section 3.2 for the small-size powder. The values from the article by Lanska et al. are noticeably higher: for the austenitic and martensitic transformations, all of the values are 50 °C higher or more. Observing values from the article by Wu and Yang, one of the compositions shows transformation temperatures which are within 19 °C or less of those measured within this study.

If it is possible that the form of the samples (bulk samples cut from an ingot in the article instead of powder) has a significant effect, other studies with powder might show a similar discrepancy with this data set. However, in [21], a powder of size comparable to that used in this thesis showed transformation temperatures within 10 °C of comparable compositions in the data set in [89]. Comparing another article which utilized powders (produced from single crystals)

and found the martensite start temperature M_s [44] to data from comparable compositions in [89], the spread is less than 20 °C. So, the use of powder is not a likely explanation for measuring lower transformation temperatures than those found in literature.

As of this writing, this lack of agreement with literature is not explained. If all of the literature data were taken as accurate, then the conclusion would be that transformation temperatures in the Ni-Mn-Ga system are extremely sensitive to composition. It is also acknowledged that variation in errors in composition measurement might create a discrepancy in measured compositions, and that small discrepancies in composition could cause the magnitude of difference in transformation temperatures just discussed. Of the articles cited, one used EDS within an SEM and three used WDS within an EPMA (WDS generally gives reduced uncertainty in measured composition). Of the articles that used WDS, one reported calibration by reference samples (whose composition was measured by coupled plasma-atomic emission spectrometer (ICP-AES)).

Table 17. Comparison of transformation temperatures measured for small-size powder to transformation temperatures from literature.

	Source	**Composition***	A_s	A_f	T_C, **heating**	T_C, **cooling**	M_s	M_f
	This work (small-size powder, annealed)	Measured: 51.8-27.9-20.2 Reported: 51.5-26.3-22.2	47	66	88	87	55	41
Compositions approaching Measured	Lanska et al. [89]	52.3-27.4-20.3	130	135	107		125	118
		51.7-27.7-20.6	108	121	113		110	96
Composition approaching Reported	Lanska et al. [89]	51.5-26.8-21.7	107	127	104		120	101
	Wu and Yang [81]	50.5-26.7-22.8	6	13	-	-	-8	-19
		52.1-25.2-22.7	64	81	-	-	58	39

All values are given in °C
*Compositions are given as Ni-Mn-Ga in at%

For the deposited samples, phase transformations induced by temperature change were explored with DSC (Figure 40 - Figure 42) and magnetization versus temperature (*M* vs. *T*) data obtained by VSM (Figure 36 − Figure 39). In DSC data, a transformation would be shown as a clear peak in heat flow; in the M-vs.-T data, a transformation would be shown as a change in magnetization from one approximately constant level to another. None of the data sets presented display such behavior. Instead, each DSC experiment shows what at first appears to be one extremely broad peak over almost the entire range investigated; however, there are many sharp changes in slope which reveal that the peak is not one peak at all. In the case of the *M* vs. *T* data, while a constant magnetization is seen at low temperatures (and while it is likely that a constant magnetization at high temperatures would be present would it not be for the interfering presence of the Curie temperature), the breadth of the transformation and its shape are out of the ordinary. The reason why these results are considered abnormal and their possible causes will be discussed next, but the most basic conclusions should be stated now. First, although the completion of the austenitic transformation is not seen with *M* vs. *T* data, it is potentially found to be in the vicinity of 90 °C for all three samples from DSC data (Figure 41 and Table 16, found in section 4.1). Furthermore, it is clear from the *M* vs. *T* data, and especially from data collected using the PPMS VSM (Figure 36 and Table 15, found in section 4.1), that the austenitic transformation starts at or above room temperature for all three samples (~20 °C for the 200 W sample, ~20-25 °C for the 250 W, and ~25 °C for the 300 W). From DSC data, austenite start temperatures were potentially found to be 30 °C, 40 °C[7], and 27 °C for the 200 W, 250 W and 300 W samples respectively (although with much uncertainty, because these values are based on changes in slopes of curves which may have already had slopes and already had other, less significant changes in slope. The slope change chosen may not correspond to the first onset of austenite, but perhaps to onset of austenite in the largest total sub-volume in the sample). It may be that only a minority of the sample begins transforming at the temperatures found by VSM, and significant transformation begins nearer to the temperatures found by DSC. Searching for comparable data in the literature, only two articles have data for a composition similar to that of the samples (within 1 at% of

[7] For the 250 W sample, the curve had continued with a significant slope from the beginning temperature of the DSC heating run, and the austenite start temperature was measured at a noticeable change from this slope.

$Ni_{53}Mn_{27}Ga_{20}$ for all three elements simultaneously): Lanska et al. [89] for $Ni_{53.7}Mn_{26.4}Ga_{19.9}$, and [90] for $Ni_{53.1}Mn_{26.6}Ga_{20.3}$. The first result shows austenite and martensite start and finish temperatures ranging from 239 – 273 °C, far removed from all of the data points just mentioned for the deposited samples. The second result is a martensitic transformation temperature of 93 °C (measured at the peak in the DSC curve on cooling), which is considerably closer to the available data for austenitic transformation in the samples. Regardless of these very varied comparisons to literature, the most basic conclusion can be drawn from the experimental data. It is concluded that the samples consist entirely of martensite at room temperature, an important goal of this study. If austenite or any other phase is present, its proportion is very small and not easily detected by the methods used. Additionally, looking below room temperature (Figure 36), no intermartensitic transformations are found from room temperature to as low as -50 °C, which is the lowest temperature investigated. Intermartensitic transformations may, however, contribute to the breadth and complexity of the observed austenitic and martensitic transformation, if an intermartensitic transformation occurs in these temperature ranges.

The breadth and multiplicity of the transformations observed will now be discussed. It can be seen in both the DSC and VSM *M* vs. *T* data that transformations are detected over a wide temperature range of 60 °C or more, which far exceeds that seen in single crystals [12] [44], polycrystalline bulk samples [88], a polycrystalline thin film [91], and a powder [21]. As counter examples, orthorhombic martensite single crystals were found to transform over a broad range (~45 °C in one case) in [44]; ball-milled, annealed powders showed an indistinguishably broad transformation with DSC in [88]; samples prepared by sintering (with compaction) of powders produced by crushing of rapidly solidified, melt-spun ribbons showed complex, multi-faceted DSC curves for all samples and broad transformations in VSM *M* vs. *T* experiments for samples with the 14M (pseudo-orthorhombic) structure [63]. Of these, only the latter exceeds the breadth observed for deposited samples in this work. Examining the DSC data (Figure 40 – Figure 42 of section 4.1) more closely, transformation temperatures and ranges are difficult to discern, and distinct peaks were identified on heating for only two of the deposited samples (shown in Table 16 for the 20 °C/min data). Furthermore, these peaks are not lone, singular peaks, but only the most distinct of many points along the curves which give the appearance of less pronounced peaks. This is paralleled in the literature only by the previously mentioned study of sintered, melt-spun material [63], where DSC curves also featured many smaller peaks and complex

features, perhaps to even a greater extent. Moving to the *M* vs. *T* data (Figure 36 – Figure 38 of section 4.1), again, broad transformation behavior is seen (compare to a more usual example of transformation behavior, shown in Figure 57 below), but the extent of the transformation in the low-temperature limit can be determined by observing the transition to a horizontal or near-horizontal slope (especially from data which continues below room temperature, shown in Figure 36). On the high-temperature end of the transformation, the Curie temperature occurs while the curve is sloped, making observation of the high-temperature (austenite finish) end of the transformation impossible by VSM. Like the DSC data, the *M* vs. *T* data is further complicated by the presence of points where the slope of the curve changes abruptly during the transformation. However, the austenite finish temperatures obtained from DSC data may be used to approximate the high-temperature end of the transformations. Comparing the austenite start values obtained by PPMS VSM (Table 15) and the austenite finish values obtained from DSC data (Table 16), the breadth of transformations may be as much as 76 °C, 66 °C, and 62 °C for the 200 W, 250 W and 300 W samples respectively.

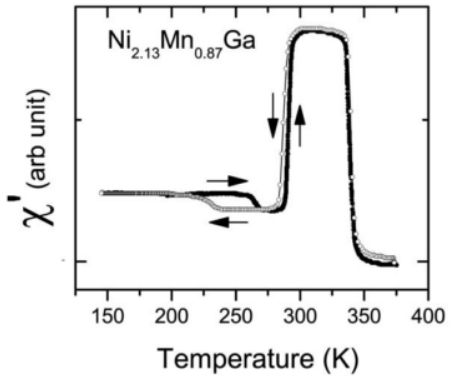

Figure 57. Susceptibility vs. temperature experiment which demonstrates the expected shape of the *M* vs. *T* curves for Ni-Mn-Ga with transformation near room temperature. The intermartensitic transformations (modest change from one constant value to another) in the range of 200 K to 275 K are not necessarily expected, but the pronounced move to/from a high, constant value demonstrate the austenitic/martensitic transformations respectively. The entire sample is in the austenite phase at the high, constant value. The sharp decrease/increase to a minimal value at just below 350 K is the signature of the Curie point. Reprinted figure with permission of the publisher from Ranjan, Rajeev; Banik, S; Barman, S R; Kumar, U; and Mukhopadhyay, P K; Pandey, Dhananjai; Physical Review B, 74, 224443, 2006. Copyright 2006 by the American Physical Society. http://dx.doi.org/10.1103/PhysRevB.74.224443 [92]

Broadening of transformations might be caused by defects, such as grain boundaries, and inclusions, and by residual stresses. All of these may be expected in material produced by a laser metal deposition process. Heczko et al. [60] reported a broadened transformation in a Ni-Mn-Ga thin film, and gave constraint by the film's substrate as a possible explanation. However, the additional points of change in slope and/or curvature in the DSC and VSM data in this thesis point to yet another cause of transformation breadth. It is possible that multiple, overlapping transformations occur in the deposited samples, producing seemingly broad transformations with many peaks or points of sudden change. This could result from volumes of the deposited sample transforming non-homogeneously (at different temperatures) due to compositional gradients, or even shifts in the transformation temperatures caused by a distribution of residual stresses. Furthermore, the presence of one or more intermartensitic transformations in the vicinity of the martensite-to-austenite transformation cannot be ruled out, and may complicate the picture further. Finally, individual transformations themselves may be broadened by the effects discussed previously. On the other hand, defects and compositional gradient may not be the only causes of broadened transformations. Richard et al. [44] argued that the higher strain energy of orthorhombic martensite (as opposed to tetragonal martensite) provides a greater barrier to transformation, resulting in broadened transformations. However, in that study, the broadened transformation was a smooth curve in M vs. T data, without any of the abrupt changes seen in the data in this study. So, if orthorhombic martensite is present in a significant proportion in the deposited samples, its presence alone cannot explain all of the irregular features of the observed transformations.

To summarize, the feedstock powder exists as martensite at room temperature after annealing, and all of the deposited samples are in the martensite phase either at room temperature or near room temperature (~20 °C in the case of the 200 W sample). Transformation to austenite is complicated and takes place over a wide temperature range (60 °C or more in breadth). The austenite finish temperatures cannot be determined with certainty, but DSC data from the 250 W and 300 W samples potentially places austenite finish temperatures near 90 °C for large portions of those samples.

5.4 MICROSTRUCTURE AND COMPOSITION

Microstructure and spatial variation in composition are often intertwined in rapidly solidified material, such as that produced by laser metal deposition. For this reason, they will be discussed together in this section.

From examination of optical micrographs, it is clear that the microstructure of the deposited samples is complex. Discussing porosity first, the samples contain large pores (or voids) and smaller features that may also be pores. The larger voids (visible at low magnifications in Figure 45 − Figure 47, Figure 52 − Figure 53, Figure 50 of section 4.5) are mostly spherical in shape while some have irregular shapes (Figure 50). Kobryn et al. [96] concluded that spherical pores are the result of entrapment of gas (introduced either in the powder feeding/deposition process, or by release from powder particles) and called these “gas porosity”, and also explained that irregular pores form when particles do not melt sufficiently to coalesce into a dense material and called these “lack-of-fusion” pores. Both, or at least the former type, are probably exacerbated by the angular feedstock powder particle shapes used in this thesis. The latter type is influenced by the laser energy density delivered to the material and other related heat transfer details. Less clearly, the smaller features (visible as black spots in Figure 51 and as dark spots in Figure 54) seem to be pores, although their appearance under DIC may cast some doubt on that conclusion. Given the length scales involved, these pores may have been present in the feedstock powder if indeed they are pores. Cross-sectioning of the powder would aid in the understanding of these small spots. in any case, porosity of the length scales and volume fractions seen is insignificant compares to that of Ni-Mn-Ga foams, and so is not likely to have any effect on MFIS.

Moving to the grain structure, differential interference contrast (DIC) micrographs reveal that the polished cross-sections of the samples have surface relief, with shapes elongated in the normal direction as the most prominent features. These features are likely grains. Perhaps these grains have a mechanically harder orientation relative to the surface, leaving them with a microscopically smaller amount of material removal during polishing and thus making them visible under certain conditions in optical microscopy and especially under DIC. After heating the sample in order to completely transform it to austenite and allowing it to cool back to room temperature − transforming again to martensite completely or almost completely – the surface

relief becomes much more intricate. Transformation from austenite to martensite, with the constraint by the mounting on most of the sample and lack of constraint on one surface, appears to cause roughening of the surface (on the small scale that is discernable with DIC). As twinning accommodates the lattice mismatch between austenite and martensite during cooling, even an unconstrained sample may show microscopic surface relief due to twinning. In the deposited samples, as used in the DIC experiments, constraint from the epoxy mounting prevents twinning from proceeding as normal, and may exacerbate the surface relief. Finally, the surface relief is of an appropriate scale for viewing with DIC.

Twinning is directly visible under multiple imaging modes, including backscattered electron imaging, darkfield optical microscopy, and DIC (Figure 50 − Figure 54 of section 4.5) as parallel bands. Regions of bands (twins) were seen to appear in irregularly shaped areas, potentially corresponding to grains. Because twinning occurs in only certain orientations, twin variants appear as bands (much like lamellae), and in any one cross-section of a polycrystal, not all grains will be sectioned on a plane which shows multiple variants (that is, perpendicular to the length of the metaphorical “lamellae”). Thus, even if the entire sample consists of twin variants, they would not be seen to cover the entirety of the images taken. Notably, bands were seen to cross the boundaries between deposition layers (Figure 52 − Figure 54 show an example of this), and so, it appears that twins may cross these layer boundaries. This may imply that there is epitaxy between layers and that this epitaxy later allows for formation of some continuous twin variants upon transformation to martensite. If confirmed by future investigation, this finding may be significant.

Etched cross-sections show dark contrasting features, suggesting micro-segregation, in all regions of the sample. In the top layers of the sample (last to be deposited), this contrast clearly forms dendritic structures (seen in Figure 49), while in lower layers (previously deposited), the contrasting features are not distinctly dendritic. This is a result of remelting and reheating cycles experienced by previously deposited material, as noted in a study of another material processed by LENS [87]. The top layer is unique in that it sees minimal reheating or remelting (any reheating and remelting is only due to the second, antiparallel line deposited during the second half of the building of this layer, as seen in the deposition path shown in Figure 21 of section 2.1.5).

Comparison of DIC micrographs and micrographs of etched samples reveal that grains (seen as the large oval-shaped regions in Figure 45 − Figure 47 of section 4.5) extend perpendicular to lines of chemical segregation in reheated/remelted layers (seen in Figure 48). This relationship is demonstrated for one sample by overlaying the DIC and etched micrographs to create a single image (Figure 58), and by highlighting directions with overlaid sketches on regions DIC images (Figure 59, which is formed from regions of Figure 46). These features show the direction of grain growth as almost normal to the substrate, but with a slight deviation from normal which alternates between layers. This deviation is the result of the direction of the laser within a given layer – as the heat source passes by a fixed location, the larger (hotter) trailing end of the temperature distribution creates a thermal gradient which is at an angle to the normal direction (directions are defined in Figure 23 of section 2.1.5). A similar observation of grain growth directions following the passing heat source in LENS was described in [75].

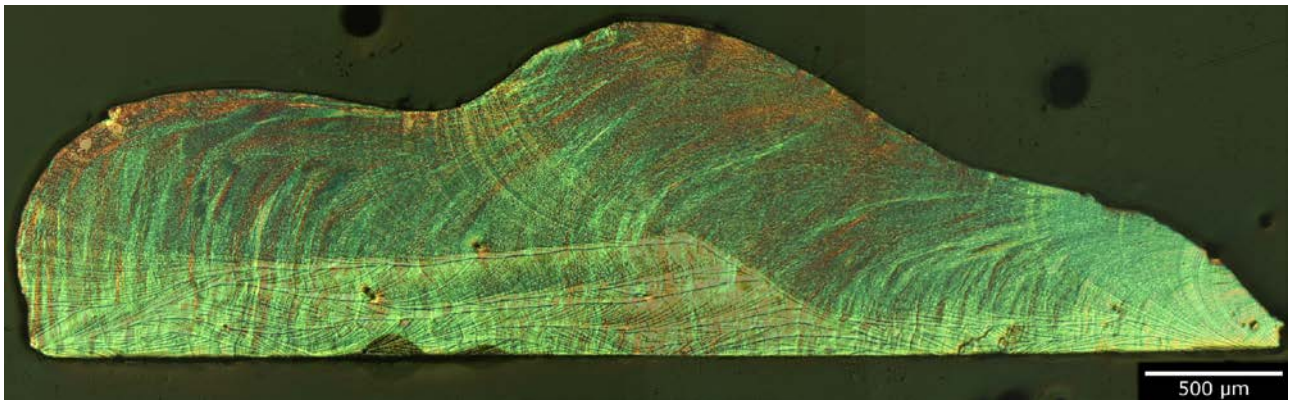

Figure 58. Transparent overlay of micrograph of etched 250 W sample and DIC micrograph of the sample after heating. Segregation lines (dark lines) can be seen running perpendicular to lines of similar elevation in the DIC image (shades of red and blue), which are likely to be grains or martensite variants.

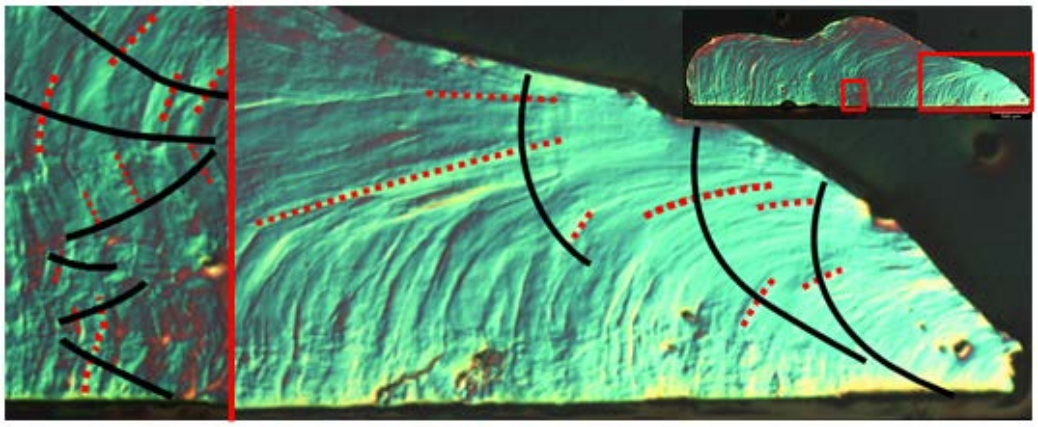

Figure 59. Selected regions of composite images created from DIC micrographs of the 250 W sample. Overlaid black lines show the locations of segregation lines (dark lines) that were revealed in micrographs of the sample after etching. The red dotted lines trace points of similar elevation in the DIC micrograph, following what appear to be grains or martensite variants. The locations of the two regions shown are highlight by red outlines in the inset at the top-right.

In addition to the segregation visible in the etched images, changes in composition across the sample (macro-segregation) were investigated by EDS line scans. EDS efforts did not reveal any systematic compositional variation (although perhaps improved use of EDS including parameter selection might have yielded a better result).

To summarize, the deposited samples contain a microstructure which features columnar grains, dendrites, twinning and porosity. Columnar grains and dendrites are associated with the laser metal deposition process. Twins appear to cross layer boundaries, which suggests epitaxial growth of grains in subsequent deposition layers.

5.5 INFLUENCE OF PROCESSING PARAMETER

This section will focus on effects which can be traced to choice of processing parameter (the experimental variable). It will also draw comparisons to the feedstock powder, and therefore will explore the effect of processing.

First, no clear effect of processing parameter on microstructure was observed, largely because a complete analysis of microstructure may be beyond the scope of this work. Moving to phase, the samples were present as martensite at room temperature regardless of choice of processing parameter, matching the feedstock powder. Continuing on to transformation behavior, the austenite start (A_s), austenite peak (A_{peak}) and austenite finish (A_f) temperatures are available for comparison among the deposited samples and the powder. These values are summarized in Table 18 (below). The start of the austenitic transformation differed by up to 10 °C among the three deposited samples, with the 200 W sample having the lowest start and the 300 W having the highest (based on VSM results, which are more accurate in this thesis). The DSC results show an increase in the peak of the austenitic transformation in the deposited samples over the powder. Because the peak position is the most reliable measurement in the observed data, this may be a legitimate result. The austenite finish (A_f) was also only measured from DSC data, and due to the difficulty in determining it from the curves, it is not reliable. However, it will be noted that the 200 W sample had the highest measured A_f. Comparing to values for the powder (measured with DSC, but with confidence), processing clearly resulted in a spread in the austenite start and austenite finish temperatures. In others words, the austenitic transformation was broadened, as stated before. From the VSM data (Figure 36 of section 4.1), it is seen that the same has happened to the martensitic transformation – as should be expected, because the transformations are each other's conjugates. Considering the experimental variable of laser power, it would seem that the lowest laser power resulted in the lowest A_s and possibly also a higher A_f, leading to the most broadened transformation. This, however, cannot be treated as conclusive, both because of the instability in processing mentioned earlier (section 5.1) and because the A_f value is not reliable.

Table 18. Comparison of transformation temperatures acquired for powder and deposited samples by both DSC and VSM (as applicable). Temperatures include the austenite start (A_s), austenite peak (A_{peak}), austenite finish (A_f) and the Curie point (T_C).

	DSC	VSM, DSC *		
	Powder, annealed	**200 W**	**250 W**	**300 W**
A_s, °C	47	17, 30	22–27, 40	27, 27
A_{peak}, °C	58	- , -	- , 67	- , 70
A_f, °C	66	- , 93	- , 88	- , 89
T_C, °C	87–88	80, -	78, -	78, -
* Pairs correspond to VSM result and DSC result, in that order. "-" indicates a value which was not discernable from the data.				

The processing parameters had no clear effect on overall composition, potentially because the measured differences in measured compositions are well below a conservative uncertainty for EDS measurements. Relative to the feedstock powder measured composition, Ni increased by 1 at% (but it should be noted that the standard deviation of the powder data was 0.7 at%, while for deposited sample data it was of order 0.1 at% – whether this is due to actual composition variation in the powder is not clear). The Ni increase is explained by loss of chiefly Mn. Ga loss of more than 0.1 at% (specifically 0.2 at%) relative to the measured powder composition was measured for only one sample (the 200 W).

While no conclusion has been drawn about the relative compositions of the samples directly, the samples do differ in Curie temperature - which is highly sensitive to composition. The Curie temperature was the same in the 250 and 300 W samples, but was 2 °C higher in the 200 W sample. *Tc* for the powder is not directly comparable, because VSM *M* vs. *T* was unfortunately not conducted on the powder as of this writing. However, because DSC was conducted in both heating and cooling at a minimal rate, and because the Curie point was visible in both, the DSC data makes a sufficient substitute. The *Tc* for powder (from DSC data) compared to *Tc* for deposited samples (from *M* vs. *T* data) is 87 – 88 °C versus 78 – 80 °C. Consulting Figure 56 (section 5.2.4) indicates that the powder should indeed have a higher Curie temperature. This holds regardless of whether we consider the measured or reported

composition, as both are a shift to higher temperatures over the T_C for the measured composition of the deposited samples. Thus, the decrease in *Tc* after processing is likely due to the change in composition. In a parallel to the Curie point, the saturation magnetization was the same in the 250 W and 300 W samples, but was 10 % higher in the 200 W sample. The 200 W sample also produced the steepest slope of the M vs. T curves at the Curie point (most rapid demagnetization), possibly suggesting that this sample had the greatest chemical homogeneity.

In closing, it must be emphasized that while it may be tempting to attribute the change in magnetic properties to change in the value of the experimental variable (laser power), there exists great variation within and among the samples which is not explained solely by laser power. Possible reasons for this were discussed in section 5.1, with emphasis placed on unsteadiness in the powder flow rate (although an overall trend of greater deposited mass per length of line with greater laser power was acknowledged). Additionally, perhaps a greater range of laser power between samples may have made clearer differences between samples. However, the fact that the lowest laser power sample has a lower *Tc* does correspond with Figure 56, because a *Tc* decrease should be caused by an Mn decrease (if Mn is the element being taken away). If Mn is the main element lost, as determined from overall composition measurements relative to the powder, its loss would likely be exacerbated by higher laser power. Thus, this may be a plausible reason why the lowest laser power sample possessed the highest Curie temperature. However, the observation that the Cure point of all the deposited samples decreased relative to its value in the powder feedstock seems contradictory to this conclusion. If laser processing consistently decreased the Curie point, then one might simply expect increased laser power to further decrease the Curie point.

6.0 CONCLUSION

- Directed energy deposition, specifically laser metal deposition, was used to deposit Ni-Mn-Ga samples with two of the properties prerequisite for magnetic field-induced strain:
    - the samples are ferromagnetic at room temperature
    - martensite is the majority phase (or only phase) at room temperature
- The samples' dense, polycrystal microstructure may pose a barrier to MFIS. However:
    - columnar grains oriented in directions similar to the normal direction predominate in remelted/reheated layers of the sample, which may be a promising microstructure for MFIS, and
    - porosity was found in the samples, but not in sufficient levels to potentially be beneficial to MFIS
- Indirect evidence of twin boundary motion has been found:
    - twin boundaries appeared to cross deposition layer boundaries, implying epitaxy between layers and formation of continuous twin variants, and
    - magnetization experiments showed changes in curvature which are an indication of twin boundary motion.
- Concerning transformations, both the feedstock powder and the deposited samples were found to have transformation temperatures that do not agree well with literature.
    - The austenite start temperatures of the deposited samples were found to be around room temperature (17 – 27 °C), but only a small fraction of the transformation had occurred before this range was exceeded.
    - Notably, the austenitic transformation was significantly broadened in each sample − to about three to four times its width relative to the feedstock powder. The Curie

temperature was only mildly less desirable than that of the feedstock powder, decreasing by no more than 10 °C.

- Processing consistently resulted in an approximately 1 at% decrease in Mn and an approximately equal increase in Ni relative to the powder feedstock.
    - This may inform the selection of feedstock powder composition for a desired as-processed composition.
    - Compositional differences across the sample may be so small that they are not easily measured by EDS (or were not detectable with the beam parameters used).
- The influence of the experimental variable (laser power) on the samples was not readily identified.
    - Difficulty in holding the process constant in other respects (maintaining a steady rate of deposition) and possibly also the small range investigated in the experimental variable may have contributed to this lack of a finding. However, it is seen that out of the three samples, the deposition of the 300 W sample was most consistent.
    - A possible link between decreased laser power and increased Curie temperature was noted. This conclusion, however, seems in contradiction with the fact that laser processing decreased the Curie temperature relative to the powder feedstock for all samples.
- The hypothesis was shown to be true: Ni-Mn-Ga feedstock, of composition to be present as martensite at room temperature, was deposited via directed energy deposition method and the resulting samples were found to be present as martensite at room temperature. This conclusion was reached by indirect means, including transformation behavior and evidence of twinning in optical microscopy and magnetization experiments. Thus, the objectives chosen to investigate the hypothesis (section 1.2) were achieved.

7.0 OUTLOOK

This work showed the potential of a full-melting additive manufacturing process to alleviate some of the problems and achieve some of the innovations given as motivation in the Introduction. Segregation may have been limited to small scales, the samples were produced rapidly, and epitaxy (potentially leading to preferred orientation) may be present. As is often the case, more work will be needed before challenges are overcome and the potential of this processing route for Ni-Mn-Ga and other magnetic shape memory alloys is fully explored.

Promising outcomes for functionality thus far include the ferromagnetic state of processed material at room temperature with only a moderate decrease in Curie temperature, the existence of the material as martensite at room temperature, and possible magnetoplasticity. On the other hand, potential challenges include a near-room temperature onset of the austenitic transformation and probable microstructural inhomogeneity.

Possible future work may include:

1) further understanding of the deposited material,

2) improvements to the present deposition process, and

3) advanced processing and post-processing leading to MFIS-capable samples.

In the first category, there is an immediate need to determine the martensite structure by diffraction, and to attempt twin movement observation by optical microscopy (in order to confirm upon the indirect evidence of magnetoplasticity). Furthermore, sectioning in the two directions normal to the one used in this thesis would likely further understanding of the microstructure and could provide more information about compositional gradients. Also, sectioning into thin slices could be used to produce detailed spatial results. Additionally, comparison of single-layer and multi-layer samples would elucidate effects of subsequent layers in processing. In the second category, improved powder feedstock with less angular features − although difficult to produce from Ni-Mn-Ga due to its brittleness − would likely improve the

consistency of deposition. Just as importantly, post-processing by annealing or other heat treatments may improve properties of interest. In the final group, concepts such as epitaxial growth from a single crystal, optimization of columnar microstructures or intentional porosity may improve the outlook for MFIS in Ni-Mn-Ga builds. Ultimately, the motivating vision for future work is a demonstration of significant MFIS in a sample produced by an additive manufacturing process.

APPENDIX

LIST OF SYMBOLS

Units

Symbol	Name	Corresponding Quantity
Å	angstrom	length
A/m	ampere per meter	applied magnetic field
$A \cdot m^2$	ampere-meter^2	magnetic moment
$A \cdot m^2/kg$	ampere-meter^2 per kilogram	mass magnetization
at%	atomic percent	atomic ratio (for composition)
at %	atomic percent	atomic ratio (for composition)
°C	degree Celsius	temperature
emu	*	magnetic moment
g	gram	mass
G	gauss	magnetic field strength
Hz	hertz	frequency
keV	kiloelectronvolt	energy
K	Kelvin	temperature
	liter	volume
m	meter	length
MPa	megapascal	stress
mm	millimeter	length
N	newton	force
nm	nanometer	length
Pa	pascal	pressure

ppm	parts per million	concentration
T	tesla	magnetic field strength
V·s/(A·m)	volt-second per ampere-meter	magnetic permeability of free space
W	watt	power
µm	micrometer	length

*According to some sources, emu is not a unit, but is equivalent to erg/G, where erg is the cgs system's unit of energy and G is as defined in this list.

Quantities/Variables

Symbol	Description
a	first dimension of unit cell (lattice parameter)
A_s	austenite start temperature
A_f	austenite finish temperature
A_{peak}	austenite peak temperature
b	second dimension of unit cell (lattice parameter)
c	third dimension of unit cell (lattice parameter)
M	mass magnetization
M_s	martensite start temperature
M_{sat}	saturation mass magnetization
M_f	martensite finish temperature
M_r	remanent mass magnetization
M_{peak}	martensite peak temperature
H	applied magnetic field
H_C	coercive magnetic field
B	magnetic field strength
K	magnetic anisotropy energy
T	temperature
T_C	Curie temperature, also known as Curie point
V	volume
x	1) length or 2) variable for families of compositions

α	first angle between axes of unit cell (lattice parameter)
β	second angle between axes of unit cell (lattice parameter)
γ	third angle between axes of unit cell (lattice parameter)
μ	magnetic permeability
μ_0	magnetic permeability of free space
μ_m	magnetic moment
μ_{orb}	orbital magnetic moment
μ_r	relative magnetic permeability
μ_s	spin magnetic moment
χ	magnetic susceptibility

BIBLIOGRAPHY

[1] Sozinov A, Lanska N, Soroka A, ou W. Appl Phys Lett 2013;102:21902.

[2] Tellinen J, Suorsa I, Jääskeläinen A, Aaltio I, Ullakko K. Basic Properties of Magnetic Shape Memory Actuators, in:. 8th Int. Conf. ACTUATOR 2002. Bremen: 2002.

[3] Kumar PK, Lagoudas DC. Introduction to Shape Memory Alloys, in:. Lagoudas DC (Ed.). Shape Mem. Alloy. Model. Eng. Appl. Springer US; 2008.

[4] Kiefer B, Lagoudas D. Modeling of Magnetic SMAs, in:. Lagoudas DC (Ed.). Shape Mem. Alloy. Model. Eng. Appl., vol. 1, first ed. Springer US; 2008.

[5] Rhyne JJ, Foner S, McNiff EJ, Doclo R. J Appl Phys 1968;39:892.

[6] Liebermann HH, Graham CD. AIP Conf Proc 1976;29:715.

[7] Ullakko K, Huang JK, Kantner C, O'Handley RC, Kokorin V V. Appl Phys Lett 1996;69:1966.

[8] Wuttig M, James RD. Philos Mag A 1998;77:1273.

[9] Chernenko VA, Besseghini S. Sensors Actuators, A Phys 2008;142:542.

[10] Müllner P, Chernenko VA, Kostorz G. J Appl Phys 2004;95:1531.

[11] Straka L, Hänninen H, Soroka A, Sozinov A. J Phys Conf Ser 2011;303.

[12] Chmielus M. Composition, Structure and Magneto- Mechanical Properties of Ni-Mn-Ga Magnetic Shape-Memory Alloys, first ed. Berlin: Logos Verlag Berlin; 2011.

[13] Karaman I, Lagoudas DC. 2006;298.

[14] Hu F, Shen B, Sun J, Wu G. Phys Rev B 2000;64:132412.

[15] Cherechukin AA, Takagi T, Matsumoto M, Buchel'Nikov VD. Phys Lett A 2004;326:146.

[16] Ingale B, Gopalan R, Raja MM, Chandrasekaran V, Ram S. J Appl Phys 2007;102.

[17] Liu C, Mu HW, Gao LX, Ma WJ, An X, Gao ZY, Cai W. Appl Surf Sci 2010;256:6655.

[18] Ma J, Karaman I, Noebe R. Int Mater Rev 2010;55:257.

[19] Heczko O, Straka L. J Appl Phys 2003;94:7139.

[20] Pagounis E, Chulist R, Szczerba MJ, Laufenberg M. Scr Mater 2014;83:29.

[21] Solomon VC, Smith DJ, Tang Y, Berkowitz AE. J Appl Phys 2004;95:6954.

[22] Hubert A, Calchand N, Le Gorrec Y, Gauthier J-Y. Adv Electromagn 2012;1:75.

[23] Oxley DP, Tebble RS, Williams KC. J Appl Phys 1963;34:1362.

[24] Webster PJ, Ziebeck KR., Town SL, Peak MS. Philos Mag B 1984;49:295.

[25] De Graef M, McHenry ME. Structure of Materials: An Introduction to Crystallography, Diffraction and Symmetry, 2nd ed. Cambridge University Press; 2012.

[26] Hummel RE. Electronic Properties of Materials, Third Edit. Springer-Verlag New York; 2005.

[27] Kasap SO. Principles of Electrical Engineering Materials and Devices, Rev. Boston: McGraw-Hill Higher Education; 2000.

[28] Spaldin NA. Magnetic Materials: Fundamentals and Applications, second ed. Cambridge: Cambridge University Press; 2010.

[29] O'Handley RC. Modern Magnetic Materials: Principles and Applications. New York: John Wiley & Sons, Inc.; 1999.

[30] Müllner P, Chernenko VA, Wollgarten M, Kostorz G. J Appl Phys 2002;92:6708.

[31] Overholser RW, Wuttig M, Neumann DA. Scr Mater 1999;40:1095.

[32] Pons J, Chernenko VA, Santamarta R, Cesari E. Acta Mater 2000;48:3027.

[33] Pons J, Santamarta R, Chernenko VA, Cesari E. J Appl Phys 2005;97:83516.

[34] Righi L, Albertini F, Calestani G, Pareti L, Paoluzi A, Ritter C, Algarabel PA, Morellon L, Ricardo Ibarra M. J Solid State Chem 2006;179:3525.

[35] Mariager SO, Huber T, Ingold G. Acta Mater 2014;66:192.

[36] Heczko O, Cejpek P, Drahokoupil J, Holý V. Acta Mater 2016;115:250.

[37] Jiang C, Muhammad Y, Deng L, Wu W, Xu H. Acta Mater 2004;52:2779.

[38] Ge Y. The Crystal and Magnetic Microstructure of Ni-Mn-Ga Alloys. Helsinki University of Technology, 2007.

[39] Chmielus M. TRAINING, MICROSTRUCTURE, AND MAGNETO-MECHANICAL PROPERTIES OF NI-MN-GA MAGNETIC SHAPE-MEMORY ALLOYS. Boise State University, 2007.

[40] Sozinov A, Likhachev AA, Ullakko K. IEEE Trans Magn 2002;38:2814.

[41] Chernenko VA, Chmielus M, Müllner P. Appl Phys Lett 2009;95:104103.

[42] Murray SJ, Marioni M, Allen SM, O'Handley RC, Lograsso T a. Appl Phys Lett 2000;77:886.

[43] Chernenko VA, Pons J, Seguí C, Cesari E. Acta Mater 2002;50:53.

[44] Richard M, Feuchtwanger J, Schlagel D, Lograsso T, Allen SM, O'Handley RC. Scr Mater 2006;54:1797.

[45] Sozinov A, Likhachev AA, Lanska N, Ullakko K. Appl Phys Lett 2002;80:1746.

[46] Yu CH, Wang WH, Chen JL, Wu GH, Yang FM, Tang N, Qi SR, Zhan WS, Wang Z, Zheng YF, Zhao LC. J Appl Phys 2000;87:6292.

[47] Rolfs K. Influence of the Alloying Element Cobalt on the Key Properties of Ferromagnetic Shape Memory Ni-Mn-Ga Single Crystals. Technische Universität München, 2010.

[48] Budruk A. Microstructural Investigations of Defects and Domains in Magnetic Shape Memory Alloys. Carnegie Mellon University, 2012.

[49] Schlagel DL, Wu YL, Zhang W, Lograsso TA. J Alloys Compd 2000;312:77.

[50] Witherspoon C, Zheng P, Chmielus M, Dunand DC, Müllner P. Acta Mater 2015;92:64.

[51] Boonyongmaneerat Y, Chmielus M, Dunand D, Müllner P. Phys Rev Lett 2007;99:247201.

[52] Chmielus M, Zhang XX, Witherspoon C, Dunand DC, Müllner P. Nat Mater 2009;8:863.

[53] Müllner P, Zhang XX, Boonyongmaneerat Y, Witherspoon C, Chmielus M, Dunand DC. Mater Sci Forum 2009;635:119.

[54] Bernard F, Delobelle P, Rousselot C, Hirsinger L. Thin Solid Films 2009;518:399.

[55] Annadurai A, Nandakumar AK, Jayakumar S, Kannan MD, Raja MM, Bysak S, Gopalan R, Chandrasekaran V. J Magn Magn Mater 2009;321:630.

[56] Ahn JP, Cheng N, Lograsso T, Krishnan KM. IEEE Trans Magn 2001;37:2141.

[57] Tello PG, Castaño FJ, O'Handley RC, Allen SM, Esteve M, Castaño F, Labarta A, Batlle X. J Appl Phys 2002;91:8234.

[58] Chung CY, Chernenko VA, Khovailo V V., Pons J, Cesari E, Takagi T. Mater Sci Eng A 2004;378:443.

[59] Thomas M, Heczko O, Buschbeck J, Rößler UK, McCord J, Scheerbaum N, Schultz L, Fähler S. New J Phys 2008;10:23040.

[60] Heczko O, Thomas M, Buschbeck J, Schultz L, Fähler S. Appl Phys Lett 2008;92:72502.

[61] Zhang Y, Hughes RA, Britten JF, Gong W, Preston JS, Botton GA, Niewczas M. Smart Mater Struct 2009;18:25019.

[62] Scheerbaum N, Hinz D, Gutfleisch O, Müller KH, Schultz L. Acta Mater 2007;55:2707.

[63] Söderberg O, Brown D, Aaltio I, Oksanen J, Syrén J, Pulkkinen H, Hannula S-P. J Alloys Compd 2011;509:5981.

[64] Rodoni E, Levingston JM, SebastiánDeghi, Lescano DE, López GP, Urreta SE, Fabietti LM. Procedia Mater Sci 2015;8:577.

[65] Biffi CA, Tuissi A. Opt Laser Technol 2014;63:1.

[66] E. Assunção FMBFCMCRMMRJCS. Opt Lasers Eng 2011;49:1289.

[67] Kozieł T. Arch Metall Mater 2015;60:767.

[68] Balla VK, DeVasConCellos PD, Xue W, Bose S, Bandyopadhyay A. Acta Biomater 2009;5:1831.

[69] Craciunescu CM, Miranda RM, Silva RJC, Assuncao E, Braz Fernandes FM. Opt Lasers Eng 2011;49:1289.

[70] Smith AR, Tellinen J, Ullakko K. Acta Mater 2014;80:373.

[71] Ullakko K, Chmielus M, Müllner P. Scr Mater 2015;94:40.

[72] Frazier WE. J Mater Eng Perform 2014;23:1917.

[73] Gu DD, Meiners W, Wissenbach K, Poprawe R. Int Mater Rev 2012;57:133.

[74] Wong K V., Hernandez A. ISRN Mech Eng 2012;2012:1.

[75] Zheng B, Zhou Y, Smugeresky JE, Schoenung JM, Lavernia EJ. Metall Mater Trans A 2008;39:2237.

[76] Qi H, Azer M, Singh P. Int J Adv Manuf Technol 2009;48:121.

[77] Qi H, Azer M, Ritter A. Metall Mater Trans A 2009;40:2410.

[78] Carroll BE, Palmer TA, Beese AM. Acta Mater 2015;87:309.

[79] Herderick E. Additive Manufacturing of Metals: A Review, in:. Mater. Sci. Technol. 2011, vol. 2. Columbus, Ohio: MS&T'11; 2011.

[80] Foner S. Rev Sci Instrum 1959;30:548.

[81] Wu SK, Yang ST. Mater Lett 2003;57:4291.

[82] Callister WD. Materials Science and Engineering: An Introduction, Seventh. New York: John Wiley & Sons, Inc.; 2007.

[83] Brandmaier C, Spring KR, Davidson MW. Reflected Light DIC Microscopy | MicroscopyU, accessed 27 Jul. 2016. URL: http://www.microscopyu.com/techniques/dic/reflected-light-dic-microscopy.

[84] Bell DC, Erdman N. Low Voltage Electron Microscopy: Principles and Applications. Chichester: John Wiley & Sons; 2013.

[85] Brandon D, Kaplan WD. Microstructural Characterization of Materials, 2nd ed. Chichester: John Wiley & Sons; 2008.

[86] Cullity B. Elements of X-Ray Diffraction, 2d ed. Reading, Mass.: Addison-Wesley Pub. Co.; 1978.

[87] Tian Y, Mcallister D, Colijn H, Mills M, Farson D, Nordin M, Babu S. Metall Mater Trans A 2014;45A:4470.

[88] Tian B, Chen F, Tong YX, Li L, Zheng YF. J Mater Eng Perform 2012;21:2530.

[89] Lanska N, Söderberg O, Sozinov A, Ge Y, Ullakko K, Lindroos VK. J Appl Phys 2004;95:8074.

[90] Chernenko VA, Cesari E, Kokorin V V, Vitenko IN. Scr Metall Mater 1995;33:1239.

[91] Kohl M, Agarwal A, Chernenko VA, Ohtsuka M, Seemann K. Mater Sci Eng A 2006;438–440:940.

[92] Ranjan R, Banik S, Barman SR, Kumar U, Mukhopadhyay PK, Pandey D. Phys Rev B 2006;74:224443.

[93] Jiang C, Liang T, Xu H, Zhang M, Wu G. Appl Phys Lett 2002;81:2818.

[94] Klingbeil NW, Bontha S, Brown CJ, Gaddam DR, Kobryn PA, Fraser HL, Sears JW. Effects of Process Variables and Size Scale on Solidification Microstructure in Laser-Based Solid Freeform Fabrication of Ti-6Al-4V, in:. Proc. Solid Free. Fabr. Symp. [15th] Held Austin, Texas August 2-4, 2004. Austin, TX: University of Texas at Austin; 2004.

[95] Jin X, Marioni M, Bono D, Allen SM, O'Handley RC, Hsu TY. J Appl Phys 2002;91:8222.

[96] Kobryn PA, Moore EH, Semiatin SL. Scr Mater 2000;43:299.